Trace and Treat: Biodistribution and therapeutic potential of radiolabeled molecular and molecular carriers

Costanza Santini

513958-L-sub01-bw-Santini
Processed on: 22-9-2017

ISBN: 978-94-028-0787-5

Ontwerp en illustratie omslag, titelpagina's: Costanza Santini
Lay-out: Ton Everears
Drukwerk: Ipskamp Printing

Trace and Treat: Biodistribution and Therapeutic Potential of Radiolabeled Molecular and Supramolecular Carriers

Trace and Treat:
biodistributie en therapeutisch potentieel van radioactief gemerkte moleculaire en supramoleculaire dragers

Proefschrift

ter verkrijging van de graad van doctor aan de
Erasmus Universiteit Rotterdam
op gezag van de rector magnificus

Prof.dr. H.A.P. Pols

en volgens besluit van het College voor Promoties.
De openbare verdediging zal plaatsvinden op

dinsdag 17 oktober 2017
om 15:30 uur

Costanza Santini
geboren te Florence, Italy

Erasmus University Rotterdam

PROMOTIECOMMISSIE

Promotor(en)
Prof. dr. ir. M. de Jong

Overige leden
Prof. dr. P. Dubruel
Prof. dr. C. Löwik
Prof. dr. L. Hofland

Copromotor(en)
Dr. M.R. Bernsen

TABLE OF CONTENTS

CHAPTER 1

INTRODUCTION

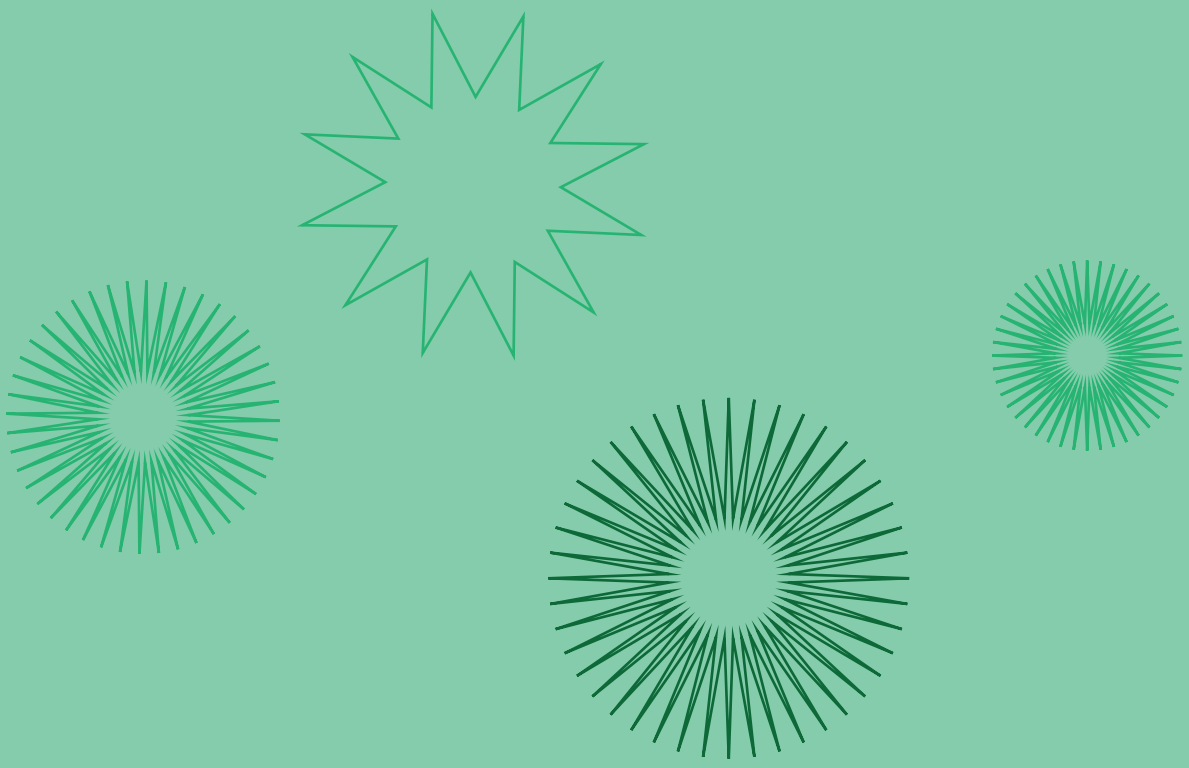

GENERAL INTRODUCTION

Cancer refers to lesions associated with the acquired capacity to freely proliferate, disseminate and grow in tissue that is different from the tissue of origin. It can originate from almost every cell type in the body [1, 2]. The probability of cancer development is strongly related to risk factors, which include environmental, behavioral (smoking, diet, physical activity, etc.) or genetic factors. Aging is also a risk factor of cancer; considering the generalized increse of life expectancy in developed countries, the incidence of cancer is expected to increase [3]. In the

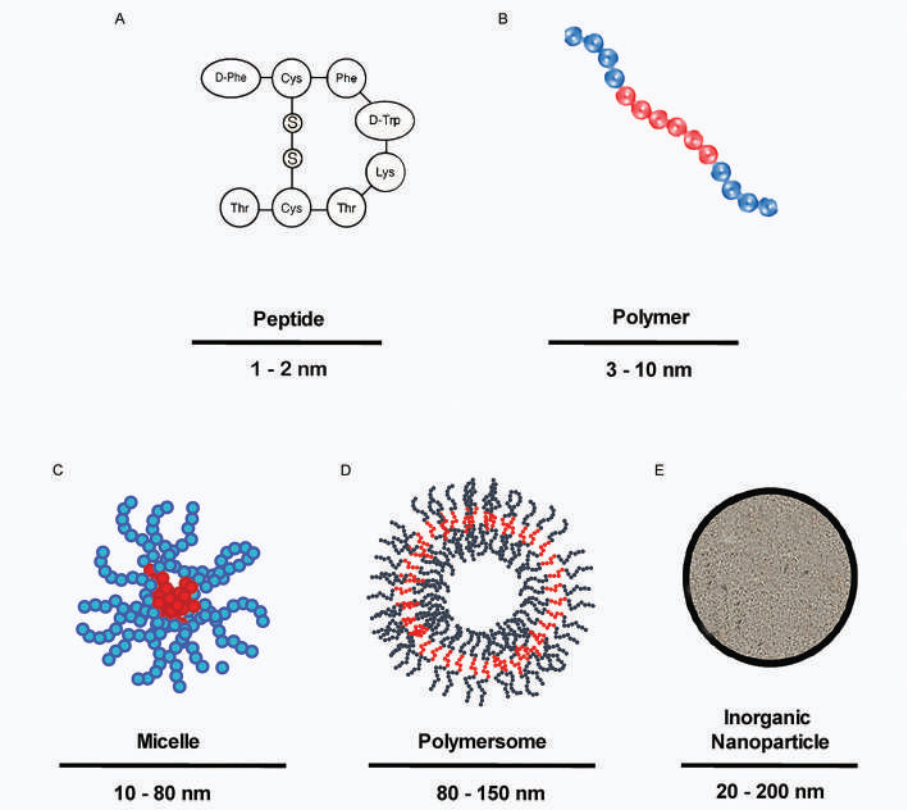

Figure 1. Schematic representation of molecules and supramolecular structures used as carriers in tumor imaging and therapy. A-B) Molecular carriers. A) Example of a targeting peptide: schematic structure of the somatostatin analogue octreotide; B) Example of a polymer: schematic structure of a tri-block copolymer. Blue dots represent the hydrophilic blocks; red dots represent the hydrophobic block. C-D) Supramolecular carriers. C) Schematic representation of a micelle: in blue is represented the hydrophilic corona and in red the hydrophobic core; D) Schematic representation of a polymersomes. The by-layer is depicted in dark-gray (hydrophilic part) and red (hydrophobic part). E) Schematic representation of an inorganic nanoparticle. Inorganic carrying nanoparticles include quantum dots, carbon nanotubes etc.

last decades, cancer incidence has indeed been increasing; however, improvements in cancer management have significantly reduced cancer mortality [2]. Common treatment approaches for cancer include surgical resection of lesions and systemic administration of anti-cancer drugs.

Surgical resection is often part of cancer treatment and may be the treatment of choice and curative for defined, contained and non-metastasized lesions. When surgical resection is not possible or does not suffice, systemic therapy (such as chemo- or radio- therapy) is (also) required [4, 5], as it allows for whole-body distribution and treatment of primary tumor and metastases.

The localization and the determination of tumor stage and dissemination are therefore crucial to define the best approach. Molecules able to specifically accumulate in tumor tissue have greatly improved the detection via molecular imaging and the delivery of drugs for therapeutic purposes [4, 6]. The results obtained in cancer imaging and therapy have strongly encouraged novel research leading to a huge proliferation of novel tumor-targeting compounds [7]. These compounds are designed to show accumulation at the target site, bind to receptor structures, or are cleaved in a specific way by enzymes. Besides molecular probes, supramolecular particles are also being developed, including polymers, polymeric micelles, nanoparticles, liposomes, and micro bubbles. They represent emerging molecular imaging instruments because of their high versatility to serve as imaging agents. Examples of molecules used for tumor targeting are shown in Figure 1.

Labels most commonly used for imaging include radionuclides, fluorescent molecules, paramagnetic ions or combinations thereof. Besides providing a signal for imaging, various labels can also be used for therapeutic purposes and/or for theranostic approaches. The use of radionuclides attached to specific targeting compounds, is an approach within nuclear oncology that has been gaining increasing interest [8].

However for effective in vivo applications, imaging and therapeutic agents must overcome numerous physiological hurdles within the body, including rapid excretion, non-specific accumulation in non-target tissues, metabolic degradation, clearance and pharmacologic delivery barriers [9]. In this thesis, we describe our studies on biological properties of two categories of biomolecules, i.e. peptides and nanoparticles, that were either labeled with a radionuclide or dual labeled with a radionuclide and an fluorochrome, thereby describing some main biological barriers these compounds have to overcome, to reach the tumor tissue.

Introduction to radioactivity

All matter consists of atoms, with a positively charged nucleus, surrounded by a cloud of negatively charged electrons. Atomic nuclei consist of two particle types with similar mass: protons (positively charged) and neutrons (uncharged). The number of protons within an atomic nucleus (referred to as atomic number, Z) determines to which element the atom belongs. Each element is characterized by a unique number of protons, and the same number of electrons. Neutrons in the nuclei "balance" the repulsion among the positively charged protons and determine the stability of the atom. The optimal ratio between protons and neutrons for stable nuclei changes over the periodic table, but lies between 1 and 1.4 [10] (Figure 2). The number of neutrons (neutron number, N) in atoms having the same atomic number (i.e. same element), does not influence the chemical properties of an element. Nuclei having non-optimal proton/neutron ratios are unstable and will decompose, emitting ionizing electromagnetic and/or particle radiation in order to reach a stable state (i.e. optimal proton/neu-

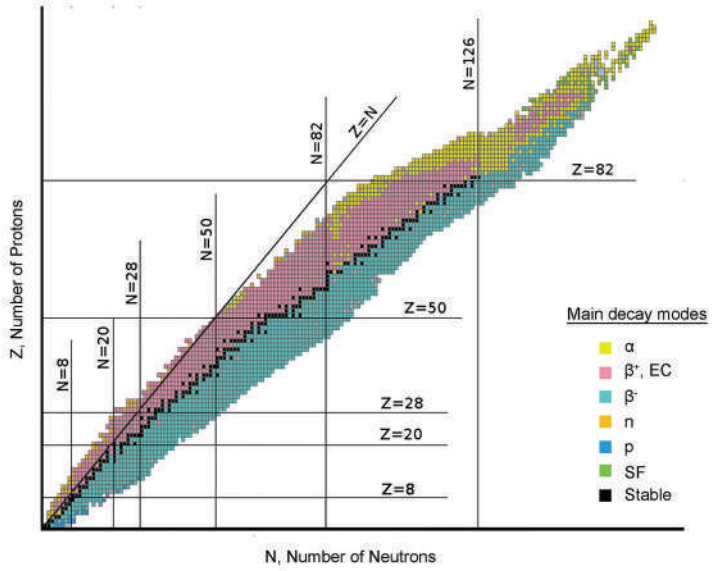

Figure 2. Nuclides by type of decay. Every square represents a different element as function of its number of neutrons and number of protons. Stable nuclides are depicted in black. Nuclides with excessive neutrons or protons are unstable leading to β^- (light blue) or β^+ (pink) decay, respectively. At high atomic number (on the top-right of the graph), alpha emission (yellow) or spontaneous fission (green) become common decay modes. The line indicated as N=Z represents the theoretical position on the graph of nuclides for which proton number is the same as neutron number. α: alpha decay; β^+: beta + decay; EC: electron capture; β^-: beta- decay; n: neutron emission; p: proton emission; SF: spontaneous fission. (Image adapted from International Atomic Energy Agency, webpage https://www-nds.iaea.org/relnsd/vcharthtml/VChartHTML.html with permission from the copyright holder).

tron ratio). Depending on the composition of the nucleus, different decay modes exist, leading to a release of energy and the transition to a lower energy state. The three main decay modes of radionuclides used in medicine, distinguished by the type of the emitted radiation/particle are: the emission of alpha (α) particles (α-decay), beta (β, + or -) particles (β^+ and $^-$-decay), or gamma (γ) radiation (γ-decay).

Radionuclides in nuclear medicine

Radioactivity in medicine is mainly used for nuclear imaging and oncological therapy, although radiation is used for other medical applications as well [11, 12].

The aim of nuclear imaging in oncology is the detection of tumor tissue for diagnosis, staging and monitoring after treatment. For this purpose, nuclear agents are administered to generate three dimensional (3D) maps of radioactivity distribution, used to assess tumor status [11, 12]. Gamma photons are most suitable for imaging purposes as they have deep penetration in biological tissues and little release of energy over their path. These two properties allow for the detection of deep lesions with low/no damage to normal tissue.

Gamma photons can be detected with the aid of two nuclear imaging techniques: Single Photon Emission Computed Tomography (SPECT) or Positron Emission Tomography (PET).

In SPECT imaging, single photons emitted from a radioactive source are detected by rotating gamma cameras (Figure 3A). Data is collected and processed via a reconstruction algorithm to generate 3D images that represent the distribution of radioactivity. SPECT machines are equipped with an absorbing plate (called "collimator") with holes (parallel-holes or pin-holes) [13, 14] (Figure 3B). Pinhole collimators give higher spatial resolution compared to parallel-holes, but require that the collimator is close to the emitting source. This option makes SPECT an excellent tool for "small object imaging" such as in preclinical investigations [15] (Figure 3).

PET is another nuclear imaging technique, broadly employed at the clinical and preclinical level. It is the most sensitive nuclear imaging method, as no collimators are needed [16]. PET relies on the detection of two gamma photons generated after positron (β^+) decay. After radioactive decay of the nucleus the positron can travel over a short distance in the tissue while losing kinetic energy. It then interacts with an electron resulting in mutual annihilation and release of energy in the form of two electromagnetic photons of 511 keV each, that travel in opposite direction [17]. The detection of these two photons by the PET camera occurs simultaneously allowing for the 3D localization of the originating source (Figure 4).

Both SPECT and PET imaging are often combined with another technique such as Computed Tomography (CT) or Magnetic Resonance Imaging (MRI). The combination with such techniques improves the 3D source localization by providing anatomical reference [18]. The studies presented in this thesis are performed using a state-of-the art preclinical SPECT/CT platform.

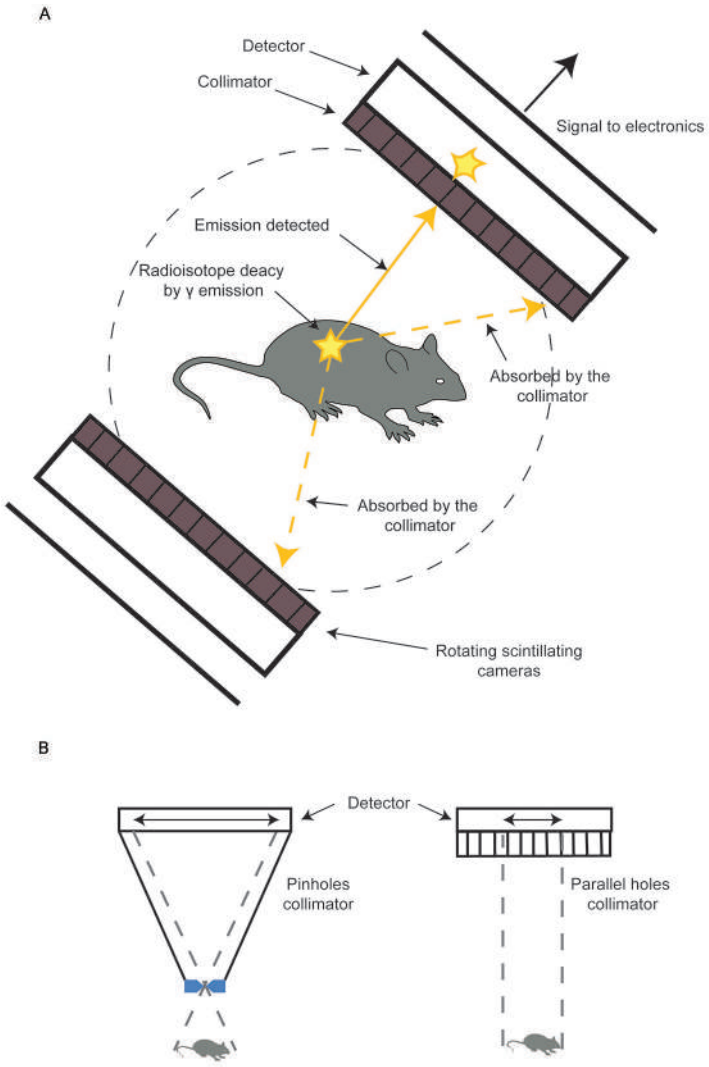

Figure 3. Single Photon Emission Computed Tomography (SPECT). A) Schematic representation of the SPECT imaging principle. Gamma photons resulting from nuclear disintegrations are detected by a detector. The presence of a parallel-hole collimator allows only perpendicular photons to pass through and reach the detector. Other photons are absorbed by the collimator. B) Schematic representation of pinhole (left) and paralle-hole (right) collimation in SPECT imaging.

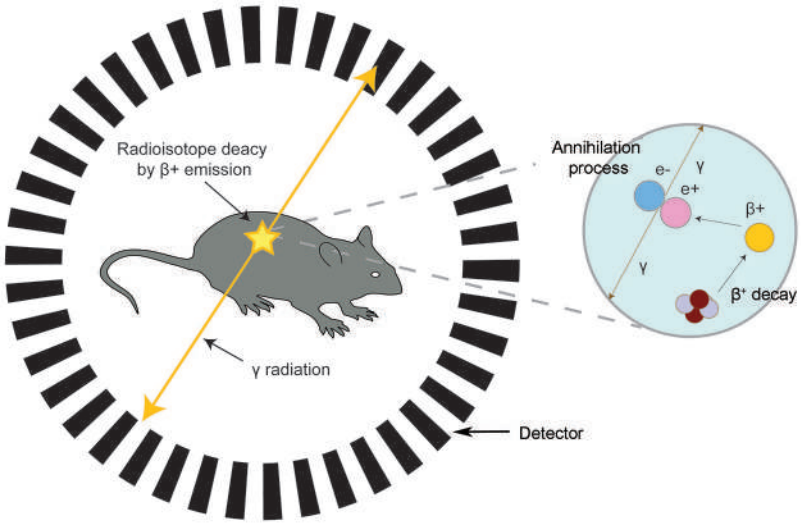

Figure 4. Schematic representation Positron Emission Tomography (PET) imaging principle. A positron (β^+) is emitted after the radioactive disintegration of one proton into a neutron; after disintegration, the positron travels shortly before interacting with an electron. The interaction results in the annihilation of the positron and electron, and the release of energy by two electromagnetic radiation of 511 keV traveling oppositely. The detectors of a PET machine areable to detect the two emitted photons contemporaneously and form a three-dimensional image localizing the emitting source.

Ionizing radiation emitted by radionuclides can also be used for therapeutic purposes. Radiation is used to cause damage in cancer cells resulting in cancer cell death or reduced proliferative capacity. To be effective in inducing (fatal) biological damage the radiation dose delivered to the tumor must be sufficiently high. For this purpose, emitted ionizing radiation should have limited tissue penetration and release energy over a short path. Currently radionuclides emitting β^- particles are the most used for therapy; however also α particle and Auger electron-emitting radionuclides have shown to be suitable for therapeutic applications [11, 19].

Considering the properties needed for imaging or therapy, radionuclides can be classified as imaging radionuclides or therapeutic radionuclides (Table 1). A radionuclide can decay via more than one decay mode. In some cases one radionuclide can be suitable for both imaging and therapy, and can be classified as a true "theranostic" radionuclide (therapy + diagnosis). An attractive example is represented by ^{177}Lu, a radionuclide used for therapy decaying via β^- emission. During therapy, however it is also suitable for SPECT imaging because of its emission of gamma radiations. In Table 1 several used radionuclides in nuclear medicine are listed.

Table 1. List of radionuclides applied in nuclear medicine

Radionuclide	$T_{½}$ (h)	Decay Mode	Main use in nuclear medicine
^{99m}Tc	6.02	IC, γ	Imaging (SPECT)
^{111}In	67.9	EC, γ	Imaging (SPECT) Therapy
^{67}Ga	78.26	EC, Auger, γ	Imaging (SPECT)
^{123}I	13.2	EC, γ	Imaging (SPECT)
^{18}F	1.83	β^+, EC	Imaging (PET)
^{68}Ga	1.13	β^+, EC	Imaging (PET)
^{64}Cu	12.7	β^+, β^-, EC	Imaging (PET) Therapy
^{86}Y	14.7	β^+, EC	Imaging (PET)
^{124}I	99.6	β^+, γ	Imaging (PET)
^{90}Y	64.1	β^-	Therapy
^{177}Lu	161	β^-, γ	Therapy Therapy + Imaging
^{67}Cu	61.9	β^-	Therapy
^{213}Bi	0.76	α, β^-	Therapy
^{225}Ac	240	α	Therapy

Data present the physical half-life, the main nuclear emission pathway and the main application in nuclear medicine. T½ (h): physical half-life in hours; α: alpha-decay; β^+: beta$^+$-decay; β^-: beta$^-$-decay; γ: gamma-decay; IC: internal conversion; EC: electron capture; PET: positron emission tomography; SPECT: single photon emission tomography.

Carriers: molecules to bring radioactivity in target tissues

To be efficient in exerting diagnostic or therapeutic functions, radioactivity needs to reach and accumulate in tumor tissue at a sufficiently high level. Radionuclides can be injected as free agent, although most often they are incorporated in a bigger structure, a carrier, to improve the accumulation in tumor tissue. Such carriers comprise molecules of different chemical/physical properties and biological behaviors (Figure 1) [6, 20]. An extensive description of various carriers available or used for the delivery of radioactivity for tumor diagnosis and therapy has been published by Psimadas et al. [21] and by Gudkov et al. [22].

Once introduced into a biological system, carriers have to face several challenges. In order to accumulate in target tissue, carriers have to evade host clearance pathways, including the immune system and other physiological and pharmacological barriers. Moreover, next to sufficient accumulation in the target tissue, carriers should show tolerable accumulation in off-target tissues.

Accumulation of a carrier in the tumor is influenced by both carrier's properties and tumor properties.

The retention of carriers in off target tissue often concerns the main clearance organ for a specific carrier (e.g. liver, spleen, or kidneys). When accumulation in these organs is elevated it can become critical because of possible toxic effects to these organs.

Focusing on the two types of radiolabeled carriers as investigated in this project, i.e. peptides and polymer based nanoparticles, the possible ways of carrier accumulation and clearance routes are discussed, since they may influence biodistribution outcomes.

Radiolabelled peptides

Peptides are molecules consisting of amino-acids (<100) linked via peptide bonds.

Stabilized peptides were preferred over the endogenous peptides for the delivery of radioactive agents to tumors expressing specific receptors because of the longer in vivo stability [23, 24].

For nuclear imaging, as well as radionuclide therapy, the incorporation of a radionuclide is a crucial aspect. Chelating structures ("chelators") are often used to modify peptides, allowing for stable incorporation of many clinically relevant radionuclides. In some cases, chelators have been shown to be more suitable for use in humans compared to other approaches (e.g. iodination) [25]. Moreover, coupling of chelators is in general well tolerated by peptides, i.e. the receptor binding capacity is preserved [26-28].

Active targeting: the prototype of receptor-mediated tumor targeting by somatostatin analogues

Receptors are protein-based structures allowing for e.g. cellular communication with the outer environment. Some tumors are known to overexpress one or more membrane receptors. Specific targeting carriers binding to the overexpressed receptor can be used to deliver radioactivity for imaging and/or therapy, indicated as "active targeting" [29]. A convincing

example of the potential of such active targeting is represented by the currently widely used approach for imaging and therapy of neuroendocrine tumors (NET) [30]. NETs represent a rare neoplasm that are known to highly overexpress somatostatin receptors (SSTR) [31]. In (patho)physiological conditions SSTR binds endogenous somatostatin, which has an inhibitory effect on tumor cell growth and hormone secretion [32].

Small stable somatostatin peptide analogues that are able to bind SSTR with high affinity have been developed. Compared to endogenous peptide such somatostatin analogues also have longer stability in vivo and therefore higher pharmacologic efficacy. In clinical studies, somatostatin analogues have been introduced as a palliative treatment for NETs, providing symptom alleviation and in some cases interruption of tumor growth [33, 34].

The radiolabeling of somatostatin analogues with specific imaging radionuclides, has enabled detection of tumor lesions via nuclear imaging techniques for non-invasive diagnosis, staging and follow up of NETs (Figure 5) [35].

As a next step, the capacity of somatostatin analogues to reach SSTR was used to deliver therapeutic radionuclides to NETs, an approach that is known as peptide receptor radionu-

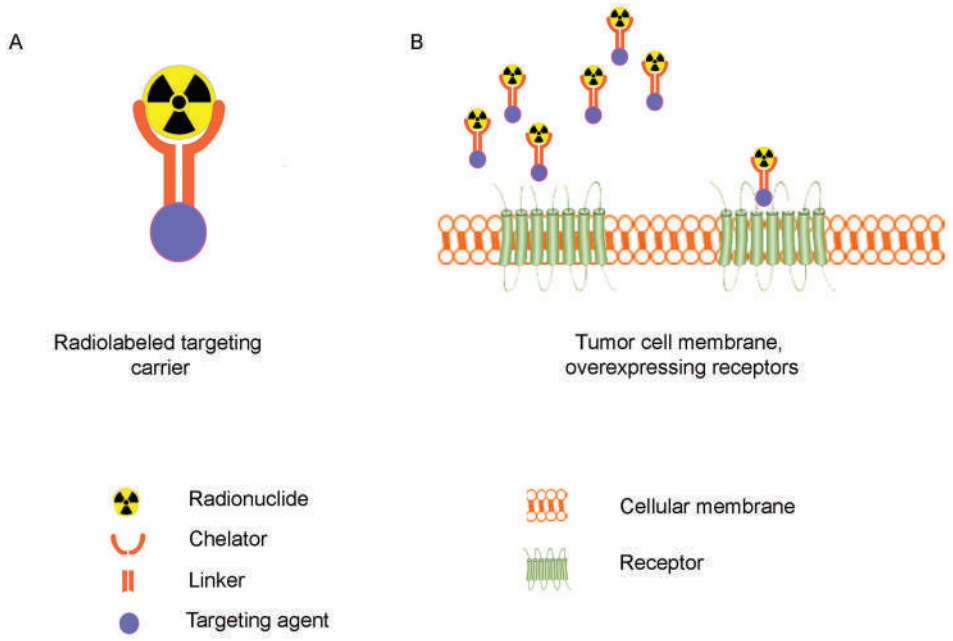

Figure 5. Schematic representation of a targeting carrier and active targeting. A) Schematic representation of a radiolabeled peptide. The targeting carrier is derivatized with a chelator for radionuclide binding and sometimes also a linker; B) Targeting peptides binding receptors that are (over)expressed on the membrane of tumor cells.

clide therapy (PRRT). Clinical studies on PRRT treatment proved the efficacy and the safety of this approach for NETs; minor and partial tumor responses in up to 35% of cases and tumor stabilization in the 60% of cases was observed [36, 37].

A high tumor dose and favorable ratio between the dose to the tumor and the dose to healthy (dose limiting) tissues are the major aims during PRRT. The amount of radioactivity delivered to the tumor determines the therapeutic response; while the high dose ratio between tumor and healthy tissues is needed to reduce off target toxicity. Specific activity and treatment schemes have shown to influence these two parameters, as shown in Chapter 2.2.

Specific activity of a radiolabeled peptide can be defined as the amount of radioactivity coupled to a peptide (MBq/nmol). This ratio can affect the tumor dose, as high specific activities will lead to lower saturation levels of the receptors. In conditions of high specific activity, the level of radiolabeled peptide molecules binding SSTR is higher and the dose to the tumor will increase [38].

As shown in Chapter 2.2 variations of fractionation schemes of therapeutic doses in radionuclide therapy can influence the therapeutic outcome as well. In this preclinical study we obtained significantly increased tumor to organ ratios in groups treated with the same dose of ^{177}Lu-DOTA,Tyr^3-octreotate administered at different time points.

Main clearance pathway in NET radionuclide therapy

Despite PRRT with radiolabeled somatostatin analogues is effective and well tolerated in patients [35] systemic application of radiolabeled peptides exposes the body to radiation. Mild nonspecific side effect (abdominal pain and fatigue) are often observed after administration of therapeutic doses of radiolabeled somatostatin analogues [35, 39]. Next to that specific organs like kidney and bone marrow can experience toxicity as well [39].

Kidneys are the main organs involved in clearance of most chelated radiopeptides and can be affected by radiation damage. Radiolabeled somatostatin analogues reach the kidneys via the renal artery; the peptides are filtered at the level of the glomerulus and most of them are then excreted via the urine [26, 40, 41]. A relatively small but significant amount of somatostatin analogues however is reabsorbed in the kidney in the proximal tubules via both SSTR-mediated [42] and "not-SSTR-mediated" mechanisms [40]. These mechanisms determine reabsorption and retention of the radioactivity in the kidneys over time .

As a result of re-uptake and retention of radioactivity, the kidney can develop acute or late toxicity during or after treatment with radiolabeled somatostatin analogues [43-45]. Positively charged molecules can interfere with the mechanism of peptide-reabsorption. The application of positively charged amino-acids has been shown to provide renal protection

in treated patients by reducing the reabsorption of radiolabeled somatostatin analogues [46, 47].

Somatostatin analogues for multimodal image-guided surgery

Despite the enormous improvement in the systemic treatment of cancer, the most successful results in tumor management are still obtained by surgical resection of operable lesions [48]. Improvements in resection outcomes have been reached by the use of nuclear imaging techniques that allow for tumor localization prior to surgery and the set-up of a surgical plan [48, 49].

In principle, the same radiation used for nuclear imaging can be used to provide surgical guidance during surgery as well and improve resection outcomes [48-51]. The radioactive signal, identified via a portable gamma-detector can guide the surgeon towards the lesions, even when it is localized deep in the tissue. Radio-guidance has brought a significant improvement in surgery of tumor because of the real-time feedback during resection [50-52]. The approach however has drawbacks as well and could profit from additional optical signal feedback during surgery.

Optical image-guided surgery makes use of optical probes to provide real-time visual feedback during surgery. The application in different procedures in human patients has provided extremely encouraging results [53, 54]. On the other hand optical signals suffer from poor penetration in biological tissue, restricting the application of optical probes to superficial lesions only [55].

Optical-and-nuclear dual-modality imaging probes have raised interest in the field of image-guided surgery because of the complementary characteristics [56, 57]. While radioactive signals can be detected from deeply lying lesions, the optical signal is very effective in giving the needed real-time visual feedback in close proximity to the lesion [48, 56, 58-60].

The simultaneous use of the two imaging modalities could be accomplished by two main approaches [58, 61]: by using one single agent carrying both a nuclear and a fluorescent moiety, or by the co-injection of two agents (one conjugated with a radiotracer, and the other conjugated with a fluorescent probe). One single carrier with multiple labels was found preferable over the two mono-functionalized ones because of the more reliable and coherent feedback (i.e. overlapping of nuclear and optical signal) [60, 62].

The first application of agents carrying optical-and-nuclear labels for image-guided surgery was in sentinel lymph node detection and resection in breast [60] and prostate cancer [58, 59]. In these cases, the carrying molecules were dual-labeled colloids able to diffuse passively through the lymphatic system [41].

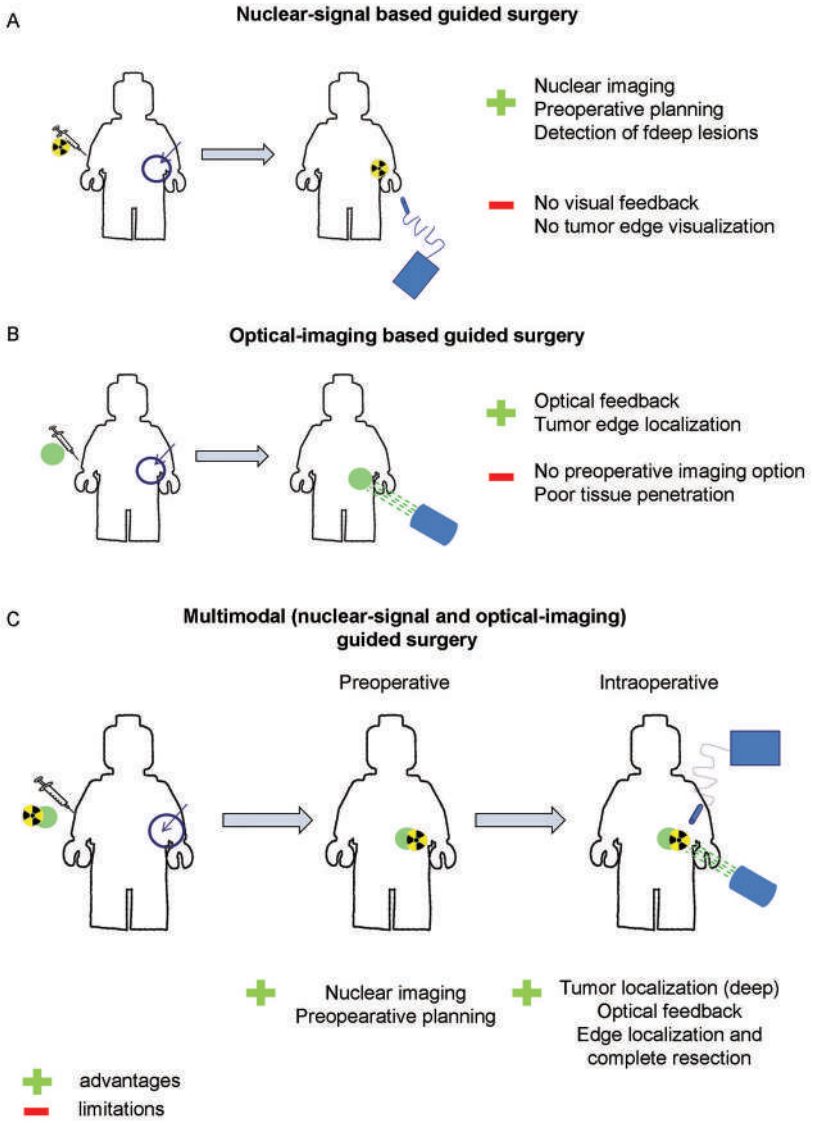

Figure 6. Schematic representation of three image guided surgery options. A) Diagram of nuclear-signal based guided surgery pros and cons. Detection can be performed prior to resection via nuclear imaging approaches (e.g. SPECT) for preoperative imaging. During the surgery, superficial or deep lesions can be detected by a dedicated gamma detector that guides the surgeon towards the lesion. The method lacks real-time optical feedback and is prone to result in incomplete resection; B) Diagram of optical-imaging based guided surgery pros and cons. The surgeon can read the optical signal at the operative theater and get a real-time optical feedback of superficial lesions. The optical signal allows for complete and precise resection; C) Diagram of multimodality (nuclear-signal and optical-imaging) imaging based guided surgery. It combines the benefits of nuclear signal and optical imaging guided surgery, providing the possibility of pre-operative nuclear imaging, detection of deep lesions, real-time optical feedback for localization and complete resection of tumor.

Further steps in multimodality guided surgery were made by modifying targeting peptides with a multimodal moiety and use them to mark tumor lesions. For some peptides commonly used for tumor targeting, the attachment of a multimodal moiety did not substantially alter the affinity for the receptor. Multimodality peptides applied in vivo in preclinical studies showed considerable levels of accumulation in the tumor and allowed for tumor detection via both nuclear and optical imaging. Results with targeting peptides carrying multimodal agents were extremely positive [48, 56], and gave high expectation for further improvement in image-guided surgery, and potential to translate the method to the clinic (Figure 6). In Chapter 2.1, the study on the potential of this dual-imaging approach using somatostatin analogs as targeting vector are described; hereby focusing on the effects of the dual-labeling procedure on receptor binding affinity and in vivo tumor accumulation capability of the modified tracers.

Radiolabeled nanoparticles

Nanoparticles have a size between five to several hundreds of nanometers. They can interact with cancer tissue, biomolecules and subcellular structures [63]. Many nanoparticles are available for medical application; they can differ in terms of size, shape, chemical composition etc. An interesting aspect of nanoparticles is their versatility as biological carrier, which includes the possibility to carry radionuclides.

For some nanoparticles radiolabeling is often obtained via attachment of a chelator on the outer structure that can be subjected to a radiolabeling step [64, 65]; other nanoparticles can incorporate radionuclides (or small radioactive complexes) and stably retain them [66].

Despite the large number of nanoparticles available, when applied in vivo, they follow similar pathways with regard to tumor accumulation and clearance pathways [67].

Tumor accumulation of nanoparticles occurs mostly via the Enhanced Permeability and Retention (EPR) effect, also referred to as “passive targeting” [29]. In contrast to active targeting, that involves binding/interaction of a probe with a specific target , the EPR effect is based on passive extravasation of particles though leaky blood vessels as is often the case with tumor vasculature [68]. Accumulation in tumors, therefore, is not restricted to one (or few) tumor type(s) expressing a specific target, but nanoparticles can potentially target every solid tumor via the EPR effect. It is possible to attach specific ligands for tumor targeting to nanoparticles adding the mechanism of specific target -ligand interaction (so called “targeted nanoparticles”) to the biodistribution properties of nanoparticles [29]

Many nanoparticles share the same clearance pathway. Clearance generally occurs via liver and/or spleen, as the size of nanoparticles often exceeds the renal filtration limit (being <5

nm)[41]. Clearance via liver or spleen can result in accumulation of particles in these two organs, whereas further clearance steps can involve other tissues as well (e.g. intestines via hepatobiliary excretion). Often long lasting retention of nanoparticles is seen in the liver and spleen; they might become dose limiting organs in case particle uptake is high.

In this thesis, we describe the investigation of two different types of polymeric nanoparticles that show potential as carrier and for delivery of radioactivity to tumors. We tested these nanoparticles in their molecular form, i.e. unimers, or in their supramolecular form as micelles.

Block copolymers and Pluronic unimers. Polymers are nanosized macromolecules consisting of repeated parts. When the same part is repeated, the polymer is called a "homo-polymer"; when different parts are repeated the polymer is called "copolymer". When chemically similar repeated units are organized in blocks and linked together by a covalent bond, the polymer is named a "block copolymer". Pluronics are a class of amphiphilic linear tri-block copolymers consisting of a hydrophilic part of poly(ethylene oxide) (PEO) and a hydrophobic part of poly(propylene oxide) (PPO), arranged in a A-B-A tri-block structure: PEO-PPO-PEO [69]. They have an extremely versatile structure, are easy to modify by the attachment of

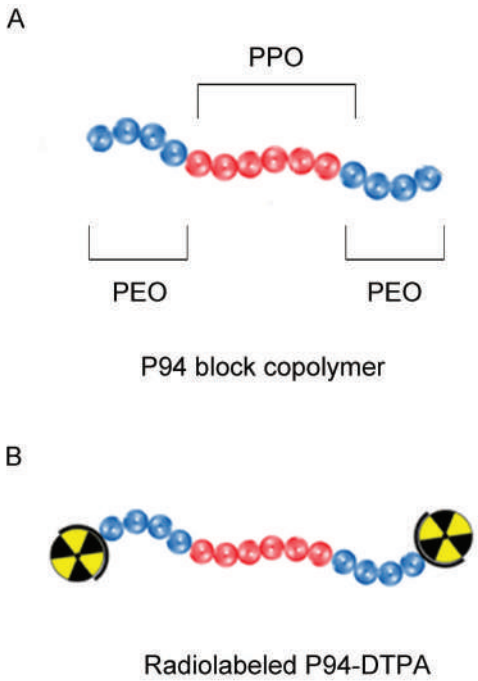

Figure 7. Schematic representation of a Pluronic P94 block copolymer. A) Structure of Pluronic P94; B) Example of the radiolabeled DTPA-P94. PPO: poly(propylene oxide (hydrophobic part); PEO: poly(ethylene oxide)(hydrophilic part).

different moieties and present excellent properties for in vivo application such as the high longevity in vivo and low level of toxicity [64]. Some formulations of Pluronics block copolymer have been approved by the Food and Drug Administration (FDA); they are used in cosmetics, in food and in the clinic as a adjuvant for injection [70]. Pluronics have also shown potential in anti-multi-drug-resistance in tumors and as platform for the delivery of drugs to tumor lesions [71, 72]. Because of their nanosized dimension (4-10 nm)[64], Pluronics as unimers can accumulate in tumor tissues as a result of the EPR effect [29, 73] (Figure 7). Application of Pluronic P94 block-copolymer in vivo as carrier for the delivery of agents (i.e. radioactivity) is described in Chapter 3.1.

Block-copolymer-based supramolecular aggregates. In aqueous solution, at specific concentrations and temperatures, block copolymers can stably aggregate into supramolecular structures defined as "polymeric supramolecular aggregates". Because of this property polymeric aggregates, at room temperature and in polar solvents, are thermodynamically more stable than the copolymer and tend to remain aggregated.

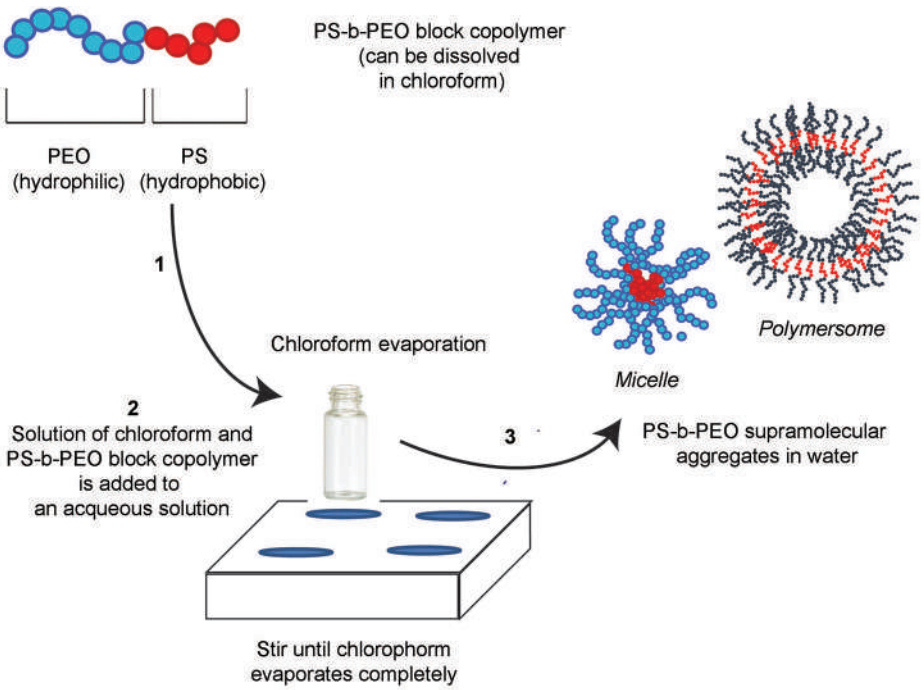

Figure 8. Schematic representation of PS-b-PEO block copolymer and diagram of PS-b-PEO based supramolecular aggregate formation. 1- PS-b-PEO block copolymer in a chloroform solution is added to a watery solution; 2- chloroform is evaporated; 3- During the evaporation of chloroform PS-b-PEO copolymer aggregates in supramolecular aggregates. PS: Poly(styrene); PEO: poly(ethylene-oxide)

Application in vivo demonstrated that supramolecular structures of PS-b-PEO copolymers have long lasting stability in the circulation and the ability to accumulate in the tumor via the EPR effect, suggesting potential as a delivery system to tumors. In this respect, PS-b-PEO polymeric aggregates have shown high versatility for labeling with different agents [74].

The capacity to generate nanoparticles with good kinetic and thermodynamic stability, that are tunable in size and easy to load with different agents, is a crucial aim for in vivo applications [75, 76]. Lately, poly(styrene)-poly(ethylene-oxide) block copolymers (PS-b-PEO) have shown interesting properties such as spontaneous aggregation in supramolecular structure (e.g. micelles, polymerosomes) tunable morphology (i.e. size and shape) and potential for easy loading [66, 74]. Poly(styrene) cores (PS) present a "glassy" structure, meaning that once

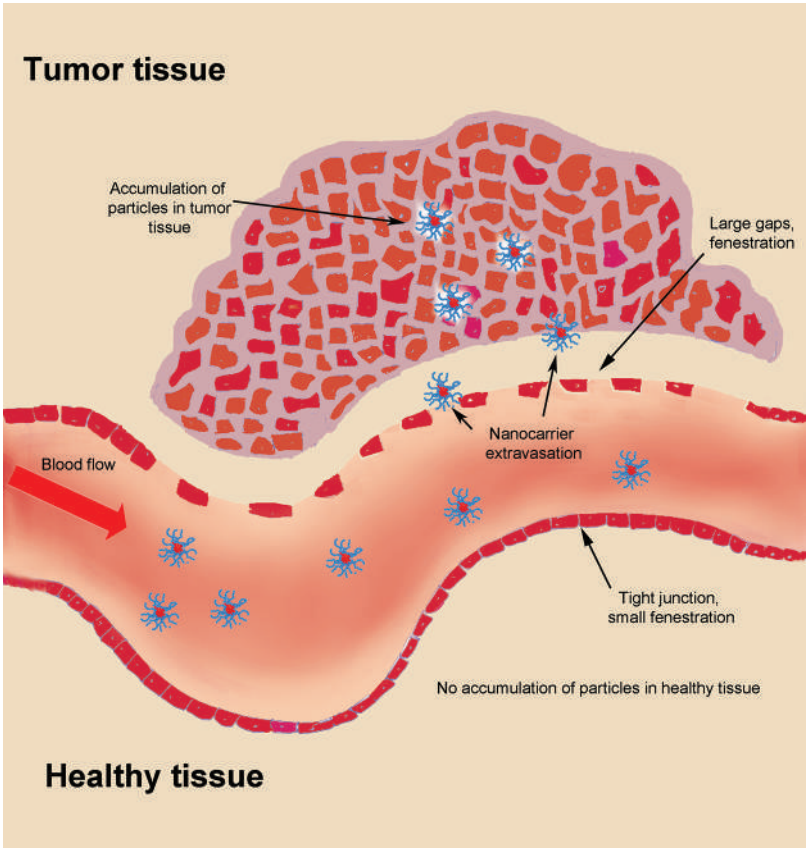

Figure 9. Schematic representation of passive targeting: the Enhanced Permeability and Retention (EPR) effect. Tumor vessels present bigger fenestration compared to healthy vasculature. Tumor vessels are thus more permeable to solutes in the blood stream. Particles from 5 nm up to 500 have shown to be able to extravasate at the tumor level and accumulate there.

aggregates are formed the block copolymer cannot freely dissociate anymore [66, 74, 77] , thus conferring extensive stability in different conditions, including physiological conditions in vivo.

The loading of PS-b-PEO aggregates with different agents occurs during the synthesis of supramolecular structures, without the need of chemical modifications. Formation of supramolecular structures enables stable incorporation of hydrophobic complexes (e.g. ^{111}In-tropolone [66] or fluorophore [74]). This principle can be applied not only for the incorporation of imaging agents, but also therapeutic agents, making the PS-b-PEO aggregates suitable for theranostic applications (Figure 8). The first application of radiolabeled PS-b-PEO supramolecular aggregates is shown in Chapter 3.2. The role of the size in the distribution of these radiolabeled PS-b-PEO supramolecular aggregates is described in Chapter 3.3.

Passive targeting: selective tumor accumulation of nanoparticles via the EPR effect

The EPR effect is a passive phenomenon occurring in rapidly growing, solid tumors. In such tumors the demand of oxygen and nutrient grow accordingly and this cannot be covered by simple diffusion [68]. Although tumor cells can become quite resistant to starvation and hypoxia, soon in the progress of cancer, the formation of new vasculature that improves the delivery of nutrients can be observed [78]. This phenomenon is known as tumor angiogenesis [79]. Due to a persistent stimulatory signal from tumor cells, the newly formed vasculature is continuously remodeled and remains in a substantially underdeveloped state [79]. Compared to normal mature vessels, the underdeveloped tumor vasculature has bigger fenestrations of 100-600 nm [80], no tight junction between endothelial cells [81, 82] and the tumor tissue misses a functional lymphatic system [68, 83]. These conditions favor vessel permeability due to the bigger fenestration, and an improved retention, because of the lack of lymphatic drainage.

Size is one of the most important parameters for the EPR effect. Particles between 5 to 200 nm present a higher level of EPR mediated accumulation in tumor tissue compared to those of <5 nm, which are rapidly cleared from tissues [84, 85]. A second parameter for successful EPR effect, is the biological half-life of particles in the circulation. Particles that remain longer in circulation have higher chance to pass through the tumor vasculature and extravasate. The extent of accumulation in the tumor due to the EPR effect is also dependent on the intra-tumoral pressure.

Despite the difficulties encountered to obtain a sufficient level of carriers (and payload) in the tumor, one big advantage of EPR over targeted accumulation is the potentially broad applicability of the method. As a tumor-specific targeting agent is not required, particles that benefit from the EPR effect can be used to deliver agents to any solid tumor with leaky vessels (Figure 9).

Main clearance organs of nanoparticles: the liver and spleen

The liver is an organ involved in many vital functions. In pharmacology, the interest around the liver is mostly on its role as clearance/detoxifying organ; the liver is able to retain, inactivate and regulate excretion of drugs. The liver receives blood supply from the systemic circulation via the portal vein and the hepatic artery. Blood enters via the hepatic tissue, afterwards it further subdivides into a network of capillaries with a diameter of 5-10 μm and fenestrae of 100-150 nm, called sinusoids [86-88]. The fenestrae of sinusoids allow the passage of most of the plasma components in the space of Disse. In general molecules with a size <200 nm can pass through the fenestrae and become available for the hepatic cells that can internalize them via pinocytosis and receptor mediated endocytosis [89]. Endothelial cells and Kupffer

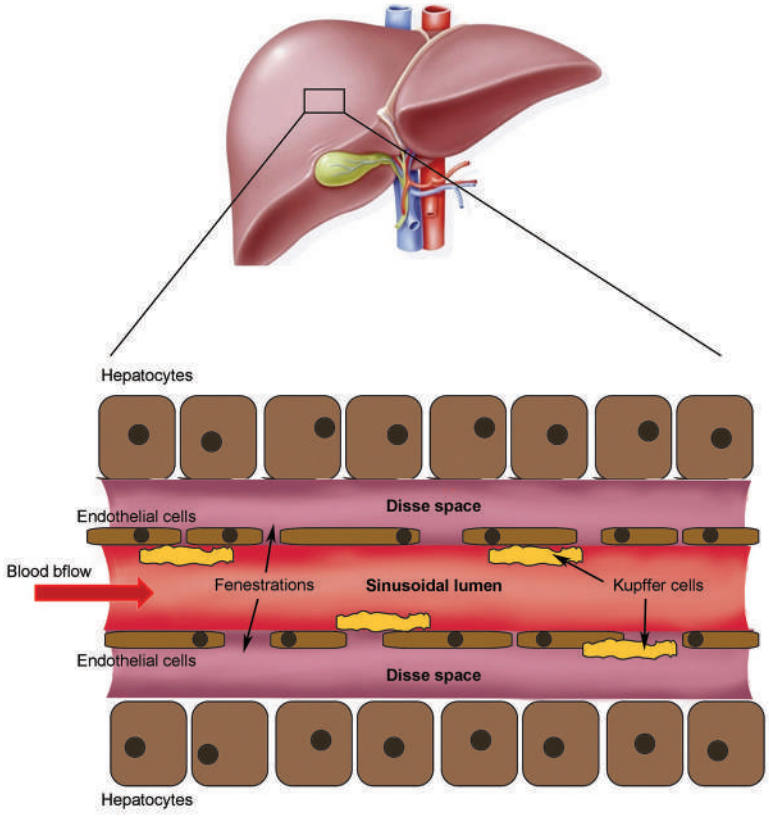

Figure 10. Liver and structure of liver sinusoid. Above: diagram of the liver. Below: diagram of liver sinusoid. The sinusoid capillaries mainly contain sinusoidal endothelial cells (70%) and resident liver macrophages known as the Kupffer cells (20%). Particles up to ~230 nm of diameter can be internalized by the sinusoidal endothelial cells that break the particles down or transfer them to the space of Disse. Bigger particles are phagocytized by Kupffer cells and are degraded in phagolysosomes before being eliminated by exocytosis (Image adapted from http://www.amfe.fr/maladies/description-du-foie/)

cells (resident liver macrophages) represent the most abundant cells in the sinusoids and have an important role in the clearance of nanoparticles [90-92]. The sinusoidal endothelial cell can internalize the particles up to ~230 nm of diameter, break them down or transfer them to the space of Disse [92, 93]. Bigger particles are phagocytized by Kupffer cells instead [94], degraded in phagolysosomes and eliminated by exocytosis [95].

The liver is the organ that generally shows the highest uptake of nanoparticles [73] and is the first organ responsible for the depletion of carrier from the circulation and for reduction of tumor availability. Reducing the liver clearance might therefore be an efficient method to increase bio-availability and the targeting potential of nanocarrier (Figure 10).

The spleen is the second organ involved in the clearance of nanoparticles [96]. It is a lymphoid organ that is highly vascularized and contributes to the clearance of senescent erythrocytes, cellular debris and opsonized microorganisms from the circulation. It is anatomically organized in two distinct areas, the white pulp and red pulp. The white pulp is close to the arteries, and is involved in the proliferation of lymphocytes and in adaptive immunity. The red pulp is mainly represented by vascular sinusoids with a specific sieve structure [67, 97]; it is also the area where the splenic macrophages are located. When the blood passes through the splenic sinusoids of the red pulp, this specific structure promotes a sieving of the blood and the retention of unhealthy cells, pathogens and debris. The presence of macrophages further

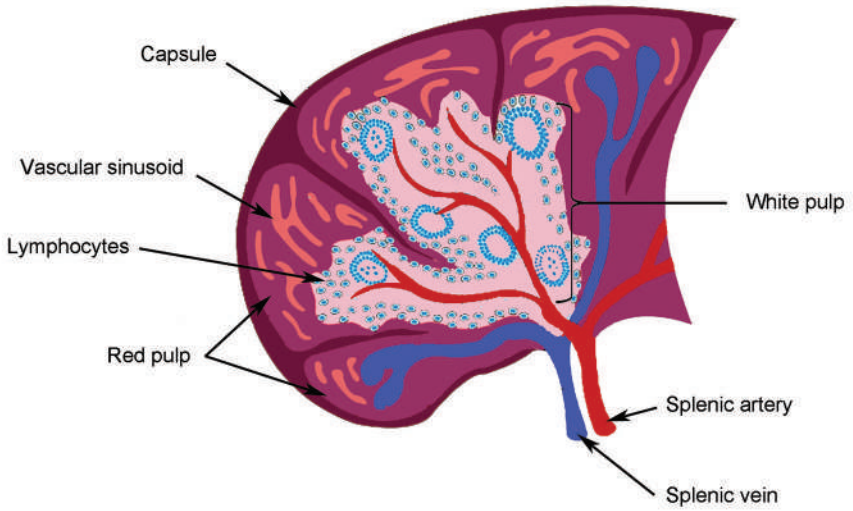

Figure 11. Schematic representation of spleen structure. The blood reaches the red pulp in the spleen via the splenic artery that further branches into smaller vessels, with a sinusoidal structure. Blood cells pass through the sinusoids in the red pulp. Blood is then sieved by a specific structure that results in removal of unhealthy blood cells, pathogens and debris and particles above 200 nm in diameter from the blood.

favors the elimination of senescent erythrocytes or pathogens from the circulation and helps to keep the sieve structure clean [96] (Figure 11). Spherical carriers, above 200 nm in diameter, can be retained for long time in the spleen. Shape of particles also seems to play a significant role during the sieving through the spleen and recent studies showed that elongated, irregular and stiff structured particles are also highly retained [74].

Similarly, to what occurs in the liver, the spleen is also responsible for the depletion of nanoparticles from the circulation. A reduction of splenic uptake by specific changes in the structure of carriers might have a positive effect on the level of particles reaching the tumor and might significantly influence the delivery of agents for imaging or therapy.

Thesis outline

This thesis describes the biodistribution and tumor uptake of novel molecular or supramolecular carriers, for imaging, therapy and image-guided surgery.

The in vivo behavior of targeting, peptide-based carriers is described in **Chapter 2**.

In **Chapter 2.1** we described that octreotate, a somatostatin analogue, was used to synthetize a multimodally labeled derivative that we tested in vivo in preclinical studies.

Radiolabeled somatostatin analogues are being used successfully in the clinic to deliver therapeutic (or theranostic) radionuclides to tumor lesions. Radionuclide therapy with radiolabeled somatostatin analogues might be further improved by tuning parameters such as the treatment scheme and/or the administered specific activity. The effect of variation in these parameters on tumor responses is described in **Chapter 2.2**.

Nanoparticles represent a very versatile delivery platform for different agents, including radionuclides. In **Chapter 3** we describe the potential of two different types of nanoparticles for tumor targeting.

Pluronics P94 are linear amphiphilic block-copolymers that can be applied for tumor delivery. **Chapter 3.1** describes the effects of different injection routes on the distribution of Pluronics P94.

In **Chapter 3.2** and **Chapter 3.3** we describe the synthesis and the in vivo application of nanoparticles derived from spontaneously aggregated of PS-b-PEO block copolymer.

REFERENCES

1. Weinberg, R.A., How cancer arises. Sci Am, 1996. 275(3): p. 62-70.
2. Stewart, B.W., et al., Cancer prevention as part of precision medicine: 'plenty to be done'. Carcinogenesis, 2016. 37(1): p. 2-9.
3. White, M.C., et al., Age and cancer risk: a potentially modifiable relationship. Am J Prev Med, 2014. 46(3 Suppl 1): p. 029.
4. Bernier, J., E.J. Hall, and A. Giaccia, Radiation oncology: a century of achievements. Nat Rev Cancer, 2004. 4(9): p. 737-47.
5. Wyld, L., R.A. Audisio, and G.J. Poston, The evolution of cancer surgery and future perspectives. Nat Rev Clin Oncol, 2015. 12(2): p. 115-24.
6. Mitra, A., et al., Nanocarriers for nuclear imaging and radiotherapy of cancer. Curr Pharm Des, 2006. 12(36): p. 4729-49.
7. Mitragotri, S., et al., Drug Delivery Research for the Future: Expanding the Nano Horizons and Beyond. Journal of Controlled Release, 2017. 246: p. 183-184.
8. Okarvi, S.M. and H.R. Maecke, Peptides for Nuclear Medicine Therapy: Chemical Properties and Production, in Therapeutic Nuclear Medicine, R.P. Baum, Editor 2014, Springer Berlin Heidelberg: Berlin, Heidelberg. p. 105-123.
9. de Jong, M., J. Essers, and W.M. van Weerden, Imaging preclinical tumour models: improving translational power. Nat Rev Cancer, 2014. 14(7): p. 481-93.
10. Kónya, J. and N.M. Nagy, 2 - Basic Concepts, in Nuclear and Radiochemistry2012, Elsevier: Oxford. p. 13-26.
11. Kramer-Marek, G. and J. Capala, The role of nuclear medicine in modern therapy of cancer. Tumor Biology, 2012. 33(3): p. 629-640.
12. Varga, J., 12 - An Introduction to Nuclear Medicine, in Nuclear and Radiochemistry2012, Elsevier: Oxford. p. 351-374.
13. Rowland, D.J. and S.R. Cherry, Small-animal preclinical nuclear medicine instrumentation and methodology. Semin Nucl Med, 2008. 38(3): p. 209-22.
14. Patton, J.A. and T.G. Turkington, SPECT/CT physical principles and attenuation correction. J Nucl Med Technol, 2008. 36(1): p. 1-10.
15. Belcari, N. and A. Del Guerra, La gamma-camera, in Fondamenti di medicina nucleare: Tecniche e applicazioni, D. Volterrani, G. Mariani, and P.A. Erba, Editors. 2010, Springer Milan: Milano. p. 213-232.
16. Rahmim, A. and H. Zaidi, PET versus SPECT: strengths, limitations and challenges. Nucl Med Commun, 2008. 29(3): p. 193-207.
17. Ziegler, S.I., Positron Emission Tomography: Principles, Technology, and Recent Developments. Nuclear Physics A, 2005. 752: p. 679-687.
18. Maurer, A.H., Combined imaging modalities: PET/CT and SPECT/CT. Health Phys, 2008. 95(5): p. 571-6.
19. Imam, S.K., Advancements in cancer therapy with alpha-emitters: a review. Int J Radiat Oncol Biol Phys, 2001. 51(1): p. 271-8.

20. Langer, M. and A.G. Beck-Sickinger, Peptides as carrier for tumor diagnosis and treatment. Curr Med Chem Anticancer Agents, 2001. 1(1): p. 71-93.
21. Psimadas, D., et al., Molecular nanomedicine towards cancer: (1)(1)(1)In-labeled nanoparticles. J Pharm Sci, 2012. 101(7): p. 2271-80.
22. Gudkov, S.V., et al., Targeted Radionuclide Therapy of Human Tumors. Int J Mol Sci, 2015. 17(1).
23. Benuck, M. and N. Marks, Differences in the degradation of hypothalamic releasing factors by rat and human serum. Life Sci, 1976. 19(8): p. 1271-6.
24. Rai, U., et al., Therapeutic uses of somatostatin and its analogues: Current view and potential applications. Pharmacology & Therapeutics, 2015. 152: p. 98-110.
25. Bakker, W.H., et al., Iodine-131 labelled octreotide: not an option for somatostatin receptor therapy. Eur J Nucl Med, 1996. 23(7): p. 775-81.
26. Krenning, E.P., et al., Somatostatin receptor scintigraphy with indium-111-DTPA-D-Phe-1-octreotide in man: metabolism, dosimetry and comparison with iodine-123-Tyr-3-octreotide. J Nucl Med, 1992. 33(5): p. 652-8.
27. De Jong, M., et al., Internalization of radiolabelled [DTPA0]octreotide and [DOTA0,Tyr3]octreotide: peptides for somatostatin receptor-targeted scintigraphy and radionuclide therapy. Nucl Med Commun, 1998. 19(3): p. 283-8.
28. Valkema, R., et al., Phase I study of peptide receptor radionuclide therapy with [In-DTPA]octreotide: the Rotterdam experience. Semin Nucl Med, 2002. 32(2): p. 110-22.
29. Lammers, T., et al., Drug targeting to tumors: principles, pitfalls and (pre-) clinical progress. J Control Release, 2012. 161(2): p. 175-87.
30. Barbieri, F., et al., Peptide receptor targeting in cancer: the somatostatin paradigm. Int J Pept, 2013. 926295(10): p. 7.
31. Reubi, J.C. and B. Waser, Concomitant expression of several peptide receptors in neuroendocrine tumours: molecular basis for in vivo multireceptor tumour targeting. Eur J Nucl Med Mol Imaging, 2003. 30(5): p. 781-93.
32. Narayanan, S. and P.L. Kunz, Role of somatostatin analogues in the treatment of neuroendocrine tumors. J Natl Compr Canc Netw, 2015. 13(1): p. 109-17; quiz 117.
33. Wolin, E.M., The expanding role of somatostatin analogs in the management of neuroendocrine tumors. Gastrointest Cancer Res, 2012. 5(5): p. 161-8.
34. Eriksson, B. and K. Oberg, Summing up 15 years of somatostatin analog therapy in neuroendocrine tumors: future outlook. Ann Oncol, 1999. 10 Suppl 2: p. S31-8.
35. Kjaer, A. and U. Knigge, Use of radioactive substances in diagnosis and treatment of neuroendocrine tumors. Scand J Gastroenterol, 2015. 50(6): p. 740-7.
36. Kwekkeboom, D.J. and E.P. Krenning, Peptide Receptor Radionuclide Therapy in the Treatment of Neuroendocrine Tumors. Hematol Oncol Clin North Am, 2016. 30(1): p. 179-91.
37. Brabander, T., et al., Peptide receptor radionuclide therapy of neuroendocrine tumours. Best Pract Res Clin Endocrinol Metab, 2016. 30(1): p. 103-14.
38. Breeman, W.A., et al., Overview of Development and Formulation of (1)(7)(7)Lu-DOTA-TATE for PRRT. Curr Radiopharm, 2016. 9(1): p. 8-18.

39. Bison, S.M., et al., Peptide receptor radionuclide therapy using radiolabeled somatostatin analogs: focus on future developments: Clin Transl Imaging. 2014;2:55-66. Epub 2014 Mar 5.
40. Melis, M., et al., Localisation and mechanism of renal retention of radiolabelled somatostatin analogues. Eur J Nucl Med Mol Imaging, 2005. 32(10): p. 1136-43.
41. Berne, R.M., B.M. Koeppen, and B.A. Stanton, Berne & Levy physiology2010, Philadelphia, PA: Mosby/Elsevier.
42. Rolleman, E.J., et al., Somatostatin receptor subtype 2-mediated uptake of radiolabelled somatostatin analogues in the human kidney. Eur J Nucl Med Mol Imaging, 2007. 34(11): p. 1854-60.
43. Bodei, L., et al., Long-term tolerability of PRRT in 807 patients with neuroendocrine tumours: the value and limitations of clinical factors. Eur J Nucl Med Mol Imaging, 2015. 42(1): p. 5-19.
44. Kam, B.L., et al., Lutetium-labelled peptides for therapy of neuroendocrine tumours. Eur J Nucl Med Mol Imaging, 2012. 39 Suppl 1: p. S103-12.
45. Bodei, L., et al., Measurement of circulating transcripts and gene cluster analysis predicts and defines therapeutic efficacy of peptide receptor radionuclide therapy (PRRT) in neuroendocrine tumors. Eur J Nucl Med Mol Imaging, 2016. 43(5): p. 839-51.
46. de Jong, M., et al., Inhibition of renal uptake of indium-111-DTPA-octreotide in vivo. J Nucl Med, 1996. 37(8): p. 1388-92.
47. Rolleman, E.J., et al., Safe and effective inhibition of renal uptake of radiolabelled octreotide by a combination of lysine and arginine. Eur J Nucl Med Mol Imaging, 2003. 30(1): p. 9-15.
48. Santini, C., et al., Evaluation of a Fluorescent and Radiolabeled Hybrid Somatostatin Analog In Vitro and in Mice Bearing H69 Neuroendocrine Xenografts. J Nucl Med, 2016. 57(8): p. 1289-95.
49. Banerjee, S.R. and M.G. Pomper, Clinical applications of Gallium-68. Appl Radiat Isot, 2013. 76: p. 2-13.
50. Gulec, S.A. and R. Baum, Radio-guided surgery in neuroendocrine tumors. J Surg Oncol, 2007. 96(4): p. 309-15.
51. García-Talavera, P., et al., Radioguided surgery in neuroendocrine tumors. A review of the literature. Revista Española de Medicina Nuclear e Imagen Molecular (English Edition), 2014. 33(6): p. 358-365.
52. Hussain, T. and Q.T. Nguyen, Molecular imaging for cancer diagnosis and surgery. Adv Drug Deliv Rev, 2014. 66: p. 90-100.
53. van Leeuwen, F.W., J.C. Hardwick, and A.R. van Erkel, Luminescence-based Imaging Approaches in the Field of Interventional Molecular Imaging. Radiology, 2015. 276(1): p. 12-29.
54. van Dam, G.M., et al., Intraoperative tumor-specific fluorescence imaging in ovarian cancer by folate receptor-alpha targeting: first in-human results. Nat Med, 2011. 17(10): p. 1315-9.
55. Keereweer, S., et al., Optical image-guided cancer surgery: challenges and limitations. Clin Cancer Res, 2013. 19(14): p. 3745-54.
56. Bunschoten, A., et al., Multimodal interventional molecular imaging of tumor margins and distant metastases by targeting alphavbeta3 integrin. Chembiochem, 2012. 13(7): p. 1039-45.
57. Jennings, L.E. and N.J. Long, 'Two is better than one'--probes for dual-modality molecular imaging. Chem Commun, 2009. 28(24): p. 3511-24.
58. Van Den Berg, N.S., et al., Hybrid tracers for sentinel node biopsy. Q J Nucl Med Mol Imaging, 2014. 58(2): p. 193-206.

59. van der Poel, H.G., et al., Intraoperative laparoscopic fluorescence guidance to the sentinel lymph node in prostate cancer patients: clinical proof of concept of an integrated functional imaging approach using a multimodal tracer. Eur Urol, 2011. 60(4): p. 826-33.
60. Schaafsma, B.E., et al., Clinical trial of combined radio- and fluorescence-guided sentinel lymph node biopsy in breast cancer. Br J Surg, 2013. 100(8): p. 1037-44.
61. Terwisscha van Scheltinga, A.G., et al., Intraoperative near-infrared fluorescence tumor imaging with vascular endothelial growth factor and human epidermal growth factor receptor 2 targeting antibodies. J Nucl Med, 2011. 52(11): p. 1778-85.
62. Brouwer, O.R., et al., Feasibility of sentinel node biopsy in head and neck melanoma using a hybrid radioactive and fluorescent tracer. Ann Surg Oncol, 2012. 19(6): p. 1988-94.
63. Xing, Y., et al., Radiolabeled nanoparticles for multimodality tumor imaging. Theranostics, 2014. 4(3): p. 290-306.
64. Arranja, A., et al., SPECT/CT Imaging of Pluronic Nanocarriers with Varying Poly(ethylene oxide) Block Length and Aggregation State. Mol Pharm, 2016. 13(3): p. 1158-65.
65. Bolkestein, M., et al., Investigation of Factors Determining the Enhanced Permeability and Retention Effect in Subcutaneous Xenografts. J Nucl Med, 2016. 57(4): p. 601-7.
66. Laan, A.C., et al., Radiolabeling polymeric micelles for in vivo evaluation: a novel, fast, and facile method. EJNMMI Res, 2016. 6(1): p. 016-0167.
67. Bertrand, N. and J.C. Leroux, The journey of a drug-carrier in the body: an anatomo-physiological perspective. J Control Release, 2012. 161(2): p. 152-63.
68. Matsumura, Y. and H. Maeda, A new concept for macromolecular therapeutics in cancer chemotherapy: mechanism of tumoritropic accumulation of proteins and the antitumor agent smancs. Cancer Res, 1986. 46(12 Pt 1): p. 6387-92.
69. Batrakova, E.V. and A.V. Kabanov, Pluronic block copolymers: evolution of drug delivery concept from inert nanocarriers to biological response modifiers. J Control Release, 2008. 130(2): p. 98-106.
70. Lilletvedt, M., et al., Solubilization of the novel anionic amphiphilic photosensitizer TPCS 2a by nonionic Pluronic block copolymers. Eur J Pharm Sci, 2011. 43(3): p. 180-7.
71. Kabanov, A.V., E.V. Batrakova, and V.Y. Alakhov, Pluronic block copolymers as novel polymer therapeutics for drug and gene delivery. J Control Release, 2002. 82(2-3): p. 189-212.
72. Batrakova, E.V., et al., Sensitization of cells overexpressing multidrug-resistant proteins by pluronic P85. Pharm Res, 2003. 20(10): p. 1581-90.
73. Kiessling, F., et al., Nanoparticles for imaging: top or flop? Radiology, 2014. 273(1): p. 10-28.
74. Jennings, L., et al., In vivo biodistribution of stable spherical and filamentous micelles probed by high-sensitivity SPECT. Biomater Sci, 2016. 10: p. 10.
75. Mikhail, A.S. and C. Allen, Poly(ethylene glycol)-b-poly(ε-caprolactone) Micelles Containing Chemically Conjugated and Physically Entrapped Docetaxel: Synthesis, Characterization, and the Influence of the Drug on Micelle Morphology. Biomacromolecules, 2010. 11(5): p. 1273-1280.
76. Miyata, K., R.J. Christie, and K. Kataoka, Polymeric micelles for nano-scale drug delivery. Reactive and Functional Polymers, 2011. 71(3): p. 227-234.
77. Kwon, G.S. and T. Okano, Polymeric micelles as new drug carriers. Advanced Drug Delivery Reviews, 1996. 21(2): p. 107-116.

78. Weis, S.M. and D.A. Cheresh, Tumor angiogenesis: molecular pathways and therapeutic targets. Nat Med, 2011. 17(11): p. 1359-70.
79. Herbert, S.P. and D.Y. Stainier, Molecular control of endothelial cell behaviour during blood vessel morphogenesis. Nat Rev Mol Cell Biol, 2011. 12(9): p. 551-64.
80. Yuan, F., et al., Vascular permeability in a human tumor xenograft: molecular size dependence and cutoff size. Cancer Res, 1995. 55(17): p. 3752-6.
81. Hashizume, H., et al., Openings between defective endothelial cells explain tumor vessel leakiness. Am J Pathol, 2000. 156(4): p. 1363-80.
82. Ruoslahti, E., Specialization of tumour vasculature. Nat Rev Cancer, 2002. 2(2): p. 83-90.
83. Konno, T., et al., Selective targeting of anti-cancer drug and simultaneous image enhancement in solid tumors by arterially administered lipid contrast medium. Cancer, 1984. 54(11): p. 2367-74.
84. Dreher, M.R., et al., Tumor vascular permeability, accumulation, and penetration of macromolecular drug carriers. J Natl Cancer Inst, 2006. 98(5): p. 335-44.
85. Wickline, S.A., et al., Applications of nanotechnology to atherosclerosis, thrombosis, and vascular biology. Arterioscler Thromb Vasc Biol, 2006. 26(3): p. 435-41.
86. Wisse, E., An electron microscopic study of the fenestrated endothelial lining of rat liver sinusoids. J Ultrastruct Res, 1970. 31(1): p. 125-50.
87. Wisse, E., An ultrastructural characterization of the endothelial cell in the rat liver sinusoid under normal and various experimental conditions, as a contribution to the distinction between endothelial and Kupffer cells. J Ultrastruct Res, 1972. 38(5): p. 528-62.
88. Wisse, E., et al., The size of endothelial fenestrae in human liver sinusoids: implications for hepatocyte-directed gene transfer. Gene Ther, 2008. 15(17): p. 1193-9.
89. Synnes, M., et al., Fluid phase endocytosis and galactosyl receptor-mediated endocytosis employ different early endosomes. Biochim Biophys Acta, 1999. 15(2): p. 317-28.
90. Blouin, A., R.P. Bolender, and E.R. Weibel, Distribution of organelles and membranes between hepatocytes and nonhepatocytes in the rat liver parenchyma. A stereological study. J Cell Biol, 1977. 72(2): p. 441-55.
91. Jacobs, F., E. Wisse, and B. De Geest, The role of liver sinusoidal cells in hepatocyte-directed gene transfer. Am J Pathol, 2010. 176(1): p. 14-21.
92. Poisson, J., et al., Liver sinusoidal endothelial cells: Physiology and role in liver diseases. J Hepatol, 2017. 66(1): p. 212-227.
93. Braet, F. and E. Wisse, Structural and functional aspects of liver sinusoidal endothelial cell fenestrae: a review. Comp Hepatol, 2002. 1(1): p. 1.
94. Bergelson, J.M., et al., Isolation of a common receptor for Coxsackie B viruses and adenoviruses 2 and 5. Science, 1997. 275(5304): p. 1320-3.
95. Naito, M., et al., Differentiation and function of Kupffer cells. Med Electron Microsc, 2004. 37(1): p. 16-28.
96. Abbas, A.K., A.H. Lichtman, and S. Pillai, Cellular and molecular immunology2012, Philadelphia: Elsevier/Saunders.
97. Mebius, R.E. and G. Kraal, Structure and function of the spleen. Nat Rev Immunol, 2005. 5(8): p. 606-16.

CHAPTER 2

SOMATOSTATIN ANALOGUES: NOVEL APPROACHES FOR CANCER CURE

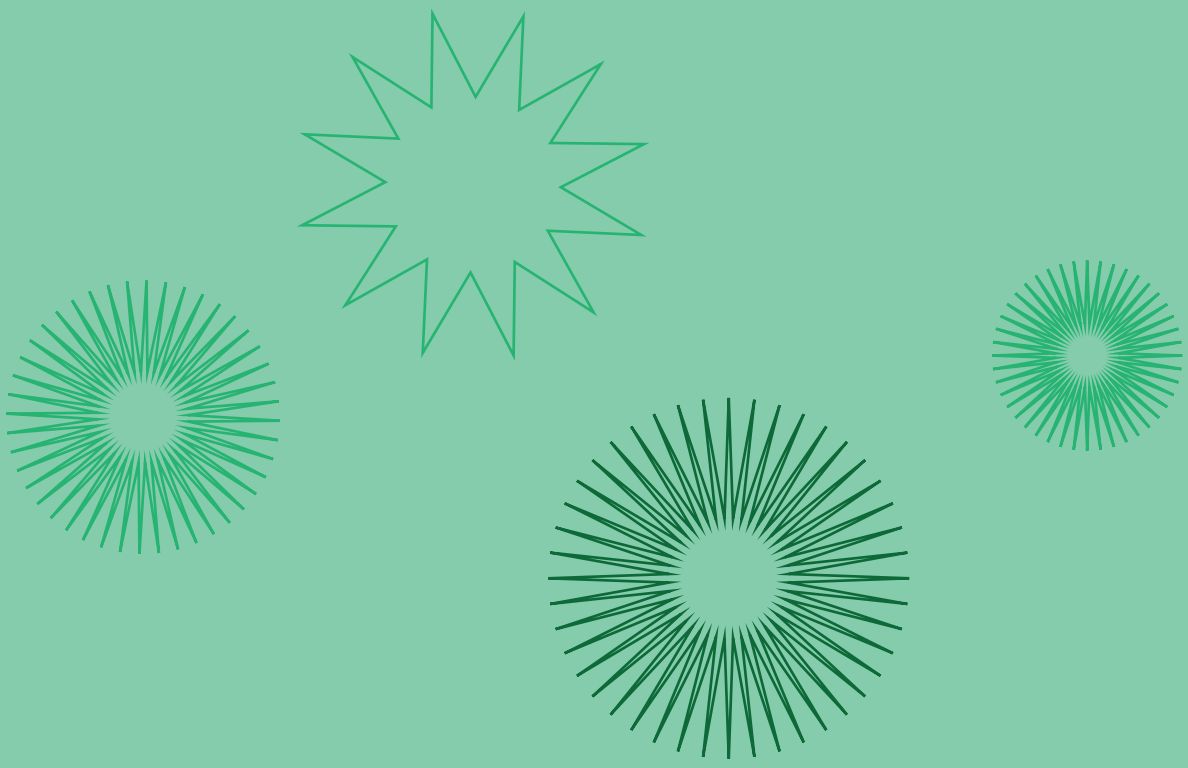

CHAPTER 2.1

Evaluation of a fluorescent and radiolabeled hybrid somatostatin analogue in vitro and in mice bearing H69 neuroendocrine xenografts

Published in Journal of Nuclear Medicine

Santini C, Kuil J, Bunschoten A, Pool S, de Blois E, Ridwan Y, Essers J, Bernsen MR, van Leeuwen FW, de Jong M

J Nucl Med. 2016 Aug;57(8):1289-95. doi:10.2967/jnumed.115.164970. Epub 2016 Apr 28. PubMed PMID: 27127222

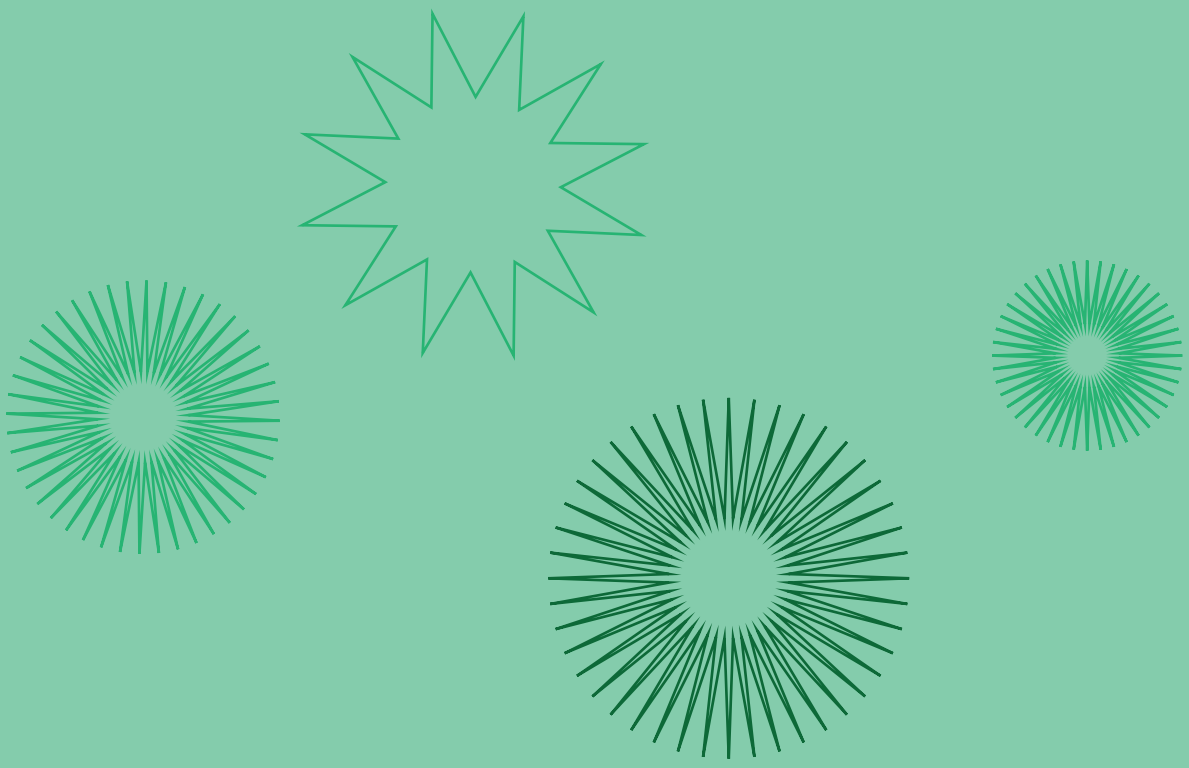

ABSTRACT

In the treatment of neuroendocrine tumors (NET), complete surgical removal of malignancy is generally desirable, as it offers curative results. Pre-operative guidance with radiolabeled somatostatin analogues, commonly used for NET diagnosis and pre-operative planning, is limited by its low resolution, with the risk that tumor margins and small metastases will be incompletely resected with subsequent recurrence. A single hybrid probe combining radiotracer and optical dye would enable high-resolution optical guidance, also during surgery. In the current study, the hybrid labeled somatostatin analogue Cy5-DTPA-Tyr^3-octreotate was synthesized and evaluated for its ability to specifically trace NET cells in vitro and in an animal model. The performance of the hybrid tracer was compared to that of octreotate with only radiolabel or only optical label.

Methods: The binding affinity and internalization capacity of Cy5-DTPA-Tyr^3-octreotate were assessed in vitro. Biodistribution profiles and both nuclear and optical in vivo imaging of Cy5-^{111}In -DTPA-Tyr^3-octreotate were performed in NET-bearing mice and compared to the performance of ^{111}In-DTPA-Tyr^3-octreotate.

Results: In vitro studies showed low receptor affinity and internalization rate for Cy5-DTPA-Tyr^3-octreotate. The K_D value was 387.7 ± 97.9 nM for Cy5-DTPA-Tyr^3-octreotate, while it was 120.5 ± 18.1 nM for DTPA-Tyr^3-octreotate. Similarly, receptor-mediated internalization reduced from 33.76 ± 1.22% applied dose (AD) for DTPA-Tyr^3-octreotate to 1.32± 0.02% AD for Cy5-DTPA-Tyr^3-octreotate. In contrast, in vivo and ex vivo studies revealed similar tumor uptake values of Cy5-^{111}In -DTPA-Tyr^3-octreotate and ^{111}In -DTPA-Tyr^3-octreotate (6.93 ± 2.08 and 5.16 ± 1.27, respectively). All organs except the kidneys showed low background radioactivity, with especially low activities in the liver, and high tumor/tissue ratios were achieved—both favorable for the tracer's toxicity profile. Hybrid imaging in mice confirmed that the nuclear and fluorescence signals co-localized.

Conclusion: The correlation between findings with the optical and the nuclear probes underlines the potential of combining SPECT-imaging with fluorescence guidance and shows the promise of this novel hybrid peptide for pre-operative and intra-operative imaging of NET.

Keywords: image-guided surgery, octreotate, neuroendocrine tumors, multimodal imaging

INTRODUCTION

Neuroendocrine tumors (NET) are rare neoplasms originating from endocrine cells and are known to overexpress the somatostatin receptor (sst). Of the five sst subtypes described, subtype 2 (sst_2) is the most commonly overexpressed in NET (*1*). Radiolabeled somatostatin peptide analogues, such as octreotide and Tyr^3-octreotate, have high affinity for the sst_2 receptor (*2*). They have been used successfully in diagnosing patients with NET using nuclear imaging technologies, such as Single-Photon Emission Computed Tomography (SPECT) or Positron Emission Tomography (PET), in combination with computed tomography (CT). They have also been used successfully for peptide receptor radionuclide therapy in patients with metastasized disease (*2,3*), although surgical resection of the tumor tissue, if possible, is the preferred treatment for NET (*4,5*).

Efficient tumor detection can considerably improve pre-operative planning and result in better patient survival. In current clinical practice, ^{68}Ga and ^{111}In are common radiolabels used in the pre-operative evaluation of lesions using PET- or SPECT- based imaging, respectively (*6*).

The introduction of portable gamma probes enabled real-time radioguidance during surgery (*7-9*). Nevertheless, radioguidance cannot determine tumor margins nor identify small metastases very accurately (*4,10*). The poor visual discrimination between tumor and healthy tissues raises the chance of an incomplete resection, associated with disease progression or recurrence (*10*).

Fluorescence imaging is an alternative technology for intraoperative guidance (*11*), that provides higher resolution and real-time optical detection of the tumor. However, photon attenuation limits tissue penetration to less than one centimeter (*12*); therefore, deep lesions cannot be identifies based on fluorescence signal alone (*10,13,14*).

The simultaneous use of optical and nuclear imaging modalities with their complementary strengths can improve surgical guidance and consequently resection outcome, as has been shown for sentinel node detection and resection (*15*).Dual-modality (or rather hybrid) radiocolloids offer two read-outs during surgery: the nuclear signal can roughly indicate the target location pre- and intra- operatively, and the fluorescence signal gives real-time, (sub) mm resolution during surgery, allowing accurate identification and precise resection.

Can this concept also be applied to tumor resection? Tumor-specific tracers, such as the peptide analogues mentioned above, are essential (*10,12*), and two strategies can be followed. One strategy involves co-injection of two single-labeled targeting agents, i.e. one agent carrying a fluorescent dye and one agent carrying a nuclear label. Alternatively, fluorescent and

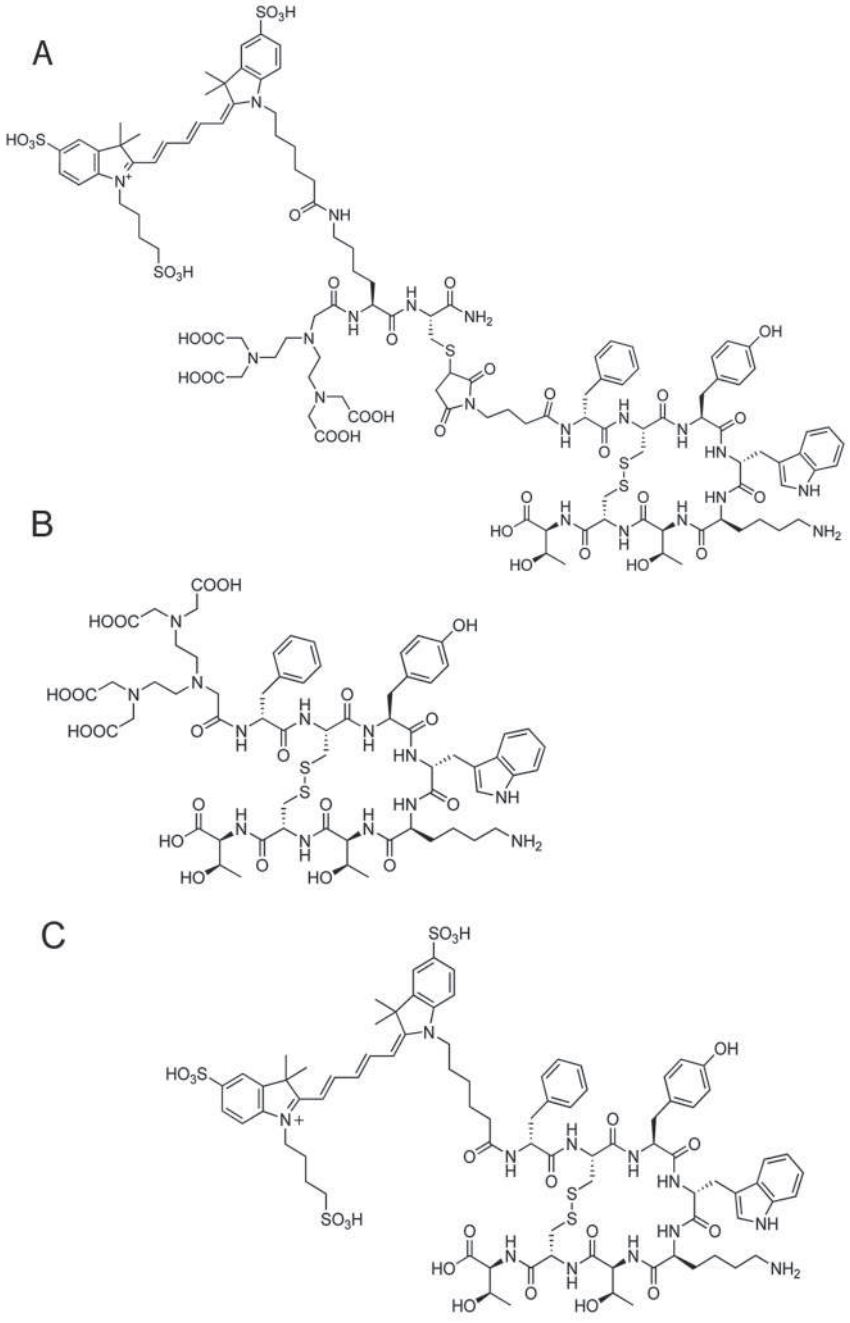

Figure 1. Structures of (A) Cy5-DTPA-Tyr^3-octreotate; (B) DTPA-Tyr^3-octreotate; (C) Cy5-Tyr^3-octreotate.

nuclear labels can both be attached to one targeting moiety, creating an imaging agent with two functionalities. The main drawback of the first strategy is the potentially different biodistribution profile of the two tracers, which could mean a mismatch between nuclear and optical signals (*10*). In contrast, the second strategy will provide automatic co-localization of the two signals. Such dual functionalization can be achieved by introducing two separate imaging labels onto each peptide or by introducing a single, hybrid label containing both functionalities (*16*). With the double-labeling approach, many previous studies with peptide-based tracers have demonstrated a substantial reduction in peptide-receptor affinity, including tracers based on somatostatin analogues (*16,17*). However, hybrid-label-modified tracers maintain a considerable level of receptor affinity both in vitro and in vivo (*16-18*). To the best of our knowledge, however, none of the hybrid-labelled somatostatin analogues have been tested for targeted imaging in vivo.

In this study we have investigated the tumor targeting potential of a newly synthetized somatostatin analogue, the hybrid tracer Cy5-DTPA-Tyr^3-octreotate (Fig. 1A), in vitro and in vivo. The tracer carries, on a single platform, the chelator diethylene triamine pentaacetic acid (DTPA), which chelates radiometals constituting the nuclear beacon, and the fluorescent cyanine dye Cy5 (λ_{ex}=650 nm; λ_{em}=670 nm) as optical label. This tracer was compared with the more traditional somatostatin analogue DTPA-Tyr^3-octreotate (Fig. 1B) and the fluorescently labeled Cy5 Tyr^3-octreotate (Fig. 1C).

MATERIALS AND METHODS

Synthesis

Cy5-DTPA hybrid label. Cy5 was synthesized following a previously described procedure (*19*). The hybrid imaging label was synthesized using solid-phase peptide synthesis. After Fmoc deprotection (20% piperidine in dimethylformamide (DMF)), Fmoc-Lys(IvDde)-OH (2 equivalents (eq.)) was coupled overnight using PyBOP (2eq.), HOBt (2 eq.), DiPEA (4 eq.) in DMF. After subsequent deprotection of the N-terminus, DTPA $(tBu)_4$ (1.3 eq.) was coupled overnight using PyBOP (1.3 eq.), HOBt (1.3 eq.), DiPEA (3 eq.) in DMF . Next, the IvDde protecting group was removed with 2% hydrazine hydrate in DMF. Then Cy5 (1.3 eq.) was coupled overnight using PyBOP (1.3 eq.), HOBt (1.3 eq.), DiPEA (10 eq.) in DMF. The hybrid label was deprotected and cleaved from the resin by treatment with trifluoroacetic acid (TFA) (92.5%), ethylenediamine (2.5%), TiS (2.5%) and water (2.5%) for 2 h. Subsequently, the compound was precipitated in cold methyl-tert-butyl-ether/hexane (1:1), dissolved in 20% CH_3CN in H_2O, and lyophilized. The crude intermediate was used for the next reaction where a reactive linker was introduced. N-succinimidyl-4-maleimidobutyrate (2 eq.) was re-

acted with the free thiol of the cysteine in dimethylsulfoxide with DiPEA (4 eq.). 30 mg of the crude product was purified by reversed-phase HPLC using a gradient of 0.1% TFA in H_2O/CH_3CN 95:5 to 0.1% TFA in H_2O/CH_3CN 5:95 in 40 minutes. Fractions containing the right mass were pooled and lyophilized to yield 9.5 mg of a blue fluffy solid. MS: $[M+H]^+$ calculated 1650.5, found 1651.5.

Synthesis of DTPA-Tyr^3-octreotate, Cy5-Tyr^3-octreotate, and Cy5-DTPA-Tyr^3-octreotate.

Resin-bound D-Phe-Cys(Acm)-Tyr(tBu)-D-Trp(Boc)-Lys(Boc)-Thr(tBu)-Cys(Acm)-Thr(t-Bu)(**1**) was synthesized as previously described (*20*) and further specified in Supplementary Information. Peptidyl resin **1** (25 μmol) was swollen in CH_2Cl_2. Depending on the peptide under synthesis, different concentrations of DTPA-tetra (t-Bu ester), Cy5, or Cy5-DTPA hybrid label was added to the mixture with different concentrations of peptide coupling agents in DMF. The mixture was stirred overnight at room temperature. The resin was then washed with DMF (3×) and CH_2Cl_2 (3×) and dried under vacuum. DTPA-Tyr^3-octreotate, Cy5-Tyr^3-octreotate, or Cy5-DTPA-Tyr^3-octreotate (as appropriate) was cleaved from the resin, and the side chains were de-protected with a solution of TFA/H_2O/TIS 90:5:1.5 (5 mL) for 3 h. The resin was removed from the solution by filtration. The peptides were precipitated with MTBE/hexane 1:1 v/v at -20 °C and lyophilized from CH_3CN/H_2O 1:1 v/v yielding 21.7 mg of crude peptide for DTPA-Tyr^3-octreotate, 25.7 mg for Cy5-Tyr^3-octreotate, and 25.5 mg for Cy5-DTPA-Tyr^3-octreotate. The peptides were purified by preparative HPLC using a gradient of 0.1% TFA in H_2O/CH_3CN 9:1 to 0.1% TFA in H_2O/CH_3CN 1:9 in 60 minutes (DTPA-Tyr^3-octreotate, Cy5-Tyr^3-octreotate) or 120 min (Cy5-DTPA-Tyr^3-octreotate). After pooling of the appropriate fractions and lyophilisation, 4.4 mg of pure DTPA-Tyr^3-octreotate, 6.8 mg of pure Cy5-Tyr^3-octreotate, and 1 mg of pure Cy5-DTPA-Tyr^3-octreotate was obtained. Further details can be found in the Supplementary Information.

Tyr^3-octreotate.

Tyr^3-octreotate was purified from the crude yield of Cy5-DTPA-Tyr^3-octreotate. The peptide was isolated with preparative HPLC using a gradient of 0.1% TFA in H_2O/CH_3CN 9:1 to 0.1% TFA in H_2O/CH_3CN 1:9 in 180 minutes.

Labeling with ^{111}In and ^{125}I

For the binding affinity study, Tyr^3-octreotate was labeled with ^{125}I following the chloramine T/method as previously described (*21*). For ^{111}In radiolabeling, DTPA-Tyr^3-octreotate or Cy5-DTPA-Tyr^3-octreotate were mixed with $^{111}InCl_3$ (1 eq.) and dissolved in 0.1 M of acetic acid. Labeling was performed as previously described (*22*) and further specified in the Supplementary Information.

In vitro studies

Fluorescence-based flow cytometry and binding assay. The dissociation constant (K_D) was determined by a fluorescence-based flow cytometry assay described previously (*23*). C204 Luc 189 RR cells were trypsinized and aliquoted in portions of 300,000 cells. For saturation binding experiments, each aliquot received 50 µL of 0.1% bovine serum albumin (BSA) in phosphate buffered saline (PBS), containing concentrations of Cy5-Tyr^3-octreotate, Cy5-DTPA-Tyr^3-octreotate, or Cy5-In-DTPA-Tyr^3-octreotate ranging between 0 – 10^3 nM. For competition binding experiments, each aliquot received 50 µL of 0.1% BSA in PBS containing 100 nM of Cy5-DTPA-Tyr^3-octreotate as well as 10^{-1} – $3*10^4$ nM of Tyr^3-octreotate, DTPA-Tyr^3-octreotate, or In-DTPA-Tyr^3-octreotate. Cells were incubated for 1 h at 4 °C, after which they were washed twice with 300 µL of 0.1% BSA in PBS and re-suspended in 300 µL of 0.1% BSA in PBS. Fluorescence was measured using a BD FACSCanto II flow cytometer with APC settings (633 nm laser, 660/20 nm filter). Live cells were gated on a Forward Scatter/Side Scatter plot, and 20,000 live cells were analyzed. All experiments were performed in duplicate.

Internalization study.

Rat pancreatic sst_2-expressing CA20948 tumor cells were isolated as previously described (*24*) and seeded in six-well plates ($0.5*10^6$ cells/well). After 24 h, cells were incubated with Cy5-^{111}In-DTPA-Tyr^3-octreotate or ^{111}In-DTPA-Tyr^3-octreotate for 1 h at 37 °C (per well: 0.035 nmol, 100 MBq/nmol). Specific binding was assessed for both tracers by co-incubation with a 100-fold molar excess of unlabeled peptide. The data was analyzed as previously described (*25*).

In vivo/ex vivo studies

Tumor model. Human small cell lung cancer H69 cells (ECACC, Salisbury, UK) were cultured under standard conditions in Gibco's RPMI medium (Invitrogen, Breda, The Netherlands) supplemented with 10% v/v fetal bovine serum and 1% v/v penicillin/streptomycin. Prior to tumor inoculation, $2.3*10^6$ cell/mL were suspended in 2:1 v/v Seligmann's buffered salt solution medium and Matrigel (BD Biosciences, Mississauga, Canada). The suspension was inoculated subcutaneously in 25 young adult male Balb/c-nu mice (Janvier, France) (100 µL/mouse). Tumor growth was monitored three-times/week. When tumors reached ~300 mm^3, animals were divided into four groups with similar distributions of tumor volumes: two groups of 8 animals for nuclear investigations and two of 4/5 mice each for optical and multimodal studies.

All animal experiments were performed in accordance with Dutch animal welfare regulations and approved by the local ethics committee.

SPECT/CT imaging and nuclear-based biodistribution.

Eight mice were given an intravenous injection of Cy5-^{111}In-DTPA-Tyr^3-octreotate (per animal: 200 pmol, 30 MBq, 200 µL); another 8 were given an injection of ^{111}In-DTPA-Tyr^3-octreotate (per animal: 200 pmol, 30 MBq, 200 µL). Animals were anesthetized with a mixture of isoflurane (Pharmachemie BV, Haarlem, The Netherlands; 4% for induction and 1.5% for maintenance) and oxygen and scanned for 30 min with SPECT/CT at 2 and 24 h pi (NanoSPECT/CT, Bioscan, Washington DC, USA). Further information is available in the Supplementary Information.

After the last scan, animals were euthanized by cervical dislocation, and blood was immediately collected by heart puncture. Several organs and the tumor were harvested and weighed. Radioactivity was measured with a gamma counter (Wallac, 1480 Wizard 3"; PerkinElmer, Groningen, The Netherlands). Uptake was calculated as percentage of injected dose (% ID/g).

Optical-based and multimodal imaging. For optical and multimodal analyses, 5 mice were injected with Cy5-^{111}In-DTPA-Tyr^3-octreotate (per animal: 200 pmol, 30 MBq, 200 µL) and another 4 mice with Cy5-Tyr^3-octreotate (per animal 200 pmol, 200 µL). All mice were imaged at 24 h pi, using a fluorescence tomography device (FMT, 2500XL, PerkinElmer Inc., Boston, MA). The mice injected with Cy5-Tyr^3-octreotate were euthanized immediately after the fluorescence tomography scan, the skin around the tumor was removed, and the tumor was

scanned with an IVIS imaging system (Perkin Elmer). The mice injected with Cy5-^{111}In-DTPA-Tyr^3-octreotate underwent SPECT/CT scanning at 24 h pi before being euthanized. Further information is available in the Supplementary Information.

Data analysis and statistical methods

All data collected were processed with Prism version 5 (GraphPad Software, La Jolla, California, USA). A two-tailed Student's t test was used, and $p<0.05$ was considered statistically significant.

RESULTS

Binding affinity

Data obtained from the fluorescence-based binding assays were used to generate concentration-binding curves of the various compounds (Fig. 2) and to calculate their K_D and IC_{50} values. See Table 1 and the Supplementary Information for more details. Based on both K_D and IC_{50} values, we observed a reduced receptor binding affinity for the peptide derivatives tested: unlabeled Tyr^3-octreotate > DTPA-Tyr^3-octreotate > Cy5-^{111}In-DTPA-Tyr^3-octreotate.

In vitro tumor uptake

Internalization efficacy of Cy5-^{111}In-DTPA-Tyr^3-octreotate was assessed in comparison to the nuclear-only tracer ^{111}In-DTPA-Tyr^3-octreotate (Fig. 3). First, the total uptake, measured as fraction of the applied dose (AD), that was retained in the cells was evaluated. For ^{111}In-DTPA-Tyr^3-octreotate and Cy5-^{111}In-DTPA-Tyr^3-octreotate the total uptake was 33.76 ± 1.22% AD and 1.32 ± 0.02% AD, respectively (Fig. 3).

Second, we distinguished between the internalized (cell fraction) and the membrane bound fraction (membrane fraction). For ^{111}In-DTPA-Tyr^3-octreotate the cell fraction and the membrane fractions were 30.76 ± 1.02% AD and 3.49 ± 0.3% AD respectively, whereas the values for Cy5-^{111}In-DTPA-Tyr^3-octreotate were 1.21 ± 0.03% AD and 0.12 ± 0.001%

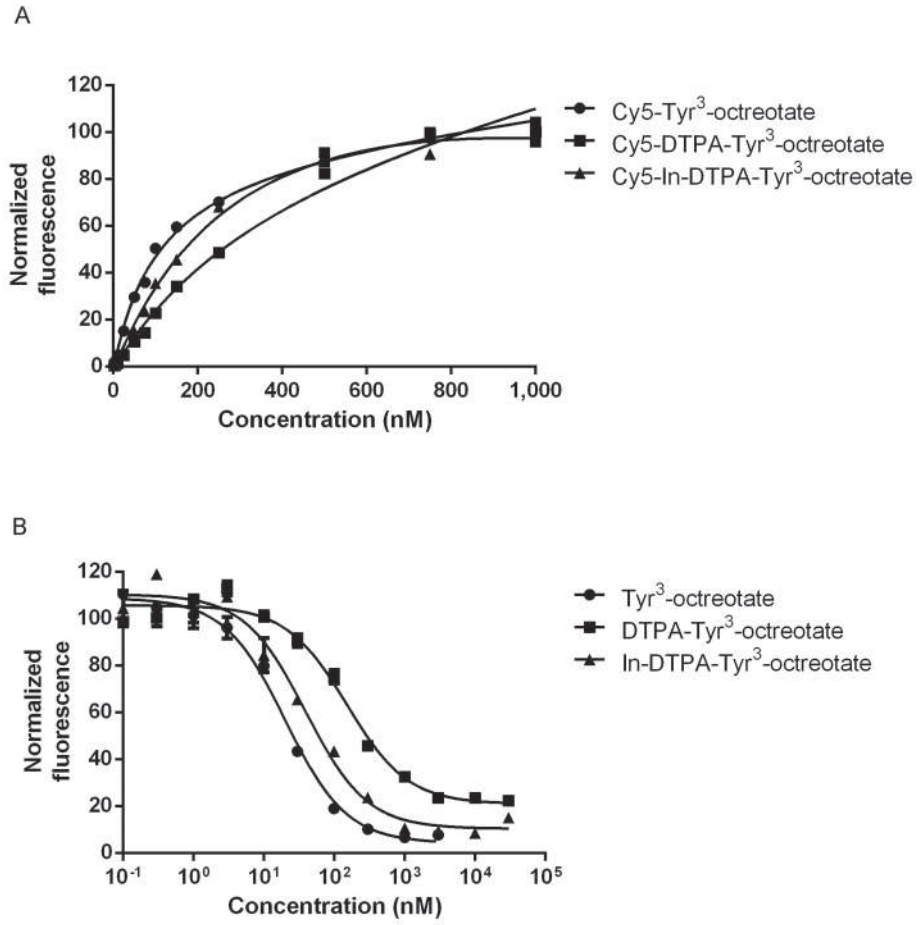

Figure 2. (A) Fluorescence-based flow cytometry saturation binding assay of Cy5-Tyr^3-octreotate, Cy5-DTPA-Tyr^3-octreotate and Cy5-In-DTPA-Tyr^3-octreotate; (B) Fluorescence-based flow cytometry competition binding assay. Cy5-DTPA-Tyr^3-octreotate was used as the ligand to be displaced at increasing concentration of Tyr^3-octreotate, DTPA-Tyr^3-octreotate, and In-DTPA-Tyr^3-octreotate.

AD, respectively. Co-incubation with an excess of DTPA-Tyr^3-octreotate or Cy5-DTPA-Tyr^3-octreotate unlabeled peptide ('block') significantly reduced total uptake to 0.15% AD for ^{111}In-DTPA-Tyr^3-octreotate and to 0.04% AD for Cy5-^{111}In-DTPA-Tyr^3-octreotate, indicating receptor specificity for both tracers (Fig. 3).

Calculating the percentage of internalized tracer versus the total uptake gave similar values for both tracers (Table 2), revealing that the two tracers have very similar kinetics once bound to the receptor.

Table 1: Receptor binding parameters of different tracers, K_D and IC_{50} values expressed in nM.

	K_D ± sd (nM)	IC_{50} (nM),(95% CI (nM))
Tyr^3-octreotate	16.2 ± 1.6	20.35 (16.8-24.7)
DTPA-Tyr^3-octroetate	120.5 ± 18.1	151.5 (112.6-204.0)
In-DTPA-Tyr^3-octreotate	31.2 ± 5.4	39.3 (28.0-55.1)
Cy5-Tyr^3-octreotate	106.1 ± 11.7	133.4 (107.5-159.5)
Cy5-DTPA-Tyr^3-octreotate	387.7± 97.9	487.7 (400.6-574.8)
Cy5-In-DTPA-Tyr^3-octreotate	415.0 ± 90.0	522.0 (399.2-644.9)

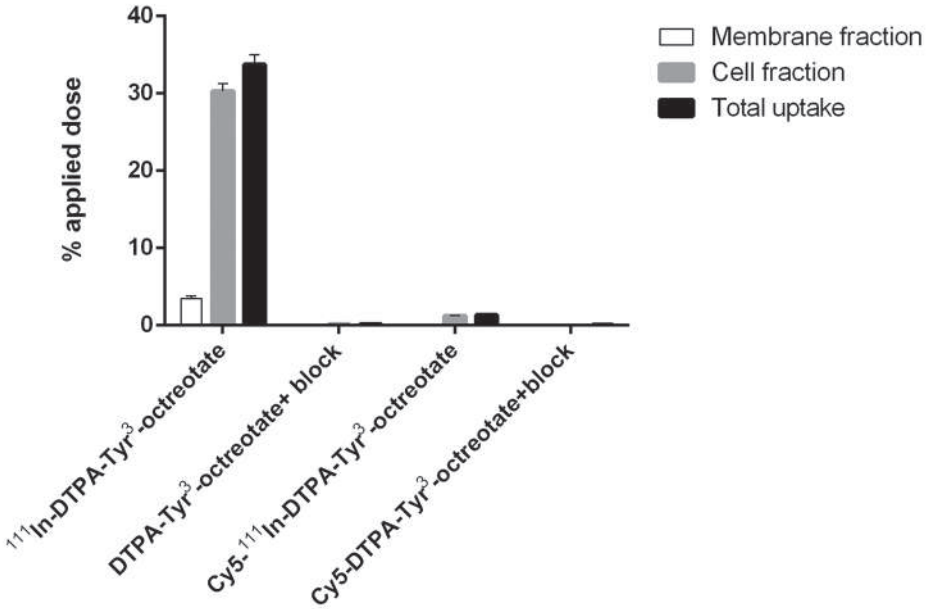

Figure 3. Uptake of ^{111}In-DTPA-Tyr^3-octreotate and Cy5-^{111}In-DTPA-Tyr^3-octreotate by CA20948 cells.

Table 2. Radioactivity in membrane fraction and cell fraction ^{111}In-DTPA-Tyr^3-octreotate and Cy5-^{111}In-DTPA-Tyr^3-octreotate expressed as % of total uptake.

	Membrane Fraction	Cell Fraction
	Mean ± sd (% total uptake)	Mean ± sd (% total uptake)
^{111}In-DTPA-Tyr^3-octreotate	10.33 ± 0.67	89.67 ± 0.70
Cy5-^{111}In-DTPA-Tyr^3-octreotate	8.86 ± 0.97	91.14 ± 0.97

In vivo/ex vivo: tumor uptake and nuclear-based biodistribution

SPECT/CT images at different time points indicate highly similar in vivo behavior of ^{111}In-DTPA-Tyr^3-octreotate and Cy5-^{111}In-DTPA-Tyr^3-octreotate, both showing substantial uptake in the tumor and in the kidneys, but generally low radioactivity in background organs (Fig. 4). Interestingly, radioactivity was not detectable in the liver, indicating low hepatic retention for both tracers. In vivo quantification of kidney and tumor radioactivity is shown in Fig. 4E: the data confirmed Cy5-DTPA-Tyr^3-octreotate to accumulate both in the kidney and in the tumor.

Ex vivo biodistribution data of ^{111}In-DTPA-Tyr^3-octreotate and Cy5-^{111}In-DTPA-Tyr^3-octreotate agreed with the pattern observed with the SPECT/CT scans, showing low accumulation (<2% ID/g) in organs other than the kidneys (Table 3). Noticeably, liver levels were extremely low. For kidneys, a high and consistent retention was visible: 14.25 ± 2.79% ID/g for ^{111}In-DTPA-Tyr^3-octreotate and 52.21 ± 7.85% ID/g for Cy5-^{111}In-DTPA-Tyr^3-octreotate. Despite the fact that receptor affinity of the hybrid tracer was signifi-

Table 3. Biodistribution (in %ID/g) and Tumor/Tissue Ratios (TTR) of ^{111}In-DTPA-Tyr^3-octreotate and Cy5-^{111}In-DTPA-Tyr^3-octreotate at 24 h pi.

	^{111}In-DTPA-Tyr^3-octreotate		**Cy5-^{111}In-DTPA-Tyr^3-octreotate**	
	mean ± sd (%ID/g)	TTR	mean ± sd (%ID/g)	TTR
Blood	0.02 ± 0.03	313.84	0.07 ± 0.03	93.72
Spleen	0.11 ± 0.03	46.6	0.56 ± 0.04	12.36
Pancreas	0.29 ± 0.07	17.99	1.90 ± 0.85	3.65
Liver	0.12 ± 0.03	41.97	0.51 ± 0.04	13.57
Kidney	14.15 ± 2.79	0.37	52.21 ± 7.85	0.13
Adrenals	0.40 ± 0.30	12.99	0.62 ± 0.27	11.1
Duodenum	0.13 ± 0.05	38.95	0.49 ± 0.19	14.06
Colon	0.38 ± 0.10	13.51	1.30 ± 0.07	5.32
Caecum	0.17 ± 0.04	31.28	0.43 ± 0.04	16.28
Stomach	0.32 ± 0.06	16.12	1.30 ± 0.31	5.32
Muscle	0.03 ± 0.02	168.68	0.11 ± 0.10	61.87
Tumor	5.16 ± 1.27	1	6.93 ± 2.08	1

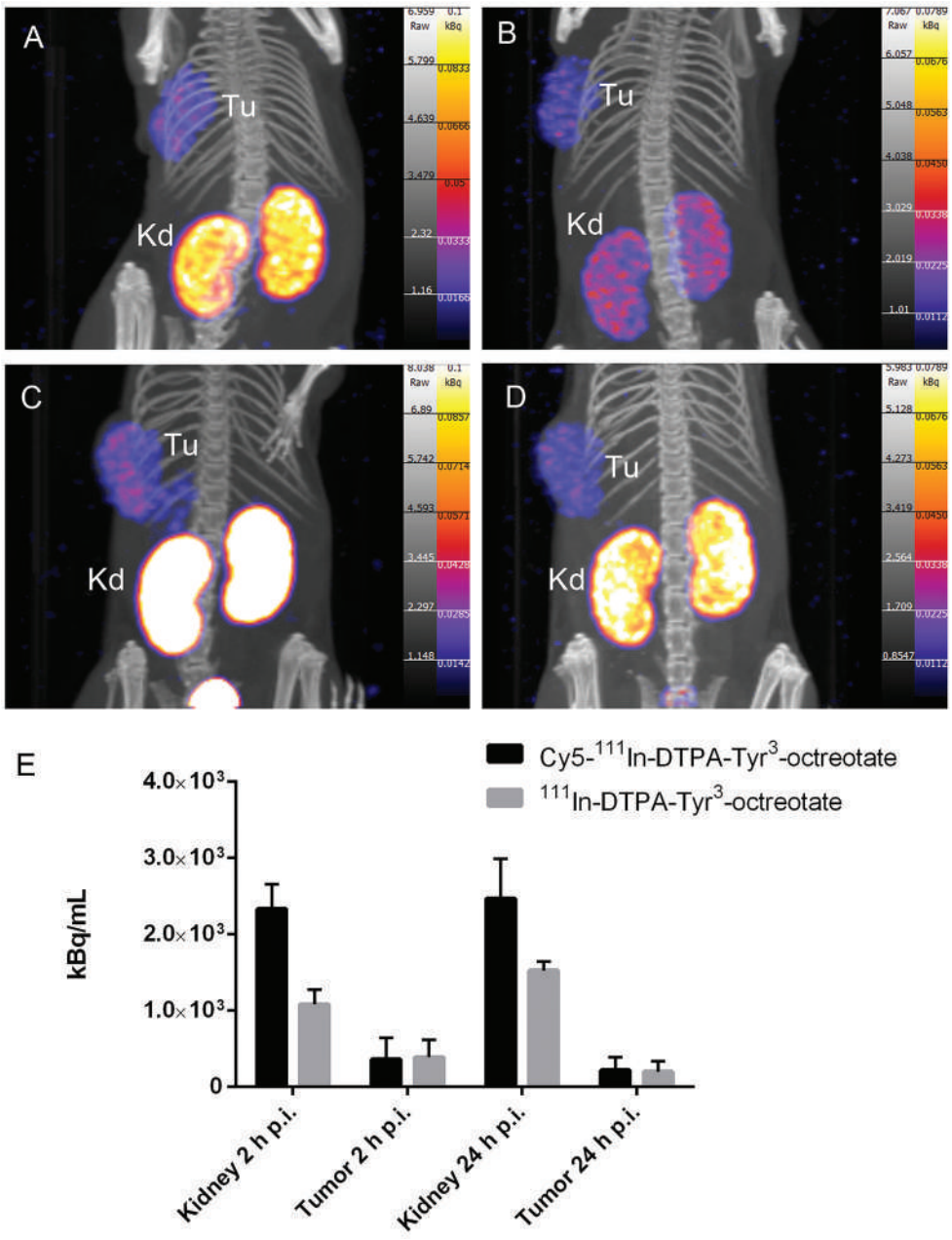

Figure 4. SPECT/CT images of H69 tumor-bearing mice. ^{111}In-DTPA-Tyr^3-octreotate (A) 2 h pi and (B) 24 h pi; Cy5-^{111}In-DTPA-Tyr^3-octreotate (C) 2h pi and (D) 24 h pi; (E) Quantification of tumor and kidney 2 h and 24 h pi; mean for N=8 of calculated uptake ± standard deviation (sd). Kd: Kidney; Tu: Tumor

cantly reduced as measured in vitro, tumor uptake in vivo was relatively high for both tracers (mean ~5% ID/g) and not statistically different ($p>0.05$). The calculated tumor/tissue ratios (TTR)—with the exception of the kidney—were always >3 and usually >10 (Table 3), indicating that tumor specificity was high.

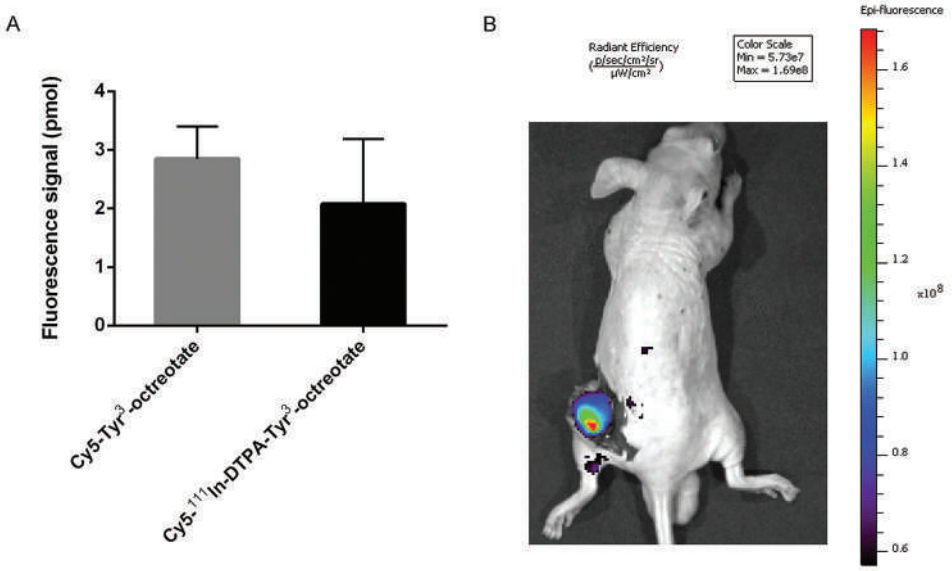

Figure 5. (A) FMT-based quantification of Cy5-^{111}In-DTPA-Tyr^3-octreotate and of Cy5-Tyr^3-octreotate accumulation in the tumor, 24 h pi; (B) Cy5-Tyr^3-octreotate fluorescence imaging via IVIS at 24 h pi, after the removal of the skin from the tumor area.

Optical-based analyses

Tumor uptake was quantified based on the FMT signal, and the results are depicted in Fig. 5A. Optical signal originating from Cy5-^{111}In-DTPA-Tyr^3-octreotate and Cy5-Tyr^3-octreotate is comparable at 24 h pi. The optical image shown in Fig. 5B was obtained with an IVIS imaging system. The image shows a representative mouse of those injected with fluorescently-labeled octreotate and indicates the potential of visualizing tumor tissue and margins in vivo using the fluorescence signal.

Multimodal analyses with Cy5-^{111}In-DTPA-Tyr^3-octreotate

The combined optical and nuclear imaging capability of Cy5-^{111}In-DTPA-Tyr^3-octreotate is shown in Fig. 6. The images indicate that tracer accumulation in the tumor can be detected with both nuclear and optical imaging modalities.

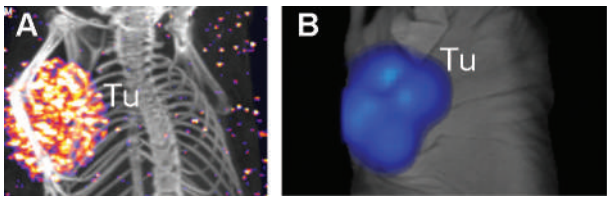

Figure 6. Cy5-^{111}In-DTPA-Tyr^3-octreotate in H69 tumor-bearing mouse 24 h pi: (A) SPECT/CT image; (B) FMT image of tumor region.

DISCUSSION

In NET, where radical tumor resection is often the only curative option, more refined surgical guidance, with the possibility of real-time tumor margin identification, would be highly beneficial for patient survival (*7*). Combined fluorescence–and-nuclear imaging represents an attractive approach to improve guidance as it allows for combined pre- and intra-operative imaging, with high resolution and real-time feedback provided by fluorescence imaging. The correlation we found between optical and nuclear imaging, confirms that the combination of the two techniques is a promising approach for pre- and intra-operative imaging in NET.

One of the main drawbacks of dual-labeled tracers is the potential loss of receptor affinity and in vivo targeting capability which has previously been reported for various dual labeled tracers (*16,17,26,27*). Cy5-^{111}In-DTPA-Tyr^3-octreotate and ^{111}In-DTPA-Tyr^3-octreotate showed comparable profiles when applied in our in vivo model, especially with respect to tumor uptake and limited off-target uptake; the only major difference between ^{111}In-DTPA-Tyr^3-octreotate and Cy5-^{111}In-DTPA-Tyr^3-octreotate was the renal uptake, which was higher with the dual-labeled tracer than with the nuclear-only tracer. It is known that ^{111}In-DTPA-Tyr^3-octreotate is cleared via and partially retained in the kidneys as a result of renal reabsorption in the proximal tubular cells, mostly due to the tracer's molecular composition (*28*). We hypothesize that the three additional negative charges present on Cy5 contributed to the increased renal retention of Cy5-^{111}In-DTPA-Tyr^3-octreotate. A favorable finding concerning the hybrid Cy5-^{111}In-DTPA-Tyr^3-octreotate is the low level of liver uptake, which was comparable to that of ^{111}In-DTPA-Tyr^3-octreotate. High hepatic retention has

been reported for several other hybrid tracers (*16,18*). Such in vivo behavior was explained as a result of the hydrophobic nature of cyanine dye and the large non-covalent interaction with serum albumin that drives increased retention in all tissues, including the high hepatic uptake (*18,29*). In our study, we used a relatively hydrophilic cyanine dye, specifically chosen to reduce the albumin interaction. The three negative charges which are likely responsible for the increased renal retention, therefore also appear to contribute to the limited degree of hepatic clearance. Nonetheless, Cy5-^{111}In-DTPA-Tyr^3-octreotate was retained in the blood stream for longer than the corresponding nuclear-only tracer; such behavior could be explained by an interaction with albumin (*26*). Indeed, in a pilot protein binding study, the serum protein fraction contained more than 30 times as much Cy5-^{111}In-DTPA-Tyr^3-octreotate than the watery fraction of blood (data not shown). The longer circulation time might explain the improved tumor uptake, this longer circulation time resulting from reduced renal filtration and/or by degradation protection. This hypothesis requires further investigation before definitive conclusions can be drawn.

Regarding stability in the bloodstream, peptide molecules are known to be vulnerable to degradation by peptidases (*30*). Nonetheless, radiolabeled DTPA- and DOTA-linked Tyr3-octreotide and Tyr^3-octreotate have exhibited excellent stability in circulation; they are excreted via the urine mostly in the intact form (*30-32*). Therefore, we expect our hybrid Cy5-^{111}In-DTPA-Tyr^3-octreotate peptide analogue to exhibit good stability in circulation as well. Indeed, the Cy5-^{111}In-DTPA-Tyr^3-octreotate biodistribution profile remained comparable with that of ^{111}In-DTPA-Tyr^3-octreotate over time. Moreover, the hybrid probe uptake in tumor could be detected using both nuclear and fluorescent imaging modalities, indicating that the radiolabel and fluorophore on the hybrid probe were not separated during transit to the tumor.

Our results on the hybrid Cy5-^{111}In-DTPA-Tyr^3-octreotate are particularly promising for application to image-guided surgery. For radio- or fluorescence- guided surgery, a significant difference in uptake by tumor and normal tissue is needed for discrimination. A TTR value of 1.5 is generally considered sufficient for radioguidance (*7*), while a TTR value of 3 is thought to be needed for fluorescence guidance (*5*). In our investigation, the nuclear-based TTR was always >3 (except for the kidneys) and usually >10. The low liver retention was particularly favorable for NETs, which are known to preferentially metastasize to the liver. To improve the relatively low (<1 TTR) in the kidneys, thereby making identification of tumor lesions near the kidney feasible, it might be useful to apply methods that have previously been shown to reduce renal uptake of radiolabeled somatostatin analogs, including a hybrid tracer (*33*).

CONCLUSION

We have demonstrated Cy5-^{111}In-DTPA-Tyr^{3}-octreotate can efficiently target sst_2 on tumor tissue in vivo, allowing nuclear and fluorescence detection. Our study provides insight in the influence of the Cy5-DTPA-label on receptor affinity as well as pharmacokinetics of octreotate in vivo. These findings suggest that this hybrid tracer could be a lead-candidate for translation into clinical studies, to achieve more accurate visualization and detection of NETs during surgery.

ACKNOWLEDGEMENTS

This work used imaging equipment provided by the Applied Molecular Imaging Erasmus MC facility. The work was partially supported by a Dutch Cancer Society translational research award (Grant No. PGF 2009-4344), by an NWO-STW-VIDI grant (Grant No. STW-BGT11272), and by the People Program (Marie Curie Actions) of the European Union's Seventh Framework Programme (FP7/2007-2013) under REA grant agreement no. PITN-GA-2012-317019 'TRACE 'n TREAT'.

REFERENCES

1. Reubi JC, Waser B. Concomitant expression of several peptide receptors in neuroendocrine tumours: molecular basis for in vivo multireceptor tumour targeting. *Eur J Nucl Med Mol Imaging.* 2003;30:781-793.
2. Laverman P, Sosabowski JK, Boerman OC, Oyen WJ. Radiolabelled peptides for oncological diagnosis. *Eur J Nucl Med Mol Imaging.* 2012;39 Suppl 1:S78-S92.
3. Bison SM, Konijnenberg MW, Melis M, et al. Peptide receptor radionuclide therapy using radiolabeled somatostatin analogs: focus on future developments. *Clin Transl Imaging.* 2014;2:55-66.
4. Hussain T, Nguyen QT. Molecular imaging for cancer diagnosis and surgery. *Adv Drug Deliv Rev.* 2014;66:90-100.
5. Tummers QR, Boonstra MC, Frangioni JV, van de Velde CJ, Vahrmeijer AL, Bonsing BA. Intraoperative near-infrared fluorescence imaging of a paraganglioma using methylene blue: a case report. *Int J Surg Case Rep.* 2015;6C:150-153.
6. Banerjee SR, Pomper MG. Clinical applications of Gallium-68. *Appl Radiat Isot.* 2013;76:2-13.
7. Gulec SA, Baum R. Radio-guided surgery in neuroendocrine tumors. *J Surg Oncol.* 2007;96:309-315.
8. García-Talavera P, Ruano R, Rioja ME, Cordero JM, Razola P, Vidal-Sicart S. Radioguided surgery in neuroendocrine tumors. A review of the literature. *Revista Española de Medicina Nuclear e Imagen Molecular (English Edition).* 2014;33:358-365.
9. Wang S, Yang W, Deng J, Zhang J, Ma F, Wang J. Reduction in the recurrence of meningiomas by combining somatostatin receptor scintigraphy of (99m)Tc-HYNIC-octreotide SPECT/CT and radio guidance with a hand-held gamma-probe during surgery. *Nucl Med Commun.* 2013;34:249-253.
10. Lutje S, Rijpkema M, Helfrich W, Oyen WJ, Boerman OC. Targeted radionuclide and fluorescence dual-modality imaging of cancer: preclinical advances and clinical translation. *Mol Imaging Biol.* 2014;16:747-755.
11. van Leeuwen FW, Hardwick JC, van Erkel AR. Luminescence-based imaging approaches in the field of Interventional molecular imaging. *Radiology.* 2015;276:12-29.
12. Keereweer S, Van Driel PB, Snoeks TJ, et al. Optical image-guided cancer surgery: challenges and limitations. *Clin Cancer Res.* 2013;19:3745-3754.
13. Azhdarinia A, Ghosh P, Ghosh S, Wilganowski N, Sevick-Muraca EM. Dual-labeling strategies for nuclear and fluorescence molecular imaging: a review and analysis. *Mol Imaging Biol.* 2012;14:261-276.
14. van Oosterom MN, Kreuger R, Buckle T, et al. U-SPECT-BioFluo: an integrated radionuclide, bioluminescence, and fluorescence imaging platform. *EJNMMI Res.* 2014;4:014-0056.
15. Van Den Berg NS, Buckle T, Kleinjan GI, et al. Hybrid tracers for sentinel node biopsy. *Q J Nucl Med Mol Imaging.* 2014;58:193-206.
16. Kuil J, Velders AH, van Leeuwen FW. Multimodal tumor-targeting peptides functionalized with both a radio- and a fluorescent label. *Bioconjug Chem.* 2010;21:1709-1719.
17. Edwards WB, Xu B, Akers W, et al. Agonist-antagonist dilemma in molecular imaging: evaluation of a monomolecular multimodal imaging agent for the somatostatin receptor. *Bioconjug Chem.* 2008;19:192-200.

18. Bunschoten A, Buckle T, Visser NL, et al. Multimodal interventional molecular imaging of tumor margins and distant metastases by targeting alphavbeta3 integrin. *Chembiochem.* 2012;13:1039-1045.
19. Mujumdar RB, Ernst LA, Mujumdar SR, Lewis CJ, Waggoner AS. Cyanine dye labeling reagents: sulfoindocyanine succinimidyl esters. *Bioconjug Chem.* 1993;4:105-111.
20. Mier W, Eritja R, Mohammed A, Haberkorn U, Eisenhut M. Preparation and evaluation of tumor-targeting peptide-oligonucleotide conjugates. *Bioconjug Chem.* 2000;11:855-860.
21. de Blois E, Chan HS, Breeman WA. Iodination and stability of somatostatin analogues: comparison of iodination techniques. A practical overview. *Curr Top Med Chem.* 2012;12:2668-2676.
22. de Blois E, Chan HS, Konijnenberg M, de Zanger R, Breeman WA. Effectiveness of quenchers to reduce radiolysis of (111)In- or (177)Lu-labelled methionine-containing regulatory peptides. Maintaining radiochemical purity as measured by HPLC. *Curr Top Med Chem.* 2012;12:2677-2685.
23. Kuil J, Buckle T, Yuan H, et al. Synthesis and evaluation of a bimodal CXCR4 antagonistic peptide. *Bioconjug Chem.* 2011;22:859-864.
24. Melis M, Bijster M, de Visser M, et al. Dose-response effect of Gelofusine on renal uptake and retention of radiolabelled octreotate in rats with CA20948 tumours. *Eur J Nucl Med Mol Imaging.* 2009;36:1968-1976.
25. de Jong M, Breeman WA, Bakker WH, et al. Comparison of (111)In-labeled somatostatin analogues for tumor scintigraphy and radionuclide therapy. *Cancer Res.* 1998;58:437-441.
26. Kuil J, Buckle T, Oldenburg J, et al. Hybrid peptide dendrimers for imaging of chemokine receptor 4 (CXCR4) expression. *Mol Pharm.* 2011;8:2444-2453.
27. Achilefu S, Jimenez HN, Dorshow RB, et al. Synthesis, in vitro receptor binding, and in vivo evaluation of fluorescein and carbocyanine peptide-based optical contrast agents. *J Med Chem.* 2002;45:2003-2015.
28. Melis M, Krenning EP, Bernard BF, Barone R, Visser TJ, de Jong M. Localisation and mechanism of renal retention of radiolabelled somatostatin analogues. *Eur J Nucl Med Mol Imaging.* 2005;32:1136-1143.
29. Bunschoten A, Buckle T, Kuil J, et al. Targeted non-covalent self-assembled nanoparticles based on human serum albumin. *Biomaterials.* 2012;33:867-875.
30. Nock BA, Maina T, Krenning EP, de Jong M. "To serve and protect": enzyme inhibitors as radiopeptide escorts promote tumor targeting. *J Nucl Med.* 2014;55:121-127.
31. Krenning EP, Bakker WH, Kooij PP, et al. Somatostatin receptor scintigraphy with indium-111-DTPA-D-Phe-1-octreotide in man: metabolism, dosimetry and comparison with iodine-123-Tyr-3-octreotide. *J Nucl Med.* 1992;33:652-658.
32. Vaidyanathan G, Affleck DJ, Zhao XG, Keir ST, Zalutsky MR. [Lu]-DOTA-Tyr-octreotate: A Potential Targeted Radiotherapeutic for the Treatment of Medulloblastoma. *Curr Radiopharm.* 2010;3:29-36.
33. Rolleman EJ, Valkema R, de Jong M, Kooij PP, Krenning EP. Safe and effective inhibition of renal uptake of radiolabelled octreotide by a combination of lysine and arginine. *Eur J Nucl Med Mol Imaging.* 2003;30:9-15.

SUPPLEMENTAL DATA

General on the synthetic procedures

All chemicals were obtained from commercial sources and used without further purification. HPLC was performed on a Waters HPLC system using a 1525EF pump and a 2489 UV detector. For preparative HPLC a Dr. Maisch GmbH Reprosil-Pur 120 C18-AQ 10 µm (250 ´ 20 mm) column was used (12 mL/min). For analytical HPLC a Dr. Maisch GmbH Reprosil-Pur C18-AQ 5 µm (250 ´ 4.6 mm) column was used and a gradient of 0.1% TFA in H_2O/CH_3CN 95:5 to 0.1% TFA in H_2O/CH_3CN 5:95 in 20 minutes (1 mL/min) was employed. Mass spectrometry was performed on a Bruker microflex MALDI-TOF.

Synthesis of Cy5-DTPA hybrid label, Tyr^3-octreotate, DTPA-Tyr^3-octreotate, and Cy5-DTPA-Tyr^3-octreotate

Cy5-DTPA hybrid label Cy5 was synthesized following a procedure described by Mujumdar et al. [1].The hybrid imaging label was synthesized using solid phase peptide synthesis (SPPS). Tentagel S RAM-Cys(Trt)-Fmoc was purchased from RAPP Polymere (Tuebingen, Germany). After Fmoc deprotection (20% piperidine in DMF) Fmoc-Lys(IvDde)-OH (2 equivalents (eq.)) was coupled overnight using PyBOP (2eq.), HOBt (2 eq.), DiPEA (4 eq.) in DMF. After subsequent deprotection of the N-terminus, DTPA $(tBu)_4$ (1.3 eq.) was coupled overnight using PyBOP (1.3 eq.), HOBt (1.3 eq.), DiPEA (3 eq.) in DMF. Next, the IvDde protecting group was removed with 2% hydrazine hydrate in DMF. Then Cy5 (1.3 eq.) was coupled overnight using PyBOP (1.3 eq.), HOBt (1.3 eq.), DiPEA (10 eq.) in DMF. The hybrid label was deprotected and cleaved from the resin by treatment with TFA (92.5%), EDT (2.5%), TIS (2.5%) and H_2O (2.5%) for 2 hours. Subsequently, the compound was precipitated in cold MTBE/hexane (1:1), dissolved in 20% CH_3CN in H_2O and lyophilized. The crude intermediate was used for the next reaction where a reactive linker was introduced. N-succinimidyl-4-maleimidobutyrate (2 eq.) was reacted with the free thiol of the cysteine in DMSO with DiPEA (4 eq.). 30 mg of the crude product was purified by reversed phase HPLC using a gradient of 0.1% TFA in H_2O/CH_3CN 95:5 to 0.1% TFA in H_2O/CH_3CN 5:95 in 40 minutes. Fractions containing the right mass were pooled and lyophilized to yield 9.5 mg of a blue fluffy solid. MS: $[M+H]^+$ calculated 1650.5, found 1651.5.

*cyclo[D-Phe-Cys-Tyr(tBu)-D-Trp(Boc)-Lys(Boc)-Thr(tBu)-Cys-Thr(tBu)]-resin (**1**)* Resin-bound D-Phe-Cys(Acm)-Tyr(tBu)-D-Trp(Boc)-Lys(Boc)-Thr(tBu)-Cys(Acm)-Thr(tBu) was synthesized by SPPS using Fmoc-L-Thr(tBu)-PEG-PS resin (loading 0.16 mmol/g). Standard Fmoc/tBu strategy was used with PyBOP as coupling reagent. The linear side

chain-protected peptide was cyclized on resin using $Tl(TFA)_3$ [2]: the resin-bound peptide (0.1 mmol) was swollen in 3 mL CH_2Cl_2. $Tl(TFA)_3$ (109 mg, 0.2 mmol) in 3 mL DMF was added to the resin and the mixture was stirred for 1 hour at room temperature. The resin was washed with DMF (3×) and CH_2Cl_2 (3×) and dried under vacuum yielding peptidyl resin **1**. The cyclization was confirmed with analytical HPLC by cleavage and deprotection of a small amount of peptide.

DTPA-Tyr³-octreotate Peptidyl resin **1** (25 µmol) was swollen in CH_2Cl_2. DTPA-tetra (t-Bu ester) (46 mg, 75 µmol), PyBOP (39 mg, 75 µmol) and DiPEA (26 µL, 150 µmol) in DMF (3 mL) was added and the mixture was stirred overnight at room temperature. The resin was washed with DMF (3×) and CH_2Cl_2 (3×) and dried under vacuum. The peptide was cleaved from the resin and the side chains were de-protected with a solution of TFA/H_2O/TIS 90:5:1.5 (5 mL) for 3 h. The resin was removed from the solution by filtration. The peptide was precipitated with MTBE/hexane 1:1 v/v at -20 °C and lyophilized from CH_3CN/H_2O 1:1 v/v yielding 21.7 mg of crude peptide. The peptide was purified by preparative HPLC using a gradient of 0.1% TFA in H_2O/CH_3CN 9:1 to 0.1% TFA in H_2O/CH_3CN 1:9 in 60 minutes. After pooling of the appropriate fractions and lyophilisation, 4.4 mg of pure DTPA-Tyr³-octreotate peptide was obtained. MS: $[M+H]^+$ calculated 1425.6, found 1425.6; $[M+Na]^+$ calculated 1447.5, found 1447.9; $[M+K]^+$ calculated 1463.7, found 1463.5.

Cy5-Tyr³-octreotate Peptidyl resin **1** (25 µmol) was swollen in CH_2Cl_2. Cy5 (38 mg, 50 µmol), PyBOP (26 mg, 50 µmol) and DiPEA (17 µL, 100 µmol) in DMF (3 mL) was added and the mixture was stirred overnight at room temperature. The resin was washed with DMF (3×) and CH_2Cl_2 (3×) and dried under vacuum. The peptide was cleaved from the resin and the side chains were deprotected with a solution of TFA/H_2O/TIS 90:5:1.5 (5 mL) for 3 h. The resin was removed from the solution by filtration. The peptide was precipitated with MTBE/hexane 1:1 v/v at -20 °C and lyophilized from CH_3CN/H_2O 1:1 v/v yielding 25.7 mg of crude peptide. The peptide was purified by preparative HPLC using a gradient of 0.1% TFA in H_2O/CH_3CN 9:1 to 0.1% TFA in H_2O/CH_3CN 1:9 in 60 minutes. After pooling of the appropriate fractions and lyophilisation, 6.8 mg of pure Cy5-Tyr³-octreotate peptide was obtained. MS: $[M+H]^+$ calculated 1797.1, found 1798.4.

Cy5-DTPA-Tyr³-octreotate Peptidyl resin **1** (25 µmol) was swollen in CH_2Cl_2. Cy5-DTPA hybrid label (30 mg, 18 µmol) and DiPEA (44 µL, 255 µmol) in DMF (2 mL) was added and the mixture was stirred overnight at room temperature. The resin was washed with DMF (3×) and CH_2Cl_2 (3×) and dried under vacuum. The peptide was cleaved from the resin and the side chains were de-protected with a solution of TFA/H_2O/TIS 90:5:1.5 (5 mL) for 3 h. The resin was removed from the solution by filtration. The peptide was precipitated with MTBE/hexane 1:1 v/v at -20 °C and lyophilized from CH_3CN/H_2O 1:1 v/v yielding 25.5 mg of crude peptide. The peptide was purified by preparative HPLC using a gradient of 0.1% TFA in H_2O/CH_3CN 9:1 to 0.1% TFA in H_2O/CH_3CN 1:9 in 120 minutes. After pooling of the

appropriate fractions and lyophilisation 1 mg of pure Cy5-DTPA-Tyr3-octreoatate peptide was obtained. MS: $[M+H]^+$ calculated 2586.0, found 2586.1.

In vitro experiments

Nuclear based imaging

Nuclear SPECT/CT images for in vivo analyses were acquired using were acquired with a four-headed helical NanoSPECT system (NanoSPECT/CT, Bioscan, Inc, Washington D.C., USA). A multi-pinhole mouse collimator with 9 pinholes (1.4 mm diameter) per head, with a matrix of 256 x 256 was used. The machinery was equipped with a heated bed system to prevent hypothermia in the animals. All animals received a SPECT scan of 24 projections (90 sec per projection) and a CT scan (240 projections, 500 ms exposure time at 55 kV) for anatomical reference. For those mice that received both SPECT/CT and FMT scan the acquisition time of nuclear imaging was reduced to 20 minutes (20 projections, 60 second per projection).

Optical and multimodal imaging

Optical imaging for in vivo analyses was performed using fluorescence tomography device (FMT, 2500XL, PerkinElmer Inc., Boston, MA) and IVIS (Caliper Life Science, Hopkinton, MA, USA). For the tomographic analyses with FMT the mice were placed in a supine position in the imaging cassette, which was inserted into the docking system of the FMT imaging chamber that was saturated with a mixture of isoflurane and oxygen (1.5% and 0.8% respectively) The light source consisted of a laser diode (80mW). The region of interest was drawn around the tumor, to highlight the uptake. The signals were collected at the opposite side of the animal body by a low noise TE-cooled back illuminated high quantum efficiency CCD camera with air assist. Using the preconfigured channel 1 (λ_{ex}=635 nm, λ_{em}=650-670 nm) both fluorescent and excitation data sets were collected and multiple source-detector fluorescence projections were normalized to laser excitation data.

In our protocol, for acquisition of optical images with the IVIS system, the mice were euthanized and placed supine in the chamber. IVIS system is equipped with a tungsten halogen lamp and filters for selection of excitation wavelength. In our evaluation optical images were acquired using an excitation length of 640 nm. The animals were top illuminated by the excitation light and the emission light subsequently filtered at different wavelength from 680 nm to 780 nm (band pass = 20 nm). Acquisition time was approximately 60 second.

Data analysis and statistical methods

The competition studies were fitted using the normalized geometric means were fitted with equations in the GraphPad Prism 5 software. The K_D and IC_{50} values of Cy5-Tyr^3-octreotate, Cy5-DTPA-Tyr^3-octreotate and Cy5-In-DTPA-Tyr^3-octreotate were calculated using the 'Binding – Saturation, One site – Total' nonlinear regression equation (Eq. 1).

$$y = \frac{B_{max} * x}{K_D + x} + NS * x + Background \quad \text{(Eq. 1)}$$

Where, y is the normalized fluorescence; B_{max} is the maximum specific binding in the units of the y axis; x is the concentration of Cy5-Tyr^3-octreotate, Cy5-DTPA-Tyr^3-octreotate or Cy5-In-DTPA-Tyr^3-octreotate in nM; K_D = equilibrium dissociation constant of Cy5-Tyr^3-octreotate, Cy5-DTPA-Tyr^3-octreotate or Cy5-In-DTPA-Tyr^3-octreotate in nM; NS is the slope of nonspecific binding; Background is the amount of normalized fluorescence with no added compound.

The K_D values of Tyr^3-octreotate, DTPA-Tyr^3-octreotate and In-DTPA-Tyr^3-octreotate were calculated using the 'Binding – Competitive, One site – Fit K_i' nonlinear regression equation (Eq. 2 and 3).

$$\log IC_{50} = \log(10^{\log K_D} * (1 + \frac{[a]}{K_{D,a}})) \quad \text{(Eq. 2)}$$

$$y = Bottom + \frac{Top - Bottom}{1 + 10^{(x - \log IC_{50})}} \quad \text{(Eq. 3)}$$

Where IC_{50} is the concentration of competitor that results in binding half-way between Bottom and Top; K_D is the equilibrium dissociation constant of the competitor in nM; [a] is the concentration of Cy5-DTPA-Tyr^3-octreotate (100 nM); $K_{D,a}$ is the dissociation constant of Cy5-DTPA-Tyr^3-octreotate (387.7 nM); y is the normalized fluorescence; Bottom and Top are the plateaus in the units of the y axis.

REFERENCES

1. Mujumdar, R.B., et al., *Cyanine dye labeling reagents: sulfoindocyanine succinimidyl esters.* Bioconjug Chem, 1993. **4**(2): p. 105-11.
2. Mier, W., et al., *Preparation and evaluation of tumor-targeting peptide-oligonucleotide conjugates.* Bioconjug Chem, 2000. **11**(6): p. 855-60.
3. Melis, M., et al., *Dose-response effect of Gelofusine on renal uptake and retention of radiolabelled octreotate in rats with CA20948 tumours.* Eur J Nucl Med Mol Imaging, 2009. **36**(12): p. 1968-76.
4. Hofland, L.J., et al., *Crucial role for somatostatin receptor subtype 2 in determining the uptake of [111In-DTPA-D-Phe1]octreotide in somatostatin receptor-positive organs.* J Nucl Med, 2003. **44**(8): p. 1315-21.

513958-L-sub01-bw-Santini
Processed on: 22-9-2017

CHAPTER 2.2

Treatment planning options for improved ^{177}Lu-DOTA, Tyr^3-octreotate therapeutic response studied in an animal model

Updated versio has been submitted toJournal of Nuclear Medicine

Bison SM, Santini C , Koelewijn SJ, de Blois E, Melis M, de Jong M, Konijnenberg MW

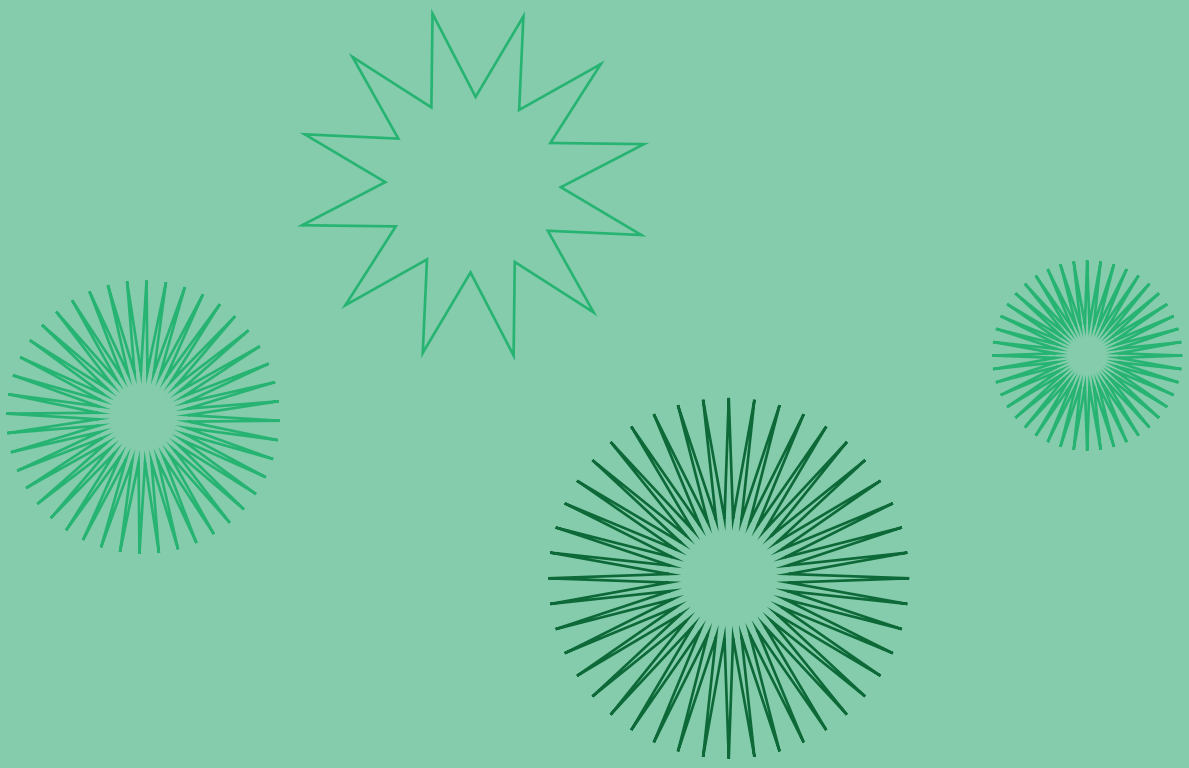

ABSTRACT

Treatment with ^{177}Lu-labelled DOTA, Tyr^3-octreotate (TATE) has been shown to be an excellent treatment for somatostatin receptor-overexpressing neuroendocrine tumours in case surgery, the primary treatment option is not an option anymore. Success full therapy depends on delivering high absorbed doses to the tumour metastases relative to a non-toxic absorbed dose delivered to normal organs. Patient-specific treatment planning aimed at increasing the absorbed tumour dose while also aiming for a tolerance absorbed dose in organs at risk, might enhance the effectiveness of this therapy. The radiobiology of tumour dose-response is described by the linear quadratic model. In theory fractionation of the dose delivered or changes in dose rate will hardly influence the tumour response while they do reduce the risk for radiation induced adverse events. These tumour radiation response effects are the main subject of this study as well as the response effect with time.

Therefore, we have performed experiments in H69 tumour-bearing nude mice, to study the effects of different specific activities on the absorbed doses in the tumour versus normal organs as well as on therapeutic responses. Furthermore, different treatment schemes were studied aiming for the impact of multiple administrations. Finally, all results were compared with calculations using the linear quadratic model to verify its usefulness for prospective treatment planning.

Our results indicated that it is possible to model the anti-tumour response by different dose rates, due to changes in specific activity and fractionation. Both tumour growth as clearance of dead cells over time in response to radiation exposure were introduced into a treatment planning model based on the linear quadratic model. This model appeared to be useful in predicting anti-tumour responses and can be applied to calculate optimal therapy conditions for future patient studies.

Key words: specific activity, multiple dosing, radiobiology, PRRT, neuroendocrine tumor, dosimetry

INTRODUCTION

Peptide receptor radionuclide therapy (PRRT) using radiolabelled peptides specifically targeting receptors overexpressed on tumour cells has been shown to be an effective cancer treatment option (*1*). During PRRT a high radiation dose can be delivered to tumours, with a tolerable toxicity in normal non-targeted tissues such as kidneys and pancreas (*2*).

In more than 50% of the patients, NETs are diagnosed at a relatively late stage, often with metastatic spread, which leaves little chance for curative surgery (*3*). PRRT has proven to be an effective palliative-type of therapy in most patients with NETs even at late stage (*4*). Complete remissions after PRRT are however still rare (*2*), indicating that further optimization of PRRT is urgently needed.

PRRT given at a fixed activity dosing scheme of 4x7.4 GBq ^{177}Lu/192 µg TATE has been proven to be effective in prolonging survival and delaying progression (*2*). Attempts to further improve treatment for each individual patient have been made by individualized treatment planning. This enables possible additional treatment cycles by using patient-specific dosimetry to determine the maximally tolerated activity by dose-limiting organs as kidneys and bone marrow (*5*). The absorbed dose to the metastatic tumour is thereby maximized. As far as we know there is however no evidence these additional treatment cycles do result in an improved response or an increased survival.

Besides the amount of activity, a patient is treated with, also the amount of peptide this activity is labeled to, the so-called specific activity, is of importance when treating patients with PRRT. This as the specific activity has been shown to influence the biodistribution of the radiopharmaceutical in preclinical studies (*6*) as well as in patients. To use this influence for further improved of individualized treatment, physiologically based pharmacokinetic models have been developed to determine the optimal amount of ligand in PRRT (*7*). This model accounts for perfusion and distribution volumes, receptor affinity and specific activity to determine time-activity curves for tumours and organs with normal physiological uptake.

Prospective treatment planning with the aim to reach an efficacious dose in the tumour has not been established yet. By getting an idea of anti-tumour response in time, effects of potential additional treatment cycles can be determined as well as possibilities to reduce toxicity by dose fractionation, as applied for external beam radiation therapy. In external beam radiotherapy, fractionation of the absorbed dose lowers the incidence of normal organ toxicity at comparable therapeutic effects (*8*). The linear quadratic model (LQM) forms the basis for this observation (*8*), and the LQM also plays a role in the dose limit for radiation-induced nephritis after ^{90}Y-DOTATOC therapy (*9*).

In the current study, we performed multiple experiments in SSTR-expressing H69 tumour-bearing nude mice to examine the influence of specific activity of the radiolabelled peptides and of fractionation of the treatment on anti-tumour response. These experiments were primarily used to tailor the linear quadratic model to predict anti-tumour response over time and investigate its value for prospective treatment planning.

MATERIALS AND METHODS

Tumour Cell Line and in vivo tumour model

Human small cell lung cancer cell line H69, overexpressing the somatostatin receptor type 2 (SSTR2) was obtained from ECACC (Salisbury, UK) and grown in RPMI medium (Gibco, Invitrogen Corp., Breda, NL) supplemented with 10% heat-inactivated fetal bovine serum. Male NMRI Nu/nu (Harlan, Heerlen, NL) were inoculated subcutaneously with 10^7 H69 cells in a suspension of 1:2 v/v Seligmann's buffered salt solution and Matrigel (BD Biosciences, Missisauga, CA). Mice and tumour growth were monitored three times per week for three weeks. All animal experiments have been conducted with prior approval of the animal ethics committee of our institution. Further information of animal handling and tumour model can be found in the Supplementary Information (SI).

Radionuclides and peptides

DOTA,Tyr^3-octreotate was obtained from BioSynthema, (St Louis, MO, USA) and $^{177}LuCl_3$ was obtained from IDB Holland (Baarle-Nassau, NL). ^{177}Lu-TATE was prepared as described previously (*10*). Activities of 30 and 26 MBq ^{177}Lu-TATE have been used. These activities resulted in our previous experiments in appropriate anti-tumour responses (*11*).

SPECT/CT imaging

A small-animal SPECT/CT camera (BioScan, Washington DC, USA) was used to image and quantify the distribution of radiolabelled peptides in vivo. See SI for further information on SPECT/CT specifications.

Experimental set-up

The set-up of the experiment is summarized in Table 1. Further details on experimental settings can be found in the SI.

Table 1 Experimental setup

Groups	Treatment	Number of mice
Effect of different specific activity		
Control	Saline	5
0.5 μg peptide	30 MBq ^{177}Lu	20 (8 +12)
1.0 μg peptide	30 MBq ^{177}Lu	20 (8 +12)
2.0 μg peptide	30 MBq ^{177}Lu	20 (8 +12)
Split-dose experiment: Comparison single-dose vs. split-dose		
Control	Saline	8
Single-dose	26 MBq ^{177}Lu/0.7 μg TATE	8
Split-dose	2x 13 MBq ^{177}Lu/0.35 μg TATE (5 d interval)	8
Double-dose experiment: Comparison single-dose vs. double-dose		
Control	Saline	5
One-dose	30 MBq ^{177}Lu/0.825 μg TATE	8
Double-dose	2x30 MBq ^{177}Lu/0.825 μg TATE (14 d interval)	8

TATE: octreotate; d: day(s)

Dosimetry calculations

Dosimetry in normal organs and tumours was performed according to the MIRD-scheme (*12*). Time-activity curves of organ and tumour distribution were determined on the combination of biodistribution data and quantitative SPECT. A more detailed description on "Dosimetry calculation" can be found in SI.

Tumour growth curve fitting and dose-response model (LQM)

The tumour growth curves V(t) were modelled with exponential growth functions from the normal growth equation. The LQM is used to predict the tumour volume as a function of time, taking into account a lag-time in response due to removal kinetics and a fraction of non-responding tumour cells. In SI a more detailed description of the "Tumor growth curve fitting", "Time-dependent tumor response" and on the "Kinetics of radioactivity of ^{177}Lu-TATE" can be found.

Statistics

Data regarding the tumour uptake were analysed with one-way ANOVA, with $p<0.05$ considered as statistically relevant. See further information of statistical method in SI.

RESULTS

Effect of specific activity

In all experimental groups, treated with different peptide amounts of ^{177}Lu-TATE (0.5, 1.0 and 2.0 μg), the highest amount of radioactivity uptake was measured in the tumour (Figure 1A). Stomach and pancreas are normal SSTR2-expressing organs showing a low, but significant amount of ^{177}Lu-TATE uptake (>0.1% IA/g), but not detectable using SPECT/CT imaging (Figure 1B). Clearance of the radiopeptides via the kidneys results in retention of radioactivity, also identifiable in the SPECT/CT scan (Figure 1B). At 7 d pi, tumour uptake was twice as high in the 0.5 μg peptide group as in the other groups. The fit of the curves describing the kinetics of the radioactivity in selected organs was described by single-exponential curves (See Figure S1 in SI).

For all peptide amounts the tumour showed the highest absorbed dose; this resulted in 592±84 mGy/MBq (0.5 μg), 471±130 mGy/MBq (1 μg) and 321±138 mGy/MBq (See Table S1 in SI). The kidneys had the highest absorbed dose in normal tissue: 140±39 mGy/MBq. Only the tumour and the pancreas and stomach showed the maximum absorbed dose in the 0.5 μg group. All other absorbed doses appeared to be similar between the three groups.

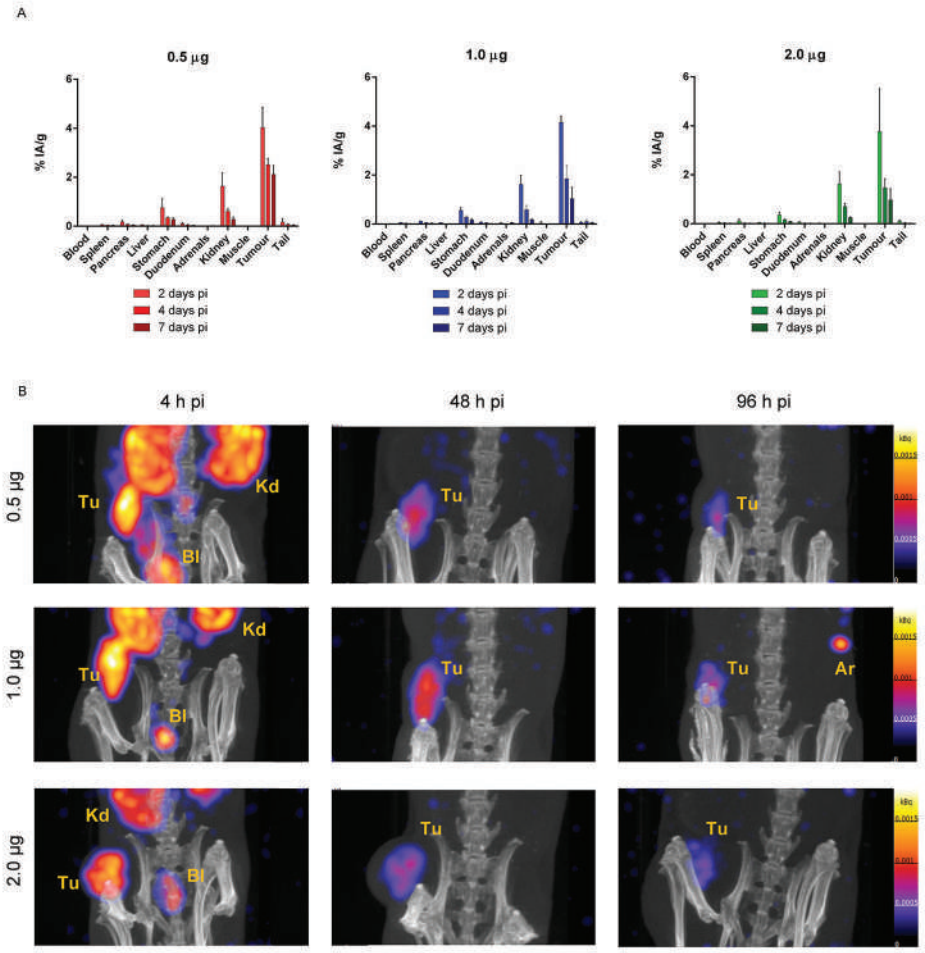

Figure 1. Uptake of ^{177}Lu-TATE applied at different. A: Percentage of injected activity per gram tissue (%IA/g) in tumour and normal organs at 2, 4 and 7 days after administration of 30 MBq ^{177}Lu-TATE: 0.5 µg peptide (red), 1.0 µg peptide (blue), 2.0 µg peptide (green); B: Uptake of radioactivity shown by the SPECT/CT scans (corrected for decay) after injection with 0.5, 1.0, 2.0 µg of ^{177}Lu-TATE. Images are acquired at 4, 48 and 96 h pi. Tu: tumour; Kd: kidney; Bl: bladder; Ar: artefact.

The tumours in the control group showed an exponential growth with a mean doubling time (T_d) of 9±2 d (Figure 2A). After initial response to therapy with a volume nadir at T_1=13±2 d, regrowth occurred in all three experimental groups with a T_d of 9±3 d. The median time to reach a volume above 1800 mm^3 was 13 d (range: 11-34) for the control group, 49 d (range: 38-62) with 0.5 µg, 42 d (range: 24-65) d with 1.0 µg and 31 d (range: 24-42) with 2.0 µg (p=0.002 for 0.5 µg vs 2.0 µg group)(Figure 2B).

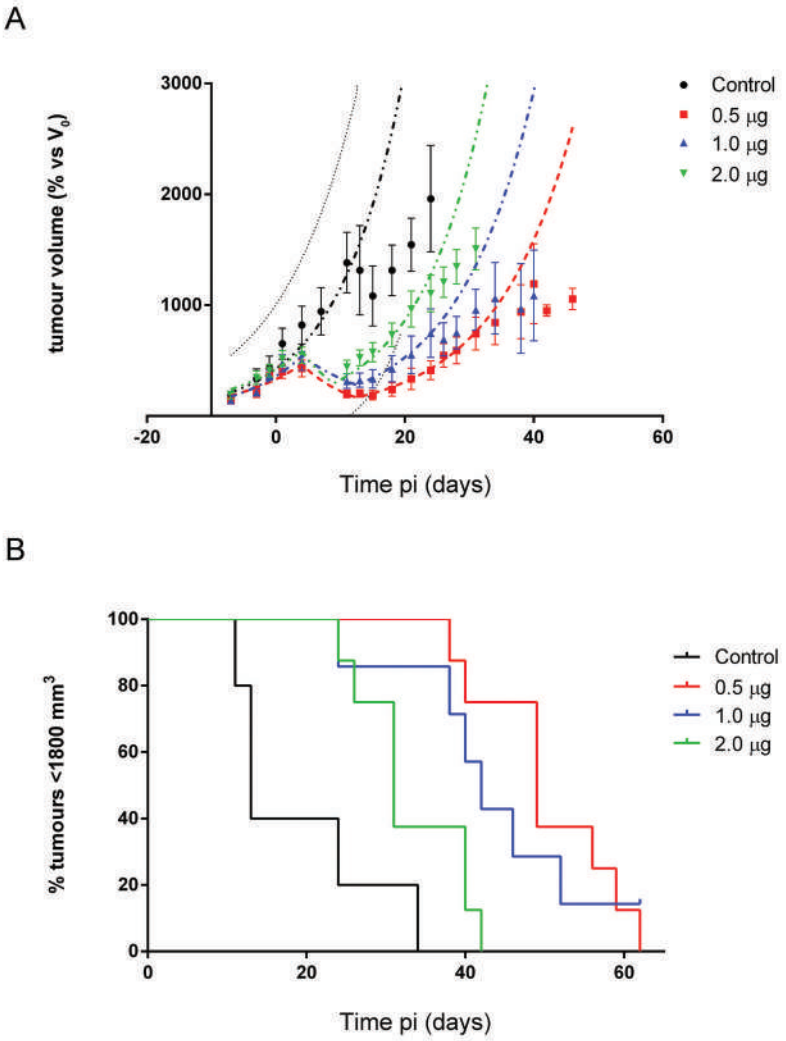

Figure 2. Tumour growth and survival curve after therapy using 30 MBq of ^{177}Lu labeled to 0.5, 1.0 or 2.0 µg TATE. A: Volume of H69 xenografts in mice after 30 MBq ^{177}Lu-TATE at 0.5 (red), 1.0 (blue) and 2.0 (green) µg. Regrowth occurred with doubling time T_d=9±3 days (n=8). The volume nadir for all groups was: 13±2 d. The control group growth (n=5) (black) with a T_d of 9±2 d. Dots represent the measured values, dashed line represents the fitting (see text for details), dotted line represents the 95% confidence interval for the control group; B: The time to reach the median maximum volume of 1800 mm^3 was 49 (38-62) d with 0.5 µg (red), 42 (24-65) d with 1.0 µg (blue) and 31 (24-42) d with 2.0 µg (green). Between the 0.5 and the 2.0 µg group there was a significant difference (p=0.002). pi: post injection

Effect of treatment scheme

Split-dose

Tumours in the control group showed exponential growth, with an average T_d of 6.4±2.1 d. These results were reflected in the median survival time: 17 d (range: 11-35) for the control group, 41 d (range: 25-71) for the 1x26 MBq group and 37 d (range: 27-50) for the 2x13 MBq group; the latter was not significantly different (p=0.56)(Figure 3A). Both treatment groups showed a significantly longer time to reach a tumour volume of 1800 mm^3 compared to the control group (p=0.001 for both groups) (Figure 3B). The group treated with 1x26 MBq/0.7 µg ^{177}Lu-TATE, showed a tumour volume nadir at 14±2 d after which regrowth occurred with an average T_d of 6 d (range: 2.8-10). In the 2x13 MBq/0.35 µg ^{177}Lu-TATE group the volume nadir was at 15±3 d. Regrowth occurred with a T_d of 6 d (range: 2.4-30). Further information on growth parameters after administration of the split-dose of ^{177}Lu-TATE are summarized in Table 2S in SI.

Double-dose

When comparing the two experimental groups, the 2x30 MBq ^{177}Lu-TATE group showed a significantly longer time to reach 1800mm^3 (p=0.04) compared to the1x30 MBq group. Median survival time was 32 d (range: 25-47) for the controls, 53 d (range: 47-75) for 1x30 MBq, and 75 d (range: 46-95) for 2x30 MBq (Figure 4A).Both the 1x30 MBq and 2x30 MBq/0,825 µg ^{177}Lu-TATE groups showed a significantly longer time to reach the tumour volume of 1800 mm^3, in comparison with the control group (p=0.008 and p= 0.002, respectively) (Figure 4B). Further information on growth parameters after administration of the double-dose of ^{177}Lu-TATE are summarized in Table 2S and 3S in SI.

Dosimetry

No difference was found in radioactivity measured in the tumour after the second administration of 30 MBq, using SPECT/CT after 24 h pi, at 1.79±0.21 kBq/mm^3 (Figure 5). This is a factor 1.14 above the 24 h value extrapolated from the biodistribution data. Correcting with this factor 1.14 results in an absorbed dose of 12.3 Gy for the group treated with one dose, whilst the double-dose corresponds to an absorbed dose of 25 Gy.

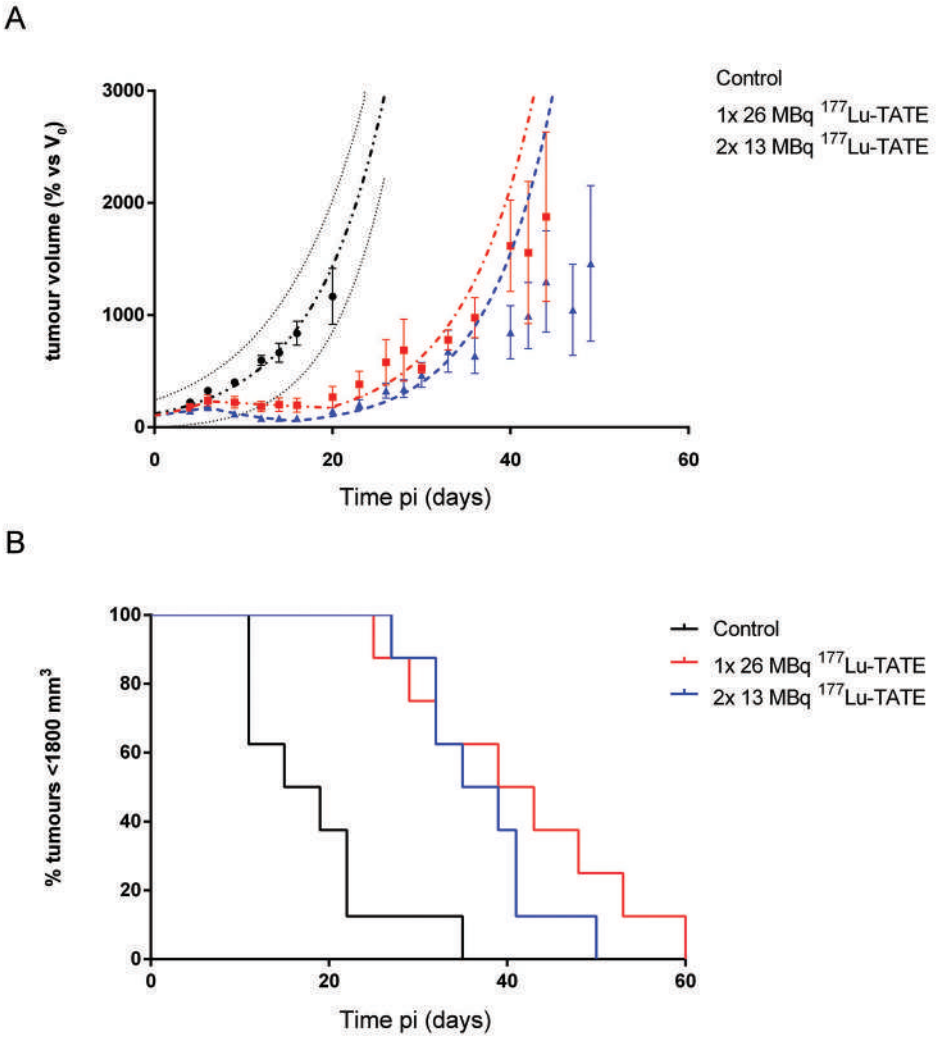

Figure 3. Tumour growth and survival curve after the therapy using 26 MBq (single-dose) or 2x13 MBq (split-dose) of ^{177}Lu-TATE. A: Tumour volume of H69 xenografts treated with 26 MBq ^{177}Lu/0.7 µg TATE (red) given and 2x13 MBq (blue). After the single therapy 7 (of 8) (red) tumours showed median regrowth with a doubling time T_d of 6 days (range: 2.4-30 d), all starting regrowth after volume nadir at 14±2 d. All tumours showed regrowth with T_d=6 d (2.8-10 d; n=8) after the 2x13 MBq with a nadir in the tumour volume after: 15±3 d. The tumour volume in the control group (n=8) showed a mean doubling time of T_d=6.4±2.1 d; B: Median time for the tumour to reach a volume of 1800 mm^3 in control group (black), single-dose (red) and split-dose (blue). The values of the median were 17, 37 and 41 d respectively. D_0: day 0; pi: post injection.

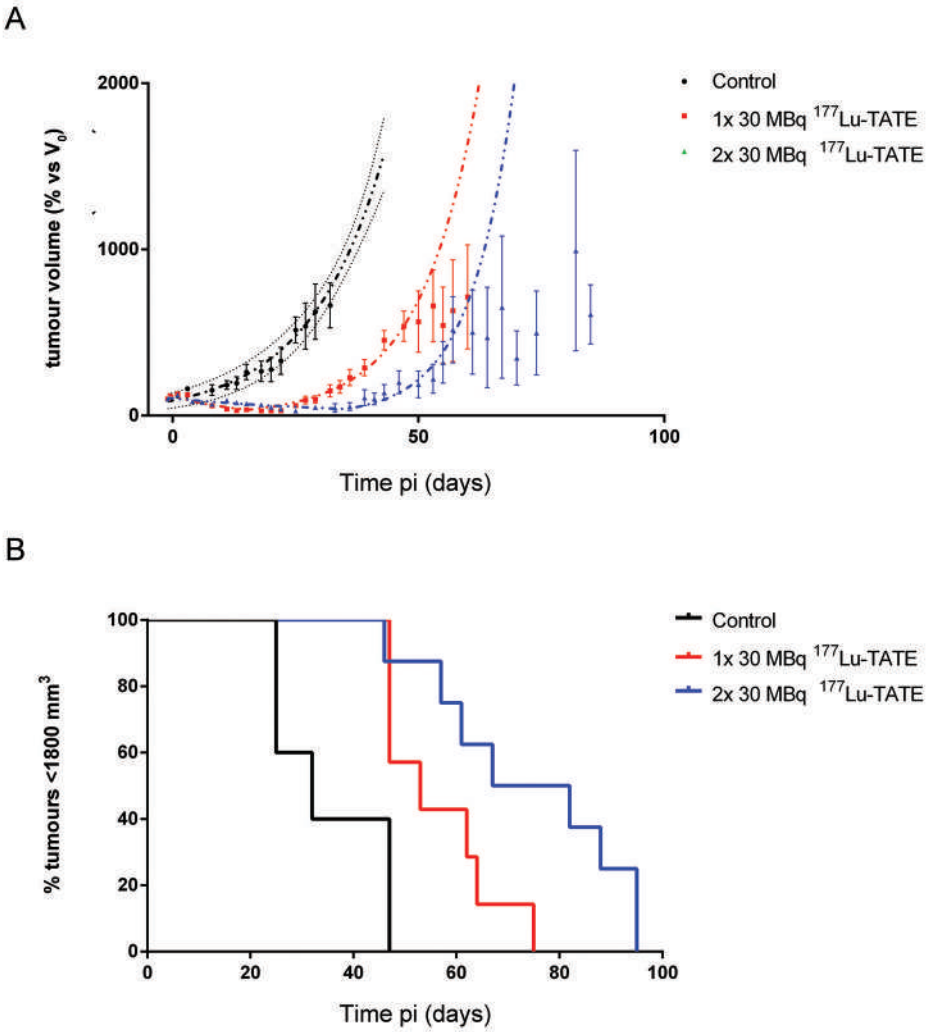

Figure 4. Tumor growth and survival curve after therapy using single- or double-dose of 30 MBq ^{177}Lu-TATE. A: Tumour volume of H69-tumours (n=8) treated with 30 MBq ^{177}Lu/0.825 µg TATE (100 MBq/2.75 µg)(red) or 2x30 MBq ^{177}Lu/0.825 µg TATE with 14 days (d) interval (blue). Volume is expressed as % of the tumor volume at day 0 (D_0). All tumours after 1x30 MBq showed regrowth with T_d = 9.4±2.5 d, after the volume nadir at 15 d (11-20). After two doses, the T_d was 7.5±2 d, with a nadir of 33 d (14-59). In the control group (black) tumours growth with a doubling time of 11.6±3 d; B: Median time to achieve a tumour volume of 1800 mm^3 was respectively 32, 53 and 74 d. pi: post injection.

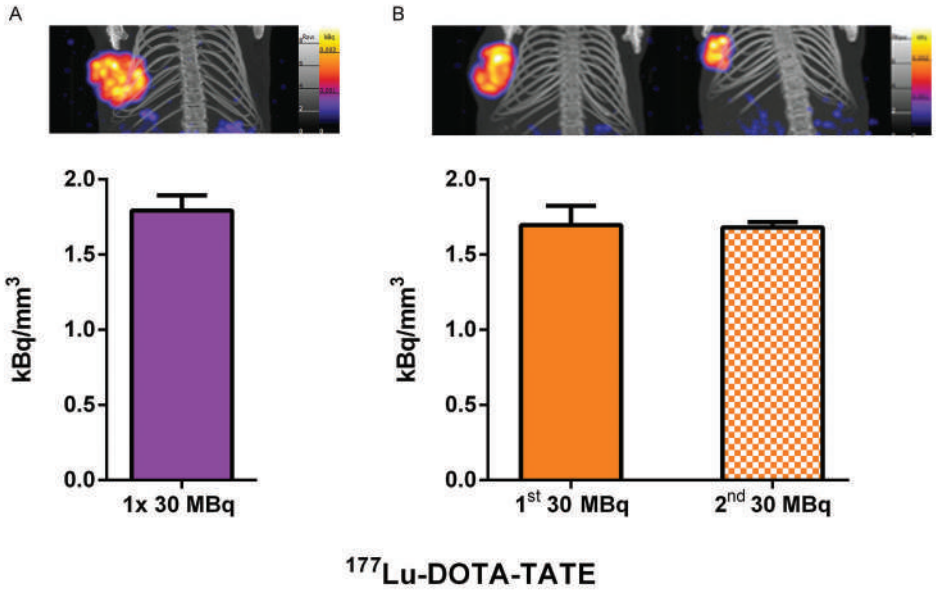

Figure 5. Uptake of activity after each dose in mice 24 h after administration of 30 MBq of ^{177}Lu-TATE. A: On top: SPECT/CT image 24 h pi of a mouse treated with a single administration of 30 MBq of ^{177}Lu-TATE; below concentration of radioactivity measured in the tumor 24 h pi (purple bar); B: On top: SPECT/CT image 24 h pi of a mouse treated with two administrations of 30 MBq of ^{177}Lu-TATE with 14 d in between; Below: concentration of radioactivity measured in the tumor 24 h pi (orange bar) and 14 d +24 h (spotted orange bar). After the first administration, as well as after the second, tumour uptake in mice treated with two doses was comparable with the uptake in mice treated with one dose.

Comparison of response predicted by the LQM and average tumour volume

The average tumour volumes respond as a function of time following the LQM prediction (See equations in SI) with a mean α=0.14±0.03 Gy^{-1} (β=0 Gy^{-2}) in all cases, under the assumption that all tumour cells respond to the radiation exposure (Figure 6). Fit parameters of LQM are represented by the propagation factor (q), the median clearance time ($T_{clearance}$) and the linear component to the growth curve in the linear quadratic model (α). The values of the fit parameters of the predicted response curve are shown in Table 4S in SI. Clearance of non-dividing cells from the tumour volume proceeded with a median $T_{clearance}$=3.5 d (range: 0.9-7.1). The cells that keep on proliferating without response to the absorbed dose is q=5.5±2.4%, except for 2.0 µg (30 MBq) and 30 MBq in double-dose experiment (See Table S4 in SI). The radiation sensitivity was set at α=0.21 Gy^{-1}. The 2 µg group could be fitted by q=22% and the 30 MBq group in the double-dose expetiment by q=19%. Clearance of

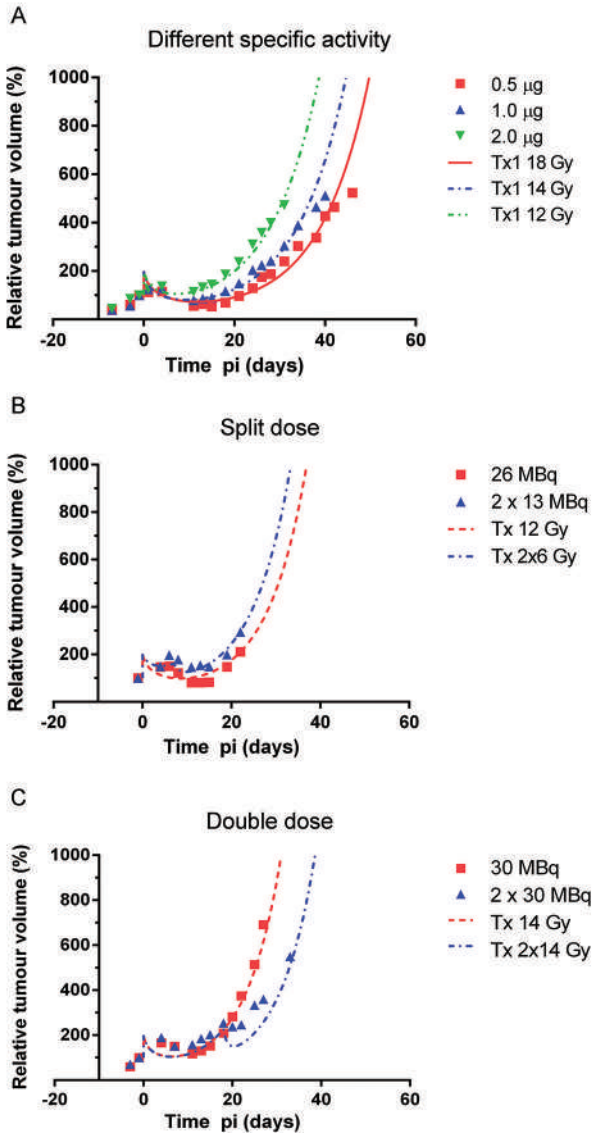

Figure 6. Comparison of response predicted by the linear quadratic model (LQM) and responses measured in the different evaluations. A: The tumor growth after the treatment 30 MBq of ^{177}Lu labeled to different amount of peptides: 0.5 µg (red) the 1.0 µg (blue) and the 2.0 µg groups (green) are compared; B: The response to 1x 26 MBq (red) is compared with response to 2x 13 MBq (blue); C: Response as predicted by the LQM with the average tumour volume measured for the mice treated with 1x (red) or 2x (blue) 30 MBq ^{177}Lu-TATE. The LQM fit was performed by either using the radiation sensitivity α as free parameter (uniform cell response) or by using the percentage of non-responding cells p as free parameter with α=0.21 Gy^{-1} (uniform radiation sensitivity). Response as predicted by the LQM is given as a line whilst the response as measured during the experiments is given as dots. Tx: therapy with the dose mention after; pi: post injection.

non-dividing cells from the tumour volume proceeded in this case with a median $T_{clearance}$=5.5 d (range: 1.5-9.0). The double-dose group (2´30 MBq) showed no delay in clearance from the tumour.

DISCUSSION

In this study, we investigated the relation between the absorbed dose in tumours response. At 48 h pi, for the 0.5 μg, the 1.0 μg as well as for the 2.0 μg group, there was an underestimation of tumour concentration of activity when comparing the SPECT results with the results from the biodistribution. A possible explanation for this underestimation could be a user dependent threshold setting for the 3D quantification.

As human NETs are slowly proliferating tumours (with a proliferation factor (Ki-67)< 3% for grade 1) (*13*), the relatively fast proliferating H69 tumour model, with a Ki-67 of 70-90% (*14*), has some limitations as a general model for NETs. Keeping this in mind, the two-weeks interval we applied in the double-dose experiment, might be comparable with the 6-8 weeks interval that is being applied in clinical PRRT for NET patients (*15*).

In earlier preclinical studies receptor saturation has been shown to be a limiting factor for tumour uptake of radiopeptides (*16*). In a CA20948 rat model, Müller et al. (*17*) also showed that a diagnostic dose of ^{177}Lu-TATE (3 MBq/0.5 μg peptide) resulted in a relatively high accumulation of radioactivity in SSTR2-positive tissues compared with a therapeutic peptide amount (300 or 555 MBq/15 μg). This suggests that therapeutic amounts are in the concentration range which saturates SSTR2 in the tumour. In patients the tumour capacity of SSTR2 seems not to be reached Kratochwil et al. (*18*) however reported receptor saturation of liver tumours when radiolabelled peptides were intra-arterially administered via the hepatic artery. The physiologically based pharmacokinetic model for radiolabelled octreotide studied by Kletting and collaborators (*7*), showed that also in clinical setting receptor saturation may cause reduced uptake in well perfused tumours (*7, 19*).

Since the majority of PRRT patients suffer from metastases, in most cases the evaluation of the therapy is focused mainly on the larger tumour masses with relative high uptake of radionuclides. However, this information may not apply to the uptake in the smaller metastases which could be less perfused or suffer from SSTR saturation.

In the second part of our investigation, we first adjusted the treatment scheme by administering the treatment in two half doses (in the split-dose experiment) and second a double-dose (in the double-dose experiment) twice the activity was given with 14 days interval.

The results we obtained in the split-dose experiment, demonstrated that this variation had no influence on the anti-tumour response. This means that for clinical application the same therapeutic effect may be obtained but with reduction of the risk on toxicity to healthy tissue by the principles of the LQM, assuming that the α/β value for tumours is larger than for normal tissue.

Despite the assumed improvement of tumour perfusion after radiolabelled peptide treatment, as reported earlier (*20*), in the double-dose experiment we observed that the tumour uptake of ^{177}Lu-TATE after the second dose did not increase.

The tumour volume as a function of time can be described by using the LQM to translate the absorbed dose rate in the tumour into the number of killed cells, leading to volume reduction. The derived LQM parameters for H69 differ hugely from those reported in literature for cell survival. We found α=0.14±0.03 Gy^{-1} without any indication for a quadratic dose response (β=0), much lower than the previous reported α of 0.21±0.16 Gy^{-1} and β=0.06±0.05 /Gy^{-2} for H69 tumours (*21*), although the difference is not significant. The diminished quadratic response could also be explained by a low sub-lethal damage repair half-life (T_{rep}); the quadratic part of the LQM (equation 4 in SI) diminishes when T_{rep} is below 6 h. Splitting the delivery of an absorbed dose, following our results, will have no influence on the tumour cell kill according to the LQM. Further experiments should consider whether the other asset of the LQM, reduction of late-occurring toxicity, also holds for ^{177}Lu-TATE. An individually optimized treatment scheme together with an individually optimized specific activity, should result in an increased absorbed dose by the tumour and optimal PRRT. For pancreatic NETs, this increased absorbed tumour dose has been related to an increased response (*15*). The results from our studies and the use of the LQM offer possibilities for further improved individualized treatment. Tumour biopsies can be used to determine its radiosensitivity, helping to predict what response a certain dose of activity will render. Furthermore, the determination of tumour radiosensitivity can indicate if dose fractionation does affect tumour response for each patient. Breeman al. (*22*) have shown that it is possible to label ^{177}Lu-TATE at a higher specific activity than the currently used 37 MBq/µg.

Treatments given at the maximal tolerated dose (for the kidneys and bone marrow), like in some institutes is performed (*23, 24*) , remains to form a matter of debate. Considering overall survival, there is some evidence that therapy at a maximal tolerated dose leads to a higher success rate in e.g. tumour lesion ablation. Tumour recurrence often is the result of just some (clusters of) untreated cells not yet visible with imaging methods or not expressing the targeting vector's receptor. Treatment with β^-radiating radionuclides is not optimal to kill

individual cells or small clusters below 1.2 mm diameter (*25*). Therefore, a more prudent approach is advisable to stay below the full tolerable maximum, and thereby keeping treatment options behind for a potential recurrence. Most importantly personalized dosimetry should be the guidance in these treatment planning approaches.

CONCLUSION

The absorbed dose and the linear quadratic model can be used to predict anti-tumour response and optimize specific activity for each individual patient. Furthermore, splitting of the dose, did not affect anti-tumour response indicating a negligible quadratic dose response parameter. Our current findings validate the use of an individualized specific activity and treatment scheme based on patient and tumour specific characteristics in dosimetry and radiobiology. Prospective treatment planning for radionuclide therapies is feasible when all relevant tumour radiobiology parameters are known, like the radiation sensitivity α/β and the sub-lethal damage repair half-life.

REFERENCES

1. Bodei L, Kidd M, Paganelli G, et al. Long-term tolerability of PRRT in 807 patients with neuroendocrine tumours: the value and limitations of clinical factors. Eur J Nucl Med Mol Imaging. 2015;42:5-19.
2. Strosberg J, El-Haddad G, Wolin E, et al. Phase 3 Trial of 177Lu-Dotatate for Midgut Neuroendocrine Tumors. N Engl J Med. 2017;376:125-135.
3. Sowa-Staszczak A, Pach D, Chrzan R, et al. Peptide receptor radionuclide therapy as a potential tool for neoadjuvant therapy in patients with inoperable neuroendocrine tumours (NETs). Eur J Nucl Med Mol Imaging. 2011;38:1669-1674.
4. van Essen M, Krenning EP, Kam BL, de Herder WW, Feelders RA, Kwekkeboom DJ. Salvage therapy with (177)Lu-octreotate in patients with bronchial and gastroenteropancreatic neuroendocrine tumors. J Nucl Med. 2010;51:383-390.
5. Sandstrom M, Garske-Roman U, Granberg D, et al. Individualized dosimetry of kidney and bone marrow in patients undergoing 177Lu-DOTA-octreotate treatment. J Nucl Med. 2013;54:33-41.
6. de Jong M, Breeman WA, Bernard BF, et al. Tumour uptake of the radiolabelled somatostatin analogue [DOTA0, TYR3]octreotide is dependent on the peptide amount. Eur J Nucl Med. 1999;26:693-698.
7. Kletting P, Schuchardt C, Kulkarni HR, et al. Investigating the Effect of Ligand Amount and Injected Therapeutic Activity: A Simulation Study for 177Lu-Labeled PSMA-Targeting Peptides. PLoS One. 2016;11:e0162303.
8. Joiner M, van der Kogel A. Basic Clinical Radiobiology Fourth Edition: Hodder Education; 2009.
9. Barone R, Borson-Chazot F, Valkema R, et al. Patient-specific dosimetry in predicting renal toxicity with (90)Y-DOTATOC: relevance of kidney volume and dose rate in finding a dose-effect relationship. J Nucl Med. 2005;46 Suppl 1:99S-106S.
10. Breeman WA, Kwekkeboom DJ, de Blois E, de Jong M, Visser TJ, Krenning EP. Radiolabelled regulatory peptides for imaging and therapy. Anticancer Agents Med Chem. 2007;7:345-357.
11. Melis M, Forrer F, Capello A, et al. Up-regulation of somatostatin receptor density on rat CA20948 tumors escaped from low dose [177Lu-DOTA0,Tyr3]octreotate therapy. Q J Nucl Med Mol Imaging. 2007;51:324-333.
12. Bolch WE, Eckerman KF, Sgouros G, Thomas SR. MIRD pamphlet No. 21: a generalized schema for radiopharmaceutical dosimetry--standardization of nomenclature. J Nucl Med. 2009;50:477-484.
13. Strosberg JR, Nasir A, Hodul P, Kvols L. Biology and treatment of metastatic gastrointestinal neuroendocrine tumors. Gastrointest Cancer Res. 2008;2:113-125.
14. Erlandsson A, Forssell-Aronsson E, Seidal T, Bernhardt P. Binding of TS1, an anti-keratin 8 antibody, in small-cell lung cancer after 177Lu-DOTA-Tyr3-octreotate treatment: a histological study in xenografted mice. EJNMMI Res. 2011;1:19.
15. Ilan E, Sandstrom M, Wassberg C, et al. Dose response of pancreatic neuroendocrine tumors treated with peptide receptor radionuclide therapy using 177Lu-DOTATATE. J Nucl Med. 2015;56:177-182.
16. Kolby L, Bernhardt P, Johanson V, et al. Successful receptor-mediated radiation therapy of xenografted human midgut carcinoid tumour. Br J Cancer. 2005;93:1144-1151.

17. Muller C, Forrer F, Bernard BF, et al. Diagnostic versus therapeutic doses of [(177)Lu-DOTA-Tyr(3)]-octreotate: uptake and dosimetry in somatostatin receptor-positive tumors and normal organs. Cancer Biother Radiopharm. 2007;22:151-159.
18. Kratochwil C, Giesel FL, Lopez-Benitez R, et al. Intraindividual comparison of selective arterial versus venous 68Ga-DOTATOC PET/CT in patients with gastroenteropancreatic neuroendocrine tumors. Clin Cancer Res. 2010;16:2899-2905.
19. Kletting P, Muller B, Erentok B, et al. Differences in predicted and actually absorbed doses in peptide receptor radionuclide therapy. Med Phys. 2012;39:5708-5717.
20. Haeck J, Bol K, Bison S, et al. Optimized time-resolved imaging of contrast kinetics (TRICKS) in dynamic contrast-enhanced MRI after peptide receptor radionuclide therapy in small animal tumor models. Contrast Media Mol Imaging. 2015;10:413-420.
21. Shui C, Khan WB, Leigh BR, Turner AM, Wilder RB, Knox SJ. Effects of stem cell factor on the growth and radiation survival of tumor cells. Cancer Res. 1995;55:3431-3437.
22. Breeman WA, Chan HS, de Zanger RM, Konijnenberg MK, de Blois E. Overview of Development and Formulation of (1)(7)(7)Lu-DOTA-TATE for PRRT. Curr Radiopharm. 2016;9:8-18.
23. Sundlov A, Sjogreen-Gleisner K, Svensson J, et al. Individualised 177Lu-DOTATATE treatment of neuroendocrine tumours based on kidney dosimetry. Eur J Nucl Med Mol Imaging. 2017.
24. Verburg FA, Lassmann M, Mäder U, Luster M, Reiners C, Hänscheid H. The absorbed dose to the blood is a better predictor of ablation success than the administered 131I activity in thyroid cancer patients. European Journal of Nuclear Medicine and Molecular Imaging. 2011;38:673-680.
25. O'Donoghue JA, Bardies M, Wheldon TE. Relationships between tumor size and curability for uniformly targeted therapy with beta-emitting radionuclides. J Nucl Med. 1995;36:1902-1909.

SUPPLEMENTARY INFORMATION

Animals and tumour model

Male NMRI Nu/nu mice were obtained from Harlan (Heerlen, the Netherlands). One week after arrival, mice were inoculated subcutaneously with 10^7 H69 cells in a suspension of 1:2 v/v Seligmann's buffered salt solution (SBSS) and Matrigel (BD Biosciences, Mississauga, Canada) while anesthetized with a mixture of isoflurane/O_2: 2.0% at 0.5 mL/min. For all experiments, animals were randomized into matching treatment groups with regard to tumour size. Three times a week mice were weighed and tumour size was measured using a calliper ruler by a person blinded for the treatment groups. Body weight of the mice at start of treatment was between 28.1 and 35.6 g. Tumour volume was calculated using the formula: (length*width) ^1,5)* π/6 (*1*). Tumours were allowed to develop until a maximum of 1800 mm^3. Mice also were euthanized after >10% loss of body weight since start of the experiment or in case of other serious discomfort. Administration of saline and ^{177}Lu-TATE was performed intravenously via the tail vain.

SPECT/CT imaging

SPECT/CT images were performed with the four-headed NanoSPECT/CT system (BioScan, Washington DC, USA). Multi pinhole mice collimators with 9 pinholes (diameter 1.4 mm) per head were used: 24 projections, 120 sec per projection were applied. The scans were obtained with a quality factor of 0.7. SPECT scans were reconstructed iteratively on a 256x256 matrix, using HiSPECT NG software (Scivis, GmbH Göttingen, DE) and ordered subset expectation maximization (OSEM). The total amount of radioactivity in the tumour was quantified on SPECT/CT images by tri-dimensional (3D) quantification using InVivoScope software (IVS, Bioscan, Washington DC, USA). To achieve accurate quantification, the camera was calibrated by scanning a 20 mL polypropylene tube phantom filled with a known amount of ^{177}Lu activity. Before each SPECT acquisition, a CT scan was performed for anatomical reference. The scan was performed using 240 projections with a standard resolution. Tube voltage was 45 kVp and exposure time was 500 ms. During scanning, the mice were anesthetized with a mixture of isoflurane/O_2: 2.0% at 0.5 mL/min. and body temperature was maintained using a heated bed.

Experimental Settings

Effect of specific activity on tumour growth and dosimetry of the tumour and normal organs (Table 1, Experiment 1)

Three experimental groups of H69 tumour bearing mice (n=8 per group) were treated with 30 MBq ^{177}Lu-TATE, labelled to either 0.5, 1.0 or 2.0 μg of peptide, which was diluted in 0.2 mL saline. A control group of H69 tumour bearing mice (n=5) received 0.2 mL saline. To study the kinetics of radioactivity uptake and retention by the tumour, SPECT/CT scans were acquired at 4 h, 2 and 4 days (d) post injection (pi). Monitoring of body weight and tumour size were performed three times a week for 65 d.

For biodistribution studies, three additional groups of H69 tumour bearing mice (n=12 per group) also received 30 MBq ^{177}Lu-TATE, labelled to 0.5, 1.0 or 2.0 μg peptide. At 2, 4 and 7 d pi four mice per group were sacrificed, tumours and selected organs were harvested and weighed and the amount of retained radioactivity was counted using a gamma counter (Wallac, 1480 Wizard 3", Perkin Elmer, Groningen). Tissue uptake of ^{177}Lu-TATE was calculated as % injected activity per gram of tissue (% IA/g).

Evaluation of variations in treatment schedules

To study the effect of a split-dose compared with the full dose administered at once, two groups of H69 tumour-bearing mice (n=8 per group) (Table 1, Split-dose experiment) were treated with a total amount of 26 MBq/0.7 μg ^{177}Lu-TATE in 0.2 mL saline, either in one single-dose of 26 MBq (single-dose group) or as two doses of 13 MBq with 5 d interval (split-dose group). A control group (n=8) received 0.2 mL of saline. Monitoring of body weight and tumour size was performed three times a week for 100 days, or until tumours reached a volume >1800 mm^3.

To study the effect of an additional treatment on tumour response and absorbed dose in critical organs, we performed further analysis on specific data from an earlier study (Table 1, Double-dose experiment) (*1*), in which two groups of H69 tumour-bearing mice (n=8 per group) were treated either with a single-dose of 30 MBq/0.825 μg ^{177}Lu-TATE in 0.2 mL saline or double the dose, in two cycles with a 14 d interval. A control group (n=5) received 0.2 mL of saline. Monitoring of body weight and tumour size were performed three times a week for 100 d, or until tumours reached a volume >1800 mm^3.

Dosimetry calculation

Dosimetry in normal organs and tumours was performed according to the Medical Internal Radiation Dose (MIRD)-scheme (*2*):

$$D(organ) = \sum_i \int_0^\infty \frac{A_i}{m_i}(t) e^{-\lambda t} dt \times m_i \times S(organ \leftarrow organ_i) \quad (1)$$

with λ the decay constant for ^{177}Lu: λ =0.00434/h. The time-specific activity curves $A_i/m_i(t)$ were obtained by fitting the biodistribution data (specific radioactivity uptake in the organs) with a single exponential curve. The time-activity curve for the tumour was based on the combination of biodistribution and SPECT data. The SPECT-based activity measurement at 4 hours was normalized by the biodistribution / SPECT ratio of the activities at 48 h. The resulting 4 tumour data were fitted with a 3-parameter exponential curve including a residual plateau. The Aikake Information Criterion was used to decide between a 2-parameter and a 3-parameter exponential fit. This curve was used for determining the time-integrated activity concentration, otherwise (if R^2 <0.7) the integral was performed by the trapezoidal method, assuming zero specific activity at 360 h. Absorbed doses (in Gy) to normal organs per administered activity were calculated with the S-values for a 25 g mouse phantom (*3*). Also, the reference organ masses in this model were used, thereby making the dose calculation independent of the actual organ mass. The absorbed dose to the tumour was calculated for a 200 mg sphere with the S-values for spherical nodes from OLINDA/EXM (*4*), the S-value of 0.114 mGy/MBq was obtained by linear interpolation, only the self-dose by the radioactivity in the tumour was calculated.

To calculate the absorbed dose in the third experiment, the original 1.0 μg dose value was multiplied with the ratio of the result of the SPECT quantification after 24 h and the 24 h time point of the fitted activity curve for the 1.0 μg biodistribution data.

Tumour growth curve fitting

The tumour growth curves V(t) were modelled with exponential growth functions from the normal growth equation. The data were further extrapolated beyond the censoring end-times to calculate a common growth curve.

$$V(t) = V(0) \times exp(kt), \text{ with } k = \ln(2)/T_d \quad (2)$$

being T_d the tumour volume doubling time. The fitted growth patterns were extrapolated beyond the censoring end-times to calculate a common growth curve. The treatment groups were modelled with exponential growth functions for both the initial growth the therapy effect and the regrowth by:

$$V(t) = V(0) \times exp(-k_1 t + k_2 \max_0(t - T_1)) \quad (3)$$

with k_1 the rate of tumour shrinkage and k_2 - k_1 the tumour growth rate setting in after the volume nadir time T_1. The time post injection needed to achieve the lowest tumour volume for each mouse is expressed as "nadir" for each treatment group (median and range).

Dose-response model for tumour volume

The LQM is used to predict the tumour volume as a function of time after start of the irradiation. The tumour volume is linked to the survival S of irradiated tumour cells. The LQM links the cell survival to the absorbed dose which builds up exponentially in radionuclide therapy with an effective decay constant l_{eff} of the radiopharmaceutical:

$$S = \exp\left(-\alpha D - \beta \frac{\lambda_{eff}}{\lambda_{rep} + \lambda_{eff}} D^2\right) \quad (4)$$

The repair of sub-lethal damage occurs during the dose delivery with time constant l_{rep}. The quadratic term expresses the combinatorial effect of unrepaired sub-lethal radiation damage and this effect is more prominent in normal tissue than in tumours (*5, 6*). Administering the absorbed dose in small fractions will therefore increase the survival more prominently in normal tissue than in tumours.

The tumour volume is represented by proliferating cells and dead or dying cells due to the irradiation. It is assumed that proliferation of alive cells will continue with the growth constant *k* and that dead cells will be cleared with clearance constant *m* (= $ln(2)/T_{clearance}$, where $T_{clearance}$ is median clearance time). The tumour volume as a function of irradiation time T after administration of the activity can then be expressed by (*7*);

$$V(T) = V(0) \times \left\{ S(T) \times \exp(kT) + \frac{\int_0^T (1 - S(t)) \times \exp(-m(T-t))dt}{\int_0^T (1 - S(t))dt} \right\} \quad (5)$$

with the survival $S(T) = \exp\left(-\alpha D(T) \times \left(1 - \frac{G(T)}{\alpha/\beta} \times D(T)\right)\right)$ and the absorbed

dose to the tumour: $D(T) = \int_0^T A(t) \times S(tumour \leftarrow tumour)dt$. The Lea-Catcheside factor G(T) expresses the probability for combinatorial damage caused by two or more repairable lesions as a function of time. In radiation therapy α is defined as linear component to the growth curve in the linear quadratic model and β as the quadratic part of the growth curve in the linear quadratic model. The α/β ratio is a theoretical measure of a tissue's predicted response to a dose rate. The α and β for H69 tumours were taken from literature α = 0.21 ± 0.16 /Gy and β = 0.06 ± 0.05 /Gy^2 (α/β = 3.01 ± 3.42 Gy)(*8*). As the time for repair (T_{rep}) is much lower than the effective time (T_{eff}), G(T) rapidly goes to 0 and the quadratic term of the LQM can be neglected. This simplifies V(T) considerably:

$$V(T) = V(0) \times \left\{ exp(-\alpha D(T)) \times \exp(kT) + \frac{\int_0^T \left(1 - \exp\left(-\alpha D(t)\right)\right) \times exp(-m(T-t))dt}{\int_0^T \left(1 - exp\left(-\alpha D(t)\right)\right)dt} \right\}, \quad (6)$$

for a single exponential dose rate with effective decay constant l_{eff}, this expression can be approximated by:

$$V(T) = V(0) \times \left\{ \begin{array}{c} exp\left(kT - \alpha\left[D_0\left(1 - \exp\left(-\lambda_{eff}T\right)\right]\right)\right) + \\ \frac{\int_0^T \left(1 - \exp\left(-\alpha\left[D_0\left(1 - \exp\left(-\lambda_{eff}t\right)\right]\right)\right) \times exp(-m(T-t))dt}{\int_0^T \left(1 - exp\left(-\alpha\left[D_0\left(1 - \exp\left(-\lambda_{eff}t\right)\right]\right)\right)dt} \end{array} \right\} \quad (7)$$

$$V(T) \approx V(0) \times \left\{ \begin{array}{c} exp\left(kT - \alpha\left[D_0\left(1 - \exp\left(-\lambda_{eff}T\right)\right]\right)\right) + \\ \frac{\frac{1 - \exp\left(-mT\right)}{m} - \frac{\exp\left(-\alpha D_0 \lambda_{eff} T\right) - \exp\left(-mT\right)}{m - \alpha D_0 \lambda_{eff}}}{T - \frac{1 - \exp\left(-\alpha D_0 \lambda_{eff} T\right)}{\alpha D_0 \lambda_{eff}}} \end{array} \right\} \quad (8)$$

The absorbed dose is assumed to be homogeneously distributed over the tumour volume and also the response of tumour cells to radiation does not allow any heterogeneity. Both heterogeneities are introduced in the volume dose response model by a propagation factor p. A fraction of the cells, representative for the propagation factor (*q*), are assumed to remain unresponsive to the radiation exposure and grow undisturbedly following equation 2, whereas the complementary fraction *1-q* will show a growth response following the LQM equation 8.

Statistics

Prism software version 5.0 (Graph Pad, La Jolla, California, USA) was used to analyse tumour growth and determine statistical significance between the treatment groups. One way ANOVA was used for statistical analysis of tumour uptake. Results are given as mean ± standard deviation (SD) when the SD is <40% and as median and range (min-max) for the survival curves or when the SD is >40%. Significant results were considered for p>0.05. A log-rank test was performed for comparison of the survival curves. Goodness of fits by the least-squares

method was judged by the Pearson R^2 method. The corrected Aikake Information Criterion was used to decide on the complexity of the fits. Growth delay was calculated as the difference in median time needed to reach a tumour volume >1800 mm^3 in the treated groups compared with this median time for the control group. This value was given with the range of the single tumours compared with the median time of the control group.

Kinetics of radioactivity of ^{177}Lu-TATE

The clearance kinetics of the radioactivity from the kidneys, pancreas and stomach were described by single-exponential curves (Figure S1), with half-lives of 38±8 h, 50±16 h and 59±16 h, respectively. The clearance half-lives were independent of the applied peptide amounts. To calculate the clearance kinetics of the H69-tumour SPECT/CT and tumour biodistribution data were combined. SPECT/CT quantitative imaging of the tumour uptake at 48 h (Figure 1B) resulted in 1.0±0.2% IA/g (0.5 μg), 0.9±0.2% IA/g (1 μg) and 0.68±0.04% IA/g (2 μg),

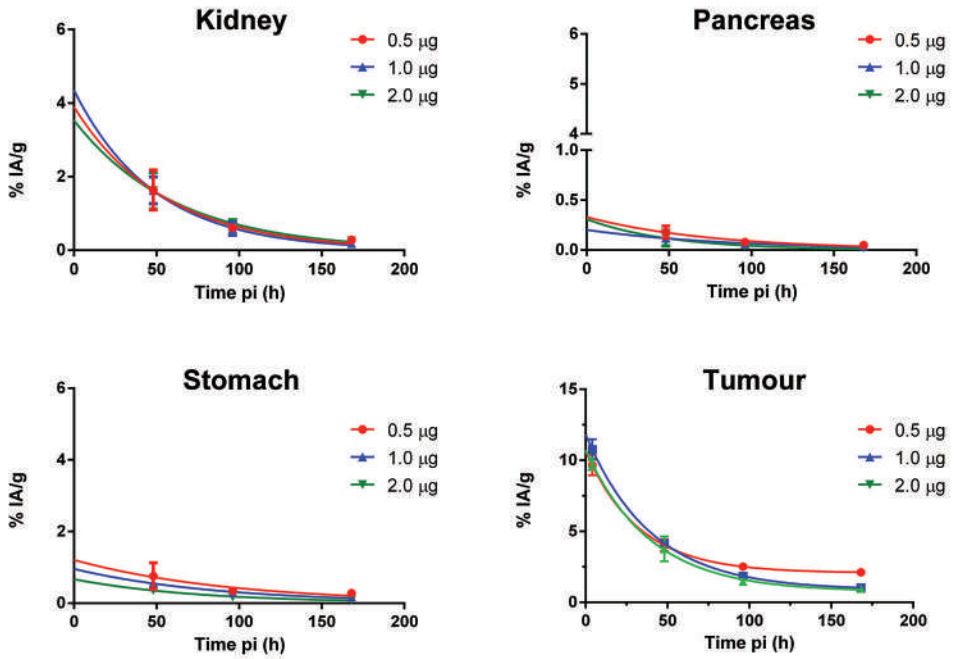

Figure S1. Radioactivity concentration as percentage injected activity per gram (%IA/g) over time in selected organs and tumor. Injected activity per group: 30 MBq of ^{177}Lu. Amount of injected octreotate: 0.5 μg (red line); 1.0 μg (blue line); 2.0 μg (green line). Tumour values are based on the combination of biodistribution and SPECT data. pi: post injection.

respectively a factor 3.9, 4.6 and 5.6 less than found in the biodistribution study. The SPECT/CT derived tumour uptake at 4 h pi was adjusted with these factors (Figure 3). The 0.5 μg study group showed a rapid initial tumour clearance with a half-life of 23±4 h, leading to a plateau uptake of 2.1±0.3% IA/g (20% of the projected initial uptake). The higher amount of peptides showed slower initial clearances of 28±4 h and 27±6 h, for 1 and 2 μg respectively, leading to a lower plateau value at only 7% of the projected initial uptake.

Tables

Table S1. Absorbed dose (in Gy) after administration of ^{177}Lu labeled to 0.5, 1.0 or 2.0 μg TATE

Absorbed dose, mean ± SD[Gy]/ peptide amount [μg]	Pancreas	Stomach	Kidneys	Tumour
0.5	0.5±0.1	1.6±0.5	4.2±1.0	17.8±2.5
1.0	0.4±0.1	1.2±0.3	4.3±1.2	14.1±3.9
2.0	0.3±0.2	0.8±0.2	4.2±1.3	9.6±4.1

Absorbed dose to normal organs and 200 mg of tumour per administered activity of 30 MBq was calculated with a 25 g mouse phantom. The dose to the tumour was calculated based on the combination of SPECT and biodistribution data.

Table S2. Growth parameters after treatment with 26 MBq of ^{177}Lu/0.7 μg TATE (Split-dose experiment)

Group	Median doubling time [days, range (min-max) or SD*]	Time to 10 x V_0 [days, range (min-max)]	Nadir [days, SD]	Growth delay [days, range (min-max)]
Control	6.4±2.1	21.1±6.9	-	-
1x26 MBq	6 (2.4-30)	37 (31-151)	14±2	24 (8-56)
2x13 MBq	6 (2.8-10)	39 (32-47)	15±3	20 (10-33)

Tumour characteristics after treatment with 26 MBq of ^{177}Lu-TATE administered at once or administered in two doses of 13 MBq with 5 days interval, compared with a control group. min: minimum; max: maximum; SD: standard deviation. *see the main text for details.

Table 3S. Tumour characteristics after treatment with one or two doses of 30 MBq ^{177}Lu/0.825 μg TATE (double-dose experiment)

Group	Doubling time [days, SD]	Time to 10 x V_0 [days, SD]	Nadir [days, range (min-max)]	Growth delay [days, range (min-max)]
Control	11.6±3.0	39±7		
30 MBq	9.4±2.5	59±13	15 (11-20)	21 (15-43)
2x30 MBq	7.5±2.0	73±17	33 (14-59)	42.5 (14-63)

Tumour characteristics after treatment with 30 MBq of ^{177}Lu-TATE administered at once or administered in two doses of 30 MBq with 14 days in between, compared with a control group. min: minimum; max: maximum

Table 4S. Fit parameters of the LQM predicted response curve (based on equation 8) and measured response of all performed experiments

		Uniform cell response (q=0)		Uniform cell sensitivity (a=0.21 Gy^{-1})	
Curves	fit R^2	a [Gy^{-1}]	$T_{clearance}$ [d]	q (%)	$T_{clearance}$ [d]
A: 0.5 mg	0.49	0.14	3.5	7%	6.3
A: 1.0 mg	0.37	0.14	7.1	9%	9.0
A: 2.0 mg	0.75	0.10	2.7	22%	4.0
B: 1 ´ 26 MBq	0.28	0.18	3.9	3%	4.6
B: 2 ´ 13 MBq	0.40	0.19	6.1	2%	8.1
C: 1 ´ 30 MBq	0.22	0.11	0.9	19%	1.5
C: 2 ´ 30 MBq	0.34	0.10	3.1	7%	¥

R^2 represents the quality of the fit. a represents the radio sensitivity of the tumour cells; p stands for the percentage of cells which do not respond to treatment but continue proliferating; a was calculated assuming a uniform cell response (q=0) and p values were calculated assuming a uniform cell sensitivity (a=0.21 Gy^{-1}). For both calculations, the median clearance halve life $T_{clearance}$, representing the removal of death cells from the tumour mass, is given. A, B, C refer to the panels in Figure 6 in the main text. q: propagation factor; a: linear component to the growth curve in the linear quadratic model; $T_{clearance}$: median clearance time.

REFERENCES

1. Haeck J, Bol K, Bison S, et al. Optimized time-resolved imaging of contrast kinetics (TRICKS) in dynamic contrast-enhanced MRI after peptide receptor radionuclide therapy in small animal tumor models. *Contrast Media Mol Imaging.* 2015;10:413-420.
2. Bolch WE, Eckerman KF, Sgouros G, Thomas SR. MIRD pamphlet No. 21: a generalized schema for radiopharmaceutical dosimetry--standardization of nomenclature. *J Nucl Med.* 2009;50:477-484.
3. Keenan MA, Stabin MG, Segars WP, Fernald MJ. RADAR Realistic Animal Model Series for Dose Assessment. *J Nucl Med.* 2010;51:471-476.
4. Stabin MG, Sparks RB, Crowe E. OLINDA/EXM: the Second-generation Personal Computer Software for Internal Dose Assessment in Nuclear Medicine. *J Nucl Med.* 2005;46:1023-1027.
5. Joiner M, van der Kogel A. *Basic Clinical Radiobiology Fourth Edition*: Hodder Education; 2009.
6. Konijnenberg MW, Breeman WAP, de Blois E, et al. Therapeutic application of CCK2R-targeting PP-F11: influence of particle range, activity and peptide amount. *EJNMMI Research.* 2014;4:47.
7. Watanabe Y, Dahlman EL, Leder KZ, Hui SK. A mathematical model of tumor growth and its response to single irradiation. *Theoretical Biology and Medical Modelling.* 2016;13:6.
8. Shui C, Khan WB, Leigh BR, Turner AM, Wilder RB, Knox SJ. Effects of stem cell factor on the growth and radiation survival of tumor cells. *Cancer Res.* 1995;55:3431-3437.

CHAPTER 3

NANOPARTICLES

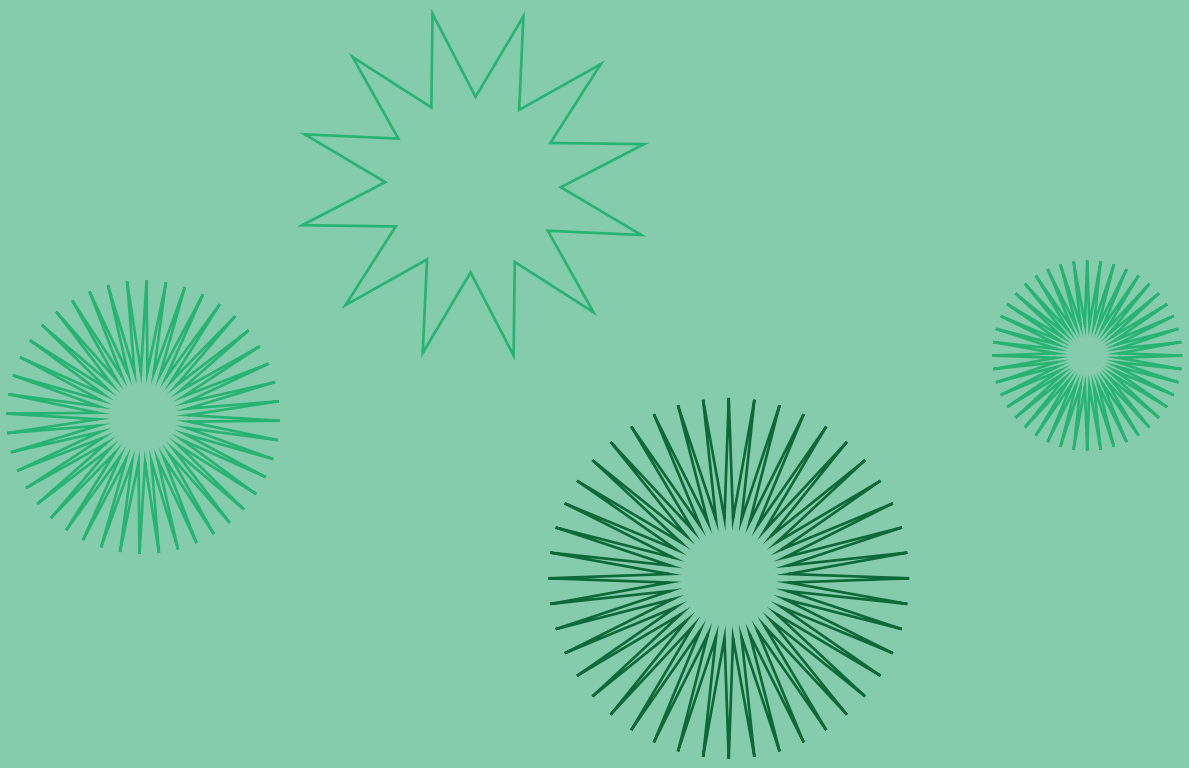

CHAPTER 3.1

Intravenous and intratumoral injection of Pluronic P94: the effect of administration route on biodistribution and tumor retention

Published in Nanotechnology, Biology and Medicine

Santini C, Arranja A, Denkova AG, Schosseler F, Morawska K, Dubruel P, Mendes E, de Jong M, Bernsen M

Nanomedicine: Nanotechnology, Biology and Medicine, doi:https://doi.org/10.1016/j.nano.2017.04.015

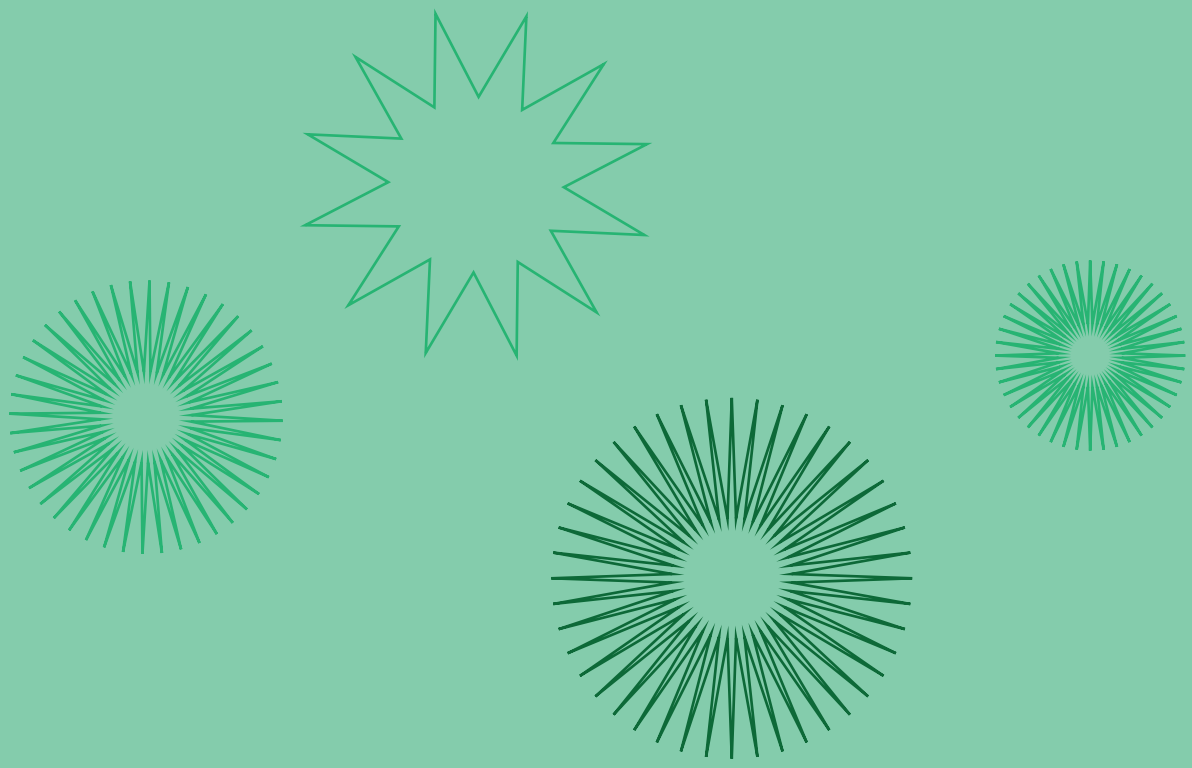

ABSTRACT

Pluronics P94 are block-copolymer showing prolonged circulation time and tumor-cell internalization in vitro, suggesting a potential for tumor accumulation and as a drug carrier. Here we report the results of the radiolabeled-P94 unimers (P94-^{111}In-DTPA) on tumor uptake/retention and biodistribution after intravenous and intratumoral administration to tumor-bearing mice. Intravenous administration results in a high radioactive signal in the liver; while in tumor and other healthy tissues only low levels of radioactivity could be measured. In contrast, the intratumoral injection of P94 resulted in elevated levels of radioactivity in the tumor and low levels in other organs, including the liver. Irrespective of the injection route, the tumor tissue presented long retention of radioactivity. The minimal involvement of off-target tissues following injection of P94, together with the excellent tracer retention over-time in the tumor designates Pluronic P94 copolymer as a highly promising carrier for anti-tumor drugs.

Keywords: Pluronics, unimers, intratumoral injection, intravenous injection, tumor retention

Abbreviations: P94: Pluronics P94; EPR: Enhanced Permeability and Retention; IV: intravenous; IT: intratumoral; DTPA: diethylenetriaminepentaacetic acid; PPO: poly(propylene oxide; PEO: poly(ethylene oxide); SPECT/CT: Single-Photon Emission Computed Tomography/Computed Tomography.

BACKGROUND

Safe, specific and more effective treatment is a well-recognized need in oncology and many efforts are being made towards the development of such therapeutic approaches. In this direction, the field of nanomedicine has grown considerably in the last decades. Many nano-sized particles showing great potential for the treatment of tumors are available for in vivo applications, including nanoparticles (liposomes, polymeric micelles) but also polymers. Among nanomedicines, structures based on Pluronics block copolymers have gained considerable interest due to their versatility, large availability, desirable biological properties and potential translation to the clinic (*1-3*). Some formulations of Pluronic are used in cosmetics, in pharmaceutical application and in clinics as a coadjutant for injections (*4, 5*).

Recently, it was shown that Pluronic P94 copolymers (P94) could be efficiently internalized by tumor cells in vitro and that exposure of tumor spheroids to P94 copolymer caused cellular disaggregation and size reduction of the spheroids (*6, 7*). Additionally, in vivo studies, performed with ^{111}In radiolabeled Pluronic copolymers in healthy mice, demonstrated high in vivo stability and long circulation time of P94 copolymer (detectable in the circulation up to 48 h post injection (pi)), with relatively limited liver and spleen accumulation and no evidence of acute toxicity (*8*). Altogether, these results suggest that P94 copolymers might be suitable for the delivery of therapeutic agents to cancers, and encourage further investigations of this compound.

When developing nanomedicines for the treatment of solid tumors, the capacity of the nanodevice to reach the tumor at high concentrations is a first requirement and has been proven challenging with various nanoparticles before (*9*).

Following IV administration, accumulation of nanoparticles in tumor tissue occurs via a phenomenon known as the Enhanced Permeability and Retention (EPR) effect (*10*). This effect results from the large fenestrations between endothelial cells from the newly-formed vessels and the lack of functional lymphatic vessels in and around the tumor (*11*). This specific combination of conditions in the tumor tissue, ensures and enhanced extravasation and specific retention of nanosized particles within the tumor mass (*10, 12-14*). The optimal size for EPR-effect-mediated extravasation was roughly estimated between 5 and 50 nm; extravasation substantially reduces above 200 nm, although a certain level of extravasation was observed for particles above 500 nm as well (*13, 14*).

Because of the nature of the EPR effect, nanoparticles that benefit from that phenomenon do not require molecular interactions with tumor receptors and the attachment of targeting agents is not needed. EPR effect therefore can be used to target lesions that do not (over)express tumor-specific targets. Despite the well-recognized value of the EPR effect,

the uptake of nanoparticles in tumors is rarely beyond the 10% ID/g (*15*), and in most cases between 1-5 % ID/g (*11*), often with limited tissue penetration (*16*).

Loco-regional administration of drugs is also commonly used approach in specific situation of clinical practice. Intratumoral (IT) administration overcomes most of the limitations of IV injections (being the poor accumulation in the tumor and the elevated retention in the off-target), improves the safety and the efficacy of treatment in localized solid tumors and is increasingly also being considered for nanoparticles (*17, 18*). The IT injection enhances the amount of an agent delivered to the tumor and, upon effective retention in the tissue, results in higher therapeutic doses at the lesion site. Additional benefit would result from reduction of the systemic spread via blood circulation, which, ultimately, leads to reduced exposure/accumulation of normal tissue to the therapeutic agent, and thus low(er) whole body toxicity.

To further assess the potential of P94 copolymer in cancer therapeutics we used the ability to functionalize P94 copolymer with the diethylenetriaminepentaacetic acid (DTPA) radiochelator, making it suitable for radiolabeling with ^{111}In. This radionuclide is broadly used in preclinical setting because of its favorable emission of gamma photons, suitable for SPECT imaging. Moreover ^{111}In has a physical half-life of ~68 h, which allows for long lasting follow up. The radiolabeling of P94 with ^{111}In allowed us to perform a detailed analysis of the biodistribution and tumor uptake characteristics of P94 copolymers in tumor bearing mice following systemic (IV) injection or loco-regional (IT) administration.

METHODS

Functionalization and radiolabeling of Pluronic P94 copolymer with DTPA chelator (P94-DTPA)

Pluronic P94 ($PEO_{26}PPO_{48}PEO_{26}$; Mn PEO blocks: 2200 Da; Mn PPO block: 2800 Da (*19*), where PEO is poly(ethylene oxide) and PPO is poly(propylene oxide)) was supplied by BASF and end-functionalized with the chelator DTPA and radiolabeled with ^{111}In following procedures described previously (*8, 20*) and further specified in Supplementary Materials (Supp) (Figure ure 1).

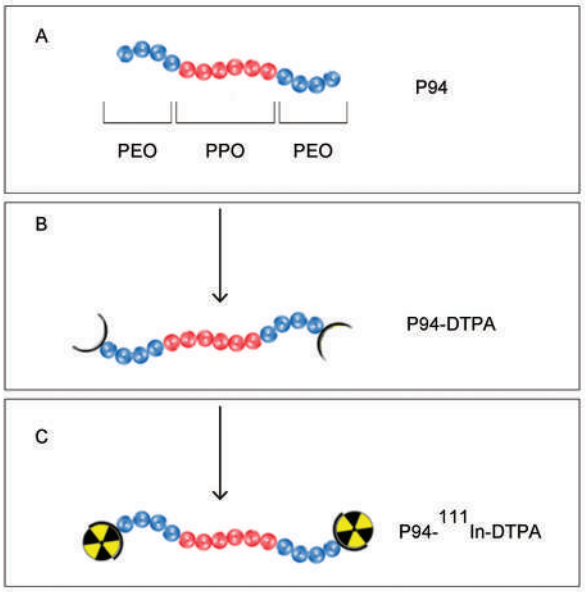

Figure 1. Diagram of the successive modifications of Pluronic P94 copolymer ($PEO_{26}PPO_{48}PEO_{26}$). A) Schematic representation of the plain P94 copolymer. PEO: hydrophilic part; PPO: hydrophobic part; B) Attachment of DTPA chelator (P94-DTPA); C) Radiolabeled P94-DTPA with ^{111}In (P94-^{111}In-DTPA). PEO: poly(ethyleneoxide); PPO: poly(propylene oxide); DTPA: diethylenetriaminepentaacetic acid.

In vivo tumor model

Human small cell lung cancer cells H69 (ECACC, Salisbury, UK (~3×10^6 cell/mouse) were inoculated subcutaneously in 20 young adult male Balb/c-nu mice (Janvier, France), $3x10^7$ cell/mL and 100 µL/mouse (see Supp for tumor model details). Tumor growth was monitored and measured with a caliper ruler three times per week. When the average tumor volume reached 300 mm^3, the mice were randomly subdivided in three groups: one experimental group (IV group) was subjected to intravenous injection of P94-^{111}In-DTPA (n=8); a second experimental group (IT group) was subjected to intratumoral injection P94-^{111}In-DTPA (n=8); the third group was used as control group and received an IT injection of ^{111}In-DTPA (n=4). All animal experiments were performed in accordance with Dutch animal welfare regulations and approved by the local ethics committee.

Experimental plan

IV experimental group. Mice from the IV injection group received an injection of ~200 μL (~0.2 mg and ~15 MBq/animal) of P94-^{111}In-DTPA in the tail vein. Six out of eight mice were randomly chosen to undergo imaging studies and subjected to a whole body Single-Photon Emission Computed Tomography/Computed Tomography (SPECT/CT) scans at different time points prior to biodistribution studies. The remaining two animals were subjected to biodistribution studies only (see Supp for SPECT/CT parameters). All mice selected for imaging studies (n=6) received a scan at 4 h, 24 h and 48 h pi. After the acquisitions at 48 h pi, three mice out of the six chosen for imaging studies and one out of the two excluded from the imaging studies, were randomly chosen and sacrificed for biodistribution evaluation at 48 h pi (n=4). The remaining three mice from the imaging group were subjected to one further SPECT/CT scan at 120 h pi. Biodistribution study at 120 h pi for the remaining mice of the IV group (n=4) was performed immediately after the last acquisition (Figure 2)(see Supp for biodistribution details).

IT experimental group. Mice from the IT group received ~100 μL (~0.1 mg and ~7.5 MBq/animal) of P94-^{111}In-DTPA in one single injection in the center of the tumor. Similarly as for IV studies, six out of eight mice were randomly chosen for imaging studies and two were used for biodistribution studies only. All mice selected for imaging studies (n=6) received a whole body CT scan and one focused SPECT scan in the region of the tumor at 0.5 h pi (see Supp for SPECT/CT parameters). Then, whole body SPECT/CT scans were performed at 24 and 48 h pi. After the acquisitions at 48 h pi, three mice out of the six chosen for imaging studies and one out of the two excluded from the imaging studies, were randomly chosen and sacrificed for biodistribution evaluation at 48 h pi (n=4). The remaining three mice from the imaging group were subjected to one further SPECT/CT scan at 72 h pi. Biodistribution study at 72 h pi was performed immediately after the last acquisition in the remaining mice of the IT group (n=4) (Figure 2) (see Supp for biodistribution details).

Control group. Mice of the IT control group were injected IT with 100 μL of ^{111}In-DTPA (200 pmol and ~3 MBq). The four mice of the control group were subjected to one focused SPECT scan in the region of the tumor at 0.5 h pi and a whole body CT scan. Whole body SPECT/CT was performed at 24 and 48 h pi (see paragraph 2.5 for SPECT and CT parameters). The whole group was sacrificed 48 h pi studies for biodistribution evaluation (Figure 2) (see Supp for biodistribution details).

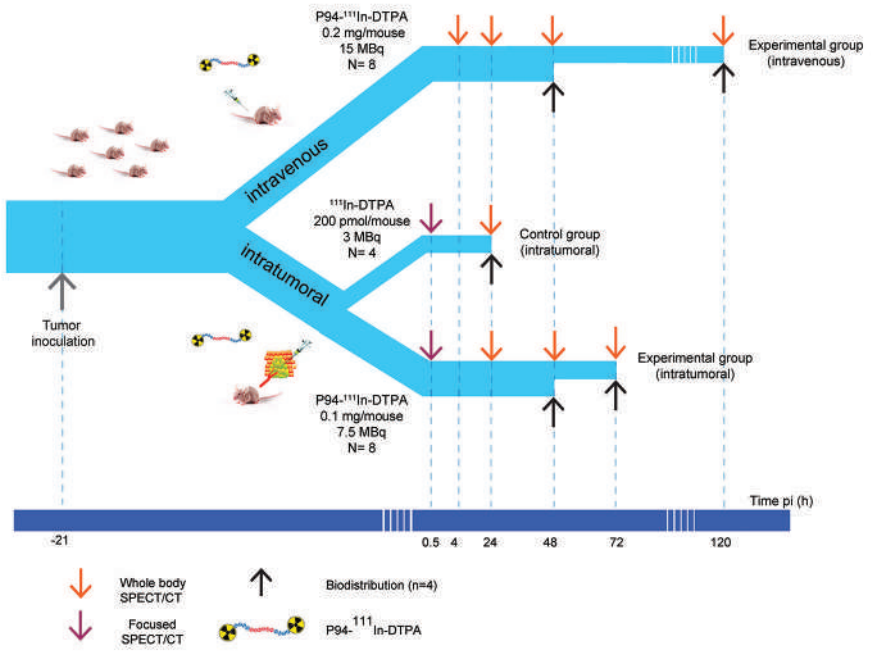

Figure 2. Temporal diagram of injection and scans of the Experimental groups (IV group and IT group) and control group.

Data analyses

All data were processed with Microsoft Excel 2010 and Prism version 5 (GraphPad Software, La Jolla, California, USA). To characterize the kinetics of P94-^{111}In-DTPA after IV and IT injection over-time, time-activity curves based on SPECT signal quantification were fitted with different curves: the one-phase-decay exponential curve was used for the data of tumors (IV and IT group) and the data from the IV injection; the linear regression was used for other IT results (see Supp for more details)

Biodistribution data were used to evaluate the difference in retention of P94-^{111}In-DTPA between the last two time points. Statistical difference was tested via the Mann-Whitney U test, setting $p<0.05$ as statistically significant.

RESULTS

SPECT/CT imaging and in vivo quantification

After functionalization, P94-DTPA was successfully radiolabeled with ^{111}In (labeling yield >90%). P94-^{111}In-DTPA copolymers were injected in tumor bearing mice either IV or IT. The levels of radioactivity reached in selected organs were followed over-time and measured (Figure 3-4; Table 1-3).

Table 1. Biodistribution of P94-^{111}In-DTPA at different time points after intravenous injection (IV) in mice

	4 h		24 h		48 h		120 h	
kBq/mm^3	**Median**	**Range**	**Median**	**Range**	**Median**	**Range**	**Median**	**Range**
Bladder	0.590	0.197-0.744	0.056	0.044-0.079	0.032	0.055-0.035	0.027	0.020-0.077
Heart	0.178	0.119-0.206	0.094	0.046-0.104	0.037	0.027-0.135	0.025	0.015-0.118
Liver	0.355	0.277-0.374	0.292	0.277-0.250	0.261	0.214-0.331	0.192	0.214-0.331
Lungs	0.142	0.130-0.170	0.050	0.049-0.084	0.039	0.027-0.096	0.027	0.018-0.104
Kidney	0.125	0.096-0.224	0.070	0.051-0.091	0.051	0.032-0.068	0.032	0.026-0.041
Tumor	0.051	0.040-0.059	0.038	0.026-0.055	0.032	0.021-0.041	0.019	0.018-0.038

Data represent the median and the range (minimum-maximum) of radioactive signal determined from SPECT/CT images. Radioactive signal is expressed as kBq/mm^3; n=6 at 4 h, 24 h and 48 h pi; n=3 at 120 h pi.

In the SPECT/CT images, made 4 h pi of mice injected IV with P94-^{111}In-DTPA, we observe a strong radioactive signal in liver (~0.3 kBq/mm^3) and bladder (~0.6 kBq/mm^3), compatible with the clearance pathway of P94 copolymer (*8*) (Figure 3A; Table 1). At this time point radioactivity in the tumor was measured at <0.06 kBq/mm^3, or ~1.8% ID/g. Considerable levels of radioactivity were measured in other normal tissues such as heart (~0.17 kBq/mm^3), lungs (~0.14 kBq/mm^3) and kidney (~0.12 kBq/mm^3) (Figure 3B; Table 1). At subsequent time points, radioactivity decreased following one-phase decay curve in all investigated tissues (healthy and tumor), however at different decay rates (Figure 3B; Table 3). We observed highest retention of radioactivity in liver and tumor with a $T_{½}$ of 75 h (95% CI:

51-141 h) for tumor tissue and a $T_{½}$ of 102 h (95% CI: 77-152) for liver. Other normal organs showed much faster clearance with a $T_{½}$ between 6 and 28 h (Table 3).

Table 2. Biodistribution of P94-^{111}In-DTPA at different time points after intratumoral injection (IT)

	0.5 h		24 h		48 h		72 h	
kBq/mm³	**Median**	**Range**	**Median**	**Range**	**Median**	**Range**	**Median**	**Range**
Bladder	*	*	0.017	0.013-0.066	0.014	0-0.021	0.007	0-0.011
Heart	*	*	0.042	0.027-0.056	0.045	0.013-0.055	0.011	0.007-0.015
Liver	*	*	0.125	0.084-0.143	0.123	0.074-0.153	0.108	0.099-0.117
Lungs	*	*	0.035	0.02-0.066	0.047	0.023-0.066	0.016	0.013-0.018
Kidney	*	*	0.046	0.035-0.025	0.032	0.029-0.059	0.037	0.031-0.041
Tumor	3.02	2.9-4.27	0.544	0.403-0.621	0.418	0.378-0.479	0.374	0.326-0.421

Data represent the median and the range (minimum-maximum) of radioactive signal determined from SPECT/CT images. Radioactive signal is expressed as kBq/mm³ (n=6) at 0.5 h, 24 h, 48 h pi; (n= 3) at 72 h pi. *: SPECT scan focused on the tumor region, organ not detectable.

Table 3. $T_{½}$, Plateau, Amplitude and R^2 of P94-^{111}In-DTPA after IV injection in different organs and after IV or IT injection in the tumor

	$T_{½}$ [h]	$T_{½}$ (95% CI) [h]	Plateau [kBq/mm³]	A [kB/mm³]	R^2
Bladder	6.5	3-23	0	0.83	0.83
Liver	102	77-152	0	0.36	0.76
Heart	11.4	5-159	0.04	0.16	0.75
Kidney	28	19-51	0	0.14	0.68
Lungs	7.8	4-56	0.04	0.14	0.81
Tumor (IV)	75	51-141	0	0.05	0.61
Tumor (IT)	0.2	0.19-0.23	0.4	15.54	0.99

The half-lives of P94-^{111}In-DTPA in the different organs and in the tumor were calculated on the one phase decay fitting curve (equation 1). $T_{½}$ represents the clearance half-life expressed in hours and the 95% CI is given; Plateau: $\lim_{t\to\infty} y(t)$; A: amplitude of the function between t=0 and Plateau; R^2: coefficient of determination; CI: confidence interval.

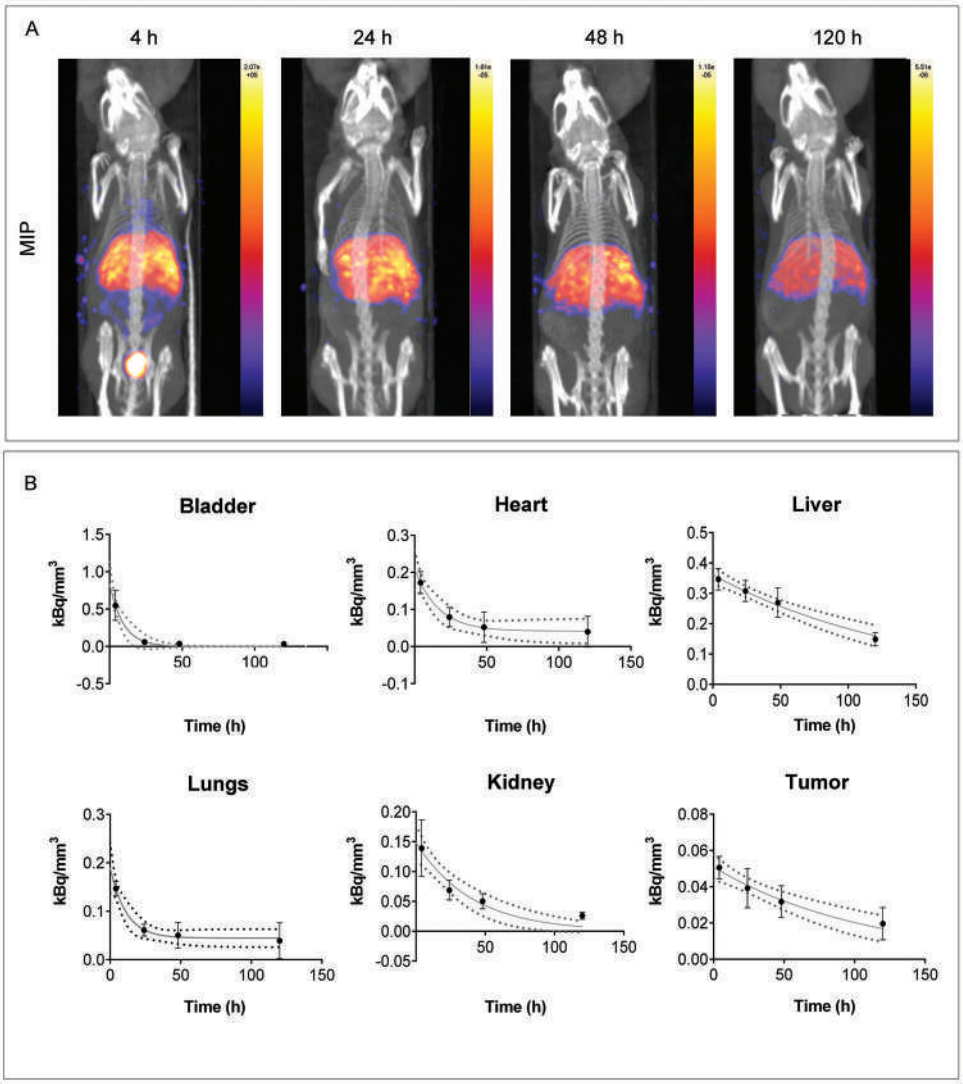

Figure 3. P94-^{111}In-DTPA biodistribution after intravenous (IV) injection. A) Whole body maximum intensity projection SPECT/CT images of randomly selected mice at 4, 24, 48 and 120 h pi, after the IV injection of P94-^{111}In-DTPA; B) Kinetics of measured activity based on images in selected organs. The points represent the mean of the measured values for each organ ± standard deviation. The data are fitted using a one-phase decay curve (gray line); spotted lines represent the 95% confidence interval. MIP: maximum intensity projection.

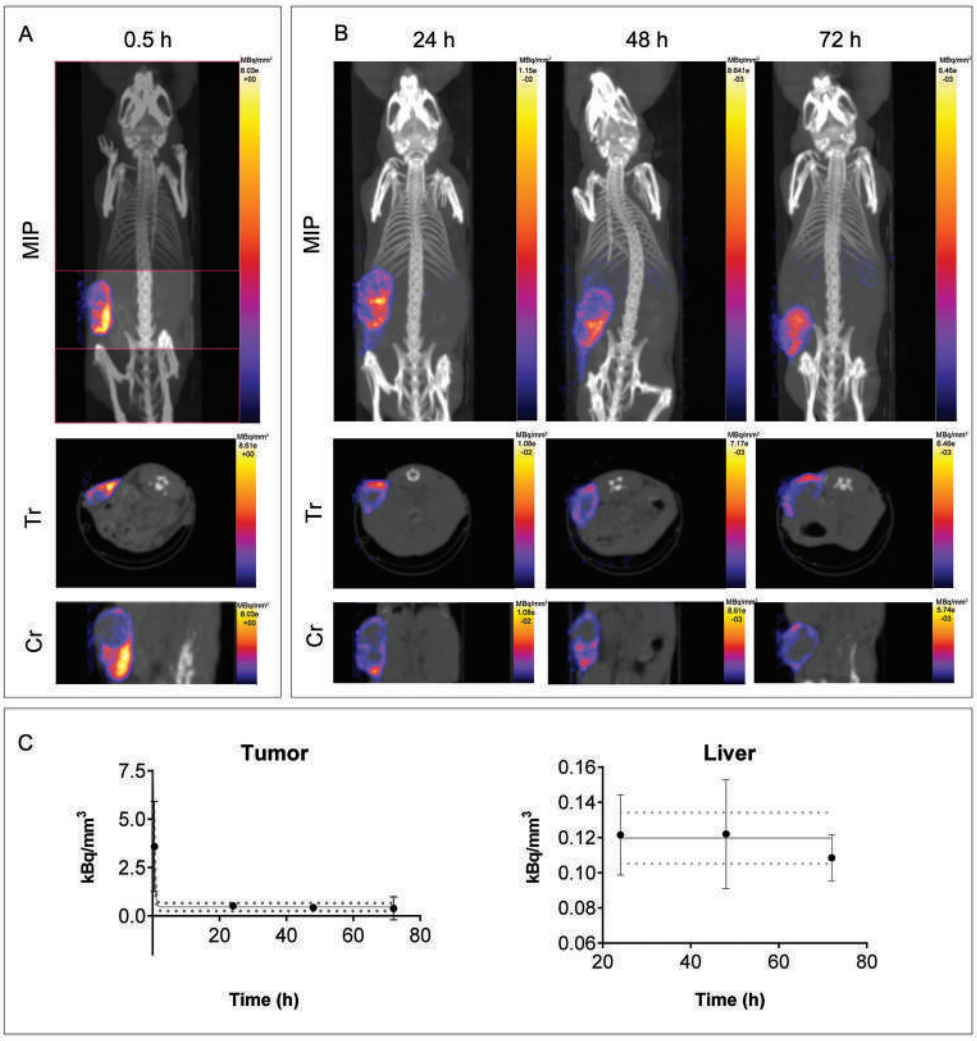

Figure 4. P94-^{111}In-DTPA biodistribution after intratumoral (IT) injection. A) Focused SPECT images at 0.5 h pi in the tumor region; margins of the scan are delimited in the image by the pink lines. Whole body CT was performed for anatomical reference. From top to bottom: maximum intensity projection (MIP), transversal view (Tr) and coronal view (Cr); B) Whole body SPECT/CT (24, 48 and 72 h pi) images of randomly selected mice. From top to bottom: MIP, Tr view and Cr view; C) Kinetics of measured activity based on images in tumor and liver. The tumor is fitted following a one-phase-decay curve (gray curve). Liver is fitted with a linear curve (gray curve). The points represent the mean measured values for each organ ± standard deviation; spotted lines represent the 95% confidence interval. MIP: maximum intensity projection. Cr: coronal view; Tr: transversal view

Following IT injection of P94-^{111}In-DTPA, a marked presence of radioactivity in the tumor was detected (between 2.9 and 4.27 kBq/mm^3 or 10-12% ID/g) from the early time point of 0.5 h pi to 72 h pi (Figure 4A). At later time points, radioactivity was discernable or measurable also in other organs although at a low level, and only the liver was visible in the images (Figure 4B). In the tumor, most of the radioactivity in the SPECT/CT images was seen towards the rim, suggesting a fast redistribution of radioactivity from the center to the periphery (see coronal and transversal images in Figure 4A-B). The analyses over the fitted curves, indicated that the radioactivity in the tumor halved in the first 0.2 h, and rapidly reached a plateau at a level of ~0.4 kBq/mm^3 (around 12% ID/g) in the first hours (Figure 4C; Table 2-3). In liver at later time points, the measured signal is most likely resulted from the activity released from the tumor shortly after IT injection. By fitting the levels of radioactivity in the liver over-time no further increase in radioactivity uptake in this organ was found (Figure 4C).

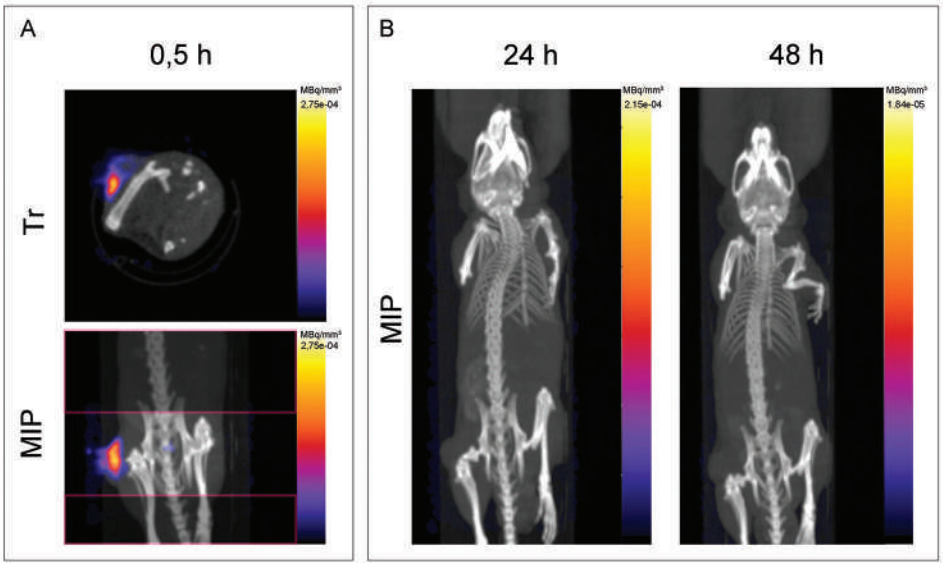

Figure 5. Biodistribution of ^{111}In-DTPA after intratumoral (IT) injection. A) Focused SPECT/CT images at 0.5 h pi in the region of the tumor; margins of the scan are delimited in the image by the pink lines. CT was performed for anatomical reference. From top to bottom: Tr view; MIP; B) SPECT/CT whole body MIP image (24 and 48 h pi) of a randomly selected mouse of the control group. Tr: transversal view; MIP: maximum intensity projection.

In contrast to the results obtained with P94-^{111}In-DTPA, IT injection of ^{111}In-DTPA did not result in prolonged presence of radioactivity in the tumor (Figure 5). Only in the SPECT/CT images taken shortly after injection (0.5 h pi) (Figure 5A) radioactive signal in the tumor mass could be detected. At the later time points (≥24 h pi) no activity in any anatomical location was detectable in the SPECT/CT images (Figure 5B).

Biodistribution results

Analysis of radioactivity in isolated organs and tissues 48 and 72/120 h pi confirmed uptake and retention profiles seen in SPECT/CT images. At 48 h post IV injection, we measured a considerable radioactive signal (median >2% ID/g) in the clearance organs (represented by liver, spleen and kidney), but also in other off-target tissues, were the median of the measured radioactivity was generally above 1% ID/g (Table 4). In the tumor the median of the measured radioactivity after IV injection of P94-^{111}In-DTPA was around 1% ID/g (Table 4).

In contrast, the biodistribution of P94-^{111}In-DTPA after IT injection showed high signal in the tumor mass that reached values up to ~30% ID/g (Table 4). Within the clearance organs, we could measure considerable radioactive signal only in the liver (~5% ID/g), while in the other clearance organs, spleen and kidney, the measured radioactivity was <1% ID/g (Table 4).

Measurements made on the heart after IV and IT injection revealed a substantial level of radioactivity even at 48 and 72/120 h pi (Table 4) suggesting that a the tracer is probably still in the circulation even at relatively late time points.

Data from tumors isolated at 48 h and 72/120 h pi revealed no statistically significant difference ($p>0.05$) in levels of radioactivity between the two time points, irrespective of the injection route used. This indicates that after radioactivity is in the tumor (either because of the contribution of EPR effect or because of a direct injection) P94-^{111}In-DTPA is well retained over-time.

In the off-target tissues after the IV injection, we measured a reduction of radioactivity between 48 and 120 h pi ($p<0.05$) indicating a substantial clearance (Figure 6A). The only exception, showing no significant difference between the two investigated time point ($p>0.05$) and therefore a stable level over that time-window was represented by the organs involved in the clearance of P94 polymers: namely liver and spleen. Much lower levels in general were found in normal organs after IT; however, at the studied time points, a significant decrease in activity was seen only for the kidney, while no significant difference was measured for all other organs (Figure 6B).

The biodistribution analyses of the control group after IT injection of ^{111}In-DTPA at 48 h pi, confirmed the results already obtained by SPECT/CT imaging (Figure 5). The radioactivity measured in the tumor was ~0.4% ID/g, and very low levels of radioactivity were measured in any of the organs and tissues <<0.01% ID/g, and considered negligible (Figure 6C).

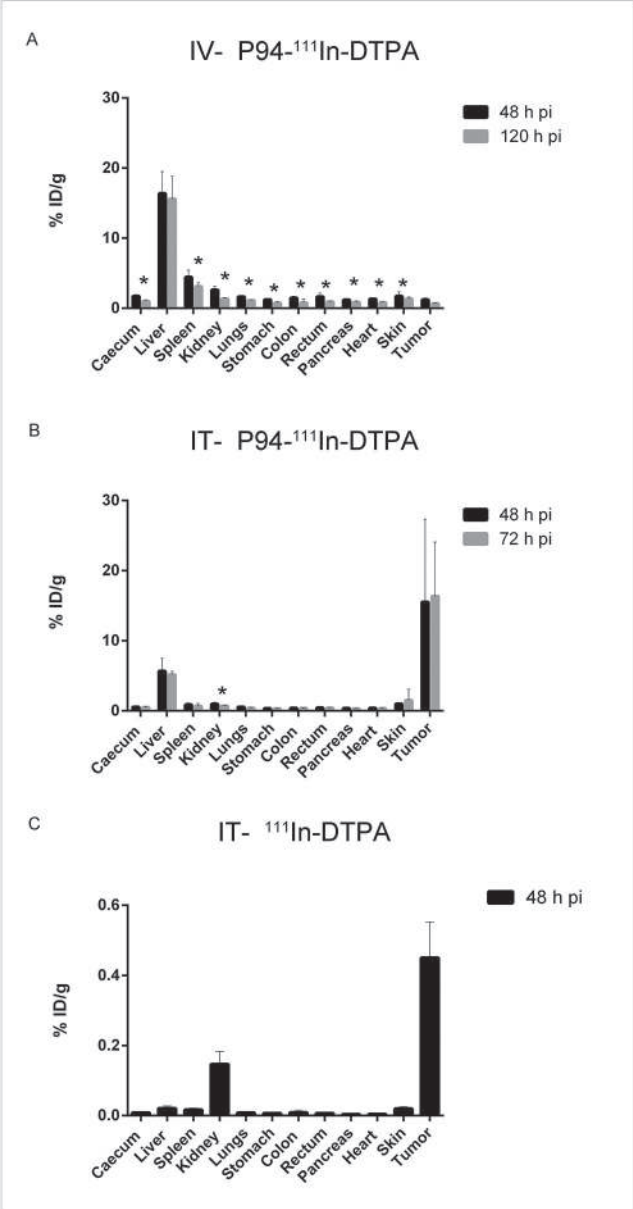

Figure 6. Biodistribution results obtained from selected organs at 48 and 72/120 h. A) Intravenous (IV) injection of P94-^{111}In-DTPA; B) intratumoral (IT) injection of P94-^{111}In-DTPA; C) IT injection of ^{111}In-DTPA. Note the scale difference between the graphs. Bars represent mean ± standard deviation. *: statistical significance between the two time points ($p<0.05$), 48 vs 120 h pi for IV and 48 and 72 for IT.

DISCUSSION

The results recently obtained with P94 copolymer have underlined valuable properties of this copolymer for in vivo application as nanocarrier (*8*). These properties are represented by the long lasting stability and potential anti-cancer cell effect, strongly indicating that P94 copolymer has the potential to be a carrier for drug delivery in tumors (*7, 8*). Successful application of a nanocarrier in vivo, however, depends on its capacity to target tumor tissue, in a safe, efficient and specific way. This includes, next to a sufficiently high delivery to the tumor, low accumulation of the nanocarrier in off-target tissue in order to maximize the amount that is available for tumor uptake but also to reduce toxicity to healthy tissues.

In this study we tested the potential of P94 copolymer to accumulate in tumor tissue following IV injection, which is the most commonly used administration route of anticancer drugs. However, upon direct injection in the circulation, elevated accumulation of nanoparticles in clearance organs is a known effect (*21, 22*), and consistent accumulation of P94-^{111}In-DTPA in liver, spleen and kidney was shown in previous studies as well (*8*). In order to reduce the accumulation in clearance organs and potentially improve the tumor retention, we also studied the biodistribution of P94-^{111}In-DTPA after injection via a different route, namely following IT injection (*17, 18*).

To accommodate the requirement for EPR-mediated tumor delivery of the radiolabeled polymer, we performed the studies in the subcutaneous, H69 xenograft tumor model. This tumor model in mice has already been described as a relevant model to study EPR-mediated accumulation with other nanoparticles (*23*). H69 tumors are characterized by a fast growth rate and early formation of a network of immature and leaky vessels, which favor the enhanced extravasation of nanosized particles and, ultimately, their retention in the tumor tissue (*24*).

The results obtained after the IV injection of P94-^{111}In-DTPA showed durable presence of radioactivity in the tumor, with the level of radioactivity remaining stable between 48 and 120 h pi. The levels of activity reached in the tumor after IV injection were fairly low (up to 2.8% ID/g) but are in line with the average levels of accumulation of various nanoparticles due to the EPR effect (*11*) and indicated P94-^{111}In-DTPA accumulation.

Following IV injection relatively high levels of radioactivity were found in the liver throughout the follow-up period, probably as a result of clearance via the hepatobiliary system and stable accumulation of P94-^{111}In-DTPA (*8*). Radioactivity in other off-target tissues was often not directly attributable to tissue accumulation of P94-^{111}In-DTPA, but was instead the result of the long lasting circulation of radioactivity or physiological clearance mechanism. A specific example of the latter is the radioactivity measured in the digestive tract, which is most likely resulting from the hepatobiliary excretion, as has been shown before to be a common excretion pathway (*8*). The radioactivity found in the stomach at a relatively high level in

comparison with other tissues can in part be explained by the phenomenon of self- and social grooming often occurring between mice (23).

In comparison to the result obtained with IV injection, local (intratumoral) injections of P94-^{111}In-DTPA provided a markedly different biodistribution profile. After IT injection of P94-^{111}In-DTPA, we found high levels of radioactivity in the tumor which were up to 10 times higher than the levels found in other organs. Moreover, the radioactivity found in the off-target tissues was roughly three times lower for IT compared to IV, indicating a preferential biodistribution profile of P94-^{111}In-DTPA when it is injected locally.

The presence of radioactivity in the off-target tissue after IT injection, and especially in the liver, which is involved in the clearance of P94 copolymer, is an indication that the injected P94-^{111}In-DTPA is released from the tumor in to the systemic circulation. This assumption is supported by SPECT/CT images showing a fast relocation of signal from the center to the tumor rim, alongside a rapid reduction of radioactivity (~70-95%) within the first 0.5 h pi. This effect is probably the result of the intra-tumor pressure, driving fluids to the periphery as a consequence of the differences in hydrostatic pressure between the tumor and the interstitium (*25, 26*). Despite the extensive release of radioactivity from the tumor after IT injection, still ~10% (range 3-30%) of the injected dose is stably retained in the tumor for at least 72 h. This is much higher than levels found with other radiolabeled agents injected IT (*27*), where only ~1% of the injected agent was detectable at 24 h pi. Our findings therefore confirm the potential of P94-^{111}In-DTPA to improve the retention within tumor tissues.

The results obtained following injection with ^{111}In-DTPA, further suggested that retention in the tumor is mediated by the P94 copolymer. From previous investigation, it is known that ^{111}In-DTPA when in circulation is rapidly cleared via the renal path (*28*). After the injection of ^{111}In-DTPA we observed a considerable reduction of radioactivity in the tumor between the 0.5 and 24 h pi (less than 0.5% ID/g was found 48 h after the injection of ^{111}In-DTPA), which suggest a rapid release of ^{111}In-DTPA from the tumor to the blood stream. In our biodistribution studies with the control group injected with ^{111}In-DTPA, we also measured low levels of radioactivity at 48 h pi in the kidney; which was indicative of release from the tumor to the circulation and renal clearance.

These results suggest that the P94 copolymer plays a decisive role in the retention within the tumor. In line with previous in vitro result, the long lasting retention might be associated to with the ability of P94 copolymer to be internalized by tumor cells (*7*), although further studies would have to be performed to determine if and to which extent the internalization occurs in in vivo settings as well.

The clearance/retention of P94 copolymer in normal tissue and in the circulation is finally an important parameter to consider for further application. In previous investigations it was

shown that after IV injection of P94-^{111}In-DTPA, it was still detectable at considerable levels at 48 h pi in the heart region (*8*) suggesting a long lasting presence of the copolymer in the circulation. In line with that finding, we could detect a considerable amount of radioactivity in the heart at 48 h, and up to 120 h pi, supporting the elevated in vivo stability of P94-^{111}In-DTPA. Radioactivity in the heart at 48 and at 72 h pi could be measured after IT injection as well, further confirming the substantial leakage from the tumor. However, in both the IV and IT groups, the signal measured in the heart was largely below the levels of tumor and liver, but it was comparable to that of the other off-target tissue. The circulation might, therefore, give an important contribution to the levels of radioactivity measured in every tissue.

Part of the measured radioactivity in off-target tissue would therefore result from the circulation and, over-time, it would follow the trend of biodistribution found heart (i.e. circulation). Together with the significant decrease of radioactivity found in the heart, between the last two time points, after IV injection of P94-^{111}In-DTPA, in many of the other investigated organs we also found a correspondent significant reduction of radioactivity. In contrast, no significant difference in radioactivity levels was found in the heart between the last two time points after IT injection of P94-^{111}In-DTPA, and no difference in the off-target tissue levels was found. The results, moreover, suggest that effective accumulation in off-target tissues only occurs in specific organs (namely clearance organs, and especially liver), while it only limitedly affects the other tissues in the body.

Of note, independently from the injection route, we found no difference in the levels measured in the tumors between the last two time points. This results probably from the poor clearance occurring from the tumor (*11*), but also indicates stable retention of P94-^{111}In-DTPA over-time and further underlines the potential of this polymer for the delivery of drug in tumors. On the other hand IT is efficient only in specific cancer types, which may limit the applicability of that injection route.

In conclusion, IV injection of P94-^{111}In-DTPA does not result in a particularly favorable biodistribution profile when compared to other nanoparticles, but showed a long lasting retention of radioactivity in the tumor. IT injection of P94-^{111}In-DTPA does result in prolonged high levels of activity in the tumor together with low involvement of off-target tissue.

Our results confirm the potential of P94 copolymer as a carrier following both IV and IT injection routes, possibly for the delivery of drugs or other therapeutic agents to solid cancers.

Acknowledgments

This work was performed on the imaging equipment in the Applied Molecular Imaging at the Erasmus MC (AMIE) facility. The authors would like to thank all the members of the consortium under the Marie Curie Actions ("Trace'n'Treat") and Mark Konijnenberg for their support, collaboration and fruitful discussions.

REFERENCES

1. Alakhova DY, Kabanov AV. Pluronics and MDR reversal: an update. *Mol Pharm.* 2014;11:2566-2578.
2. Chiappetta DA, Sosnik A. Poly(ethylene oxide)-poly(propylene oxide) block copolymer micelles as drug delivery agents: improved hydrosolubility, stability and bioavailability of drugs. *Eur J Pharm Biopharm.* 2007;66:303-317.
3. Moghimi SM, Hunter AC. Poloxamers and poloxamines in nanoparticle engineering and experimental medicine. *Trends in Biotechnology.* 2000;18:412-420.
4. Pitto-Barry A, Barry NPE. Pluronic[registered sign] block-copolymers in medicine: from chemical and biological versatility to rationalisation and clinical advances. *Polymer Chemistry.* 2014;5:3291-3297.
5. Moloughney JG, Weisleder N. Poloxamer 188 (P188) as a Membrane Resealing Reagent in Biomedical Applications. *Recent patents on biotechnology.* 2012;6:200-211.
6. Arranja A, Schroder AP, Schmutz M, Waton G, Schosseler F, Mendes E. Cytotoxicity and internalization of Pluronic micelles stabilized by core cross-linking. *Journal of Controlled Release.* 2014;196:87-95.
7. Arranja A, Denkova AG, Morawska K, et al. Interactions of Pluronic nanocarriers with 2D and 3D cell cultures: Effects of PEO block length and aggregation state. *Journal of Controlled Release.* 2016;224:126-135.
8. Arranja A, Ivashchenko O, Denkova AG, et al. SPECT/CT Imaging of Pluronic Nanocarriers with Varying Poly(ethylene oxide) Block Length and Aggregation State. *Mol Pharm.* 2016;13:1158-1165.
9. Kiessling F, Mertens ME, Grimm J, Lammers T. Nanoparticles for imaging: top or flop? *Radiology.* 2014;273:10-28.
10. Maeda H. Macromolecular therapeutics in cancer treatment: the EPR effect and beyond. *J Control Release.* 2012;164:138-144.
11. Noguchi Y, Wu J, Duncan R, et al. Early phase tumor accumulation of macromolecules: a great difference in clearance rate between tumor and normal tissues. *Jpn J Cancer Res.* 1998;89:307-314.
12. Lammers T, Kiessling F, Hennink WE, Storm G. Drug targeting to tumors: principles, pitfalls and (pre-) clinical progress. *J Control Release.* 2012;161:175-187.
13. Blanco E, Shen H, Ferrari M. Principles of nanoparticle design for overcoming biological barriers to drug delivery. *Nat Biotech.* 2015;33:941-951.
14. Duncan R, Gaspar R. Nanomedicine(s) under the microscope. *Mol Pharm.* 2011;8:2101-2141.
15. Albanese A, Tang PS, Chan WC. The effect of nanoparticle size, shape, and surface chemistry on biological systems. *Annu Rev Biomed Eng.* 2012;14:1-16.
16. Al-Abd AM, Aljehani ZK, Gazzaz RW, et al. Pharmacokinetic strategies to improve drug penetration and entrapment within solid tumors. *J Control Release.* 2015;219:269-277.
17. Ray A, Williams MA, Meek SM, et al. A phase I study of intratumoral ipilimumab and interleukin-2 in patients with advanced melanoma. *Oncotarget.* 2016;6:10453.
18. Liang M, Fan K, Zhou M, et al. H-ferritin-nanocaged doxorubicin nanoparticles specifically target and kill tumors with a single-dose injection. *Proc Natl Acad Sci U S A.* 2014;111:14900-14905.
19. Arranja A, Waton G, Schosseler F, Mendes E. Lack of a unique kinetic pathway in the growth and decay of Pluronic micelles. *Soft Matter.* 2016;12:769-778.

20. Hoang B, Lee H, Reilly RM, Allen C. Noninvasive monitoring of the fate of 111In-labeled block copolymer micelles by high resolution and high sensitivity microSPECT/CT imaging. *Mol Pharm.* 2009;6:581-592.
21. Bertrand N, Leroux JC. The journey of a drug-carrier in the body: an anatomo-physiological perspective. *J Control Release.* 2012;161:152-163.
22. Yu M, Zheng J. Clearance Pathways and Tumor Targeting of Imaging Nanoparticles. *ACS Nano.* 2015;9:6655-6674.
23. Moreira JN, Hansen CB, Gaspar R, Allen TM. A growth factor antagonist as a targeting agent for sterically stabilized liposomes in human small cell lung cancer. *Biochim Biophys Acta.* 2001;1:303-317.
24. Weis SM, Cheresh DA. Tumor angiogenesis: molecular pathways and therapeutic targets. *Nat Med.* 2011;17:1359-1370.
25. Munson JM, Shieh AC. Interstitial fluid flow in cancer: implications for disease progression and treatment. *Cancer Manag Res.* 2014;6:317-328.
26. Boucher Y, Jain RK. Microvascular pressure is the principal driving force for interstitial hypertension in solid tumors: implications for vascular collapse. *Cancer Res.* 1992;52:5110-5114.
27. Roelcke U, Hausmann O, Merlo A, et al. PET imaging drug distribution after intratumoral injection: the case for (124)I-iododeoxyuridine in malignant gliomas. *J Nucl Med.* 2002;43:1444-1451.
28. Breeman WA, van der Wansem K, Bernard BF, et al. The addition of DTPA to [177Lu-DOTA0,Tyr3]octreotate prior to administration reduces rat skeleton uptake of radioactivity. *Eur J Nucl Med Mol Imaging.* 2003;30:312-315.

513958-L-sub01-bw-Santini
Processed on: 22-9-2017

CHAPTER 3.2

Radiolabeling polymeric micelles for in vivo evaluation: a novel, fast, and facile method

Published in EJNMMI Research

Santini C, Laan AC*, Jennings L, de Jong M, Bernsen MR, Denkova AG*

EJNMMI Res. 2016 Dec;6(1):12. doi: 0.1186/s13550-016-0167-x. Epub. 2016 Feb 9.
PubMed PMID: 26860294; PubMed Central PMCID: PMC4747947

**The authors contributed equally to the manuscript*

ABSTRACT

Background: Single photon emission computed tomography (SPECT) is an indispensable tool in the determination of the in vivo fate of polymeric micelles. However, for this purpose, the micelles need to be radiolabeled, and almost all radiolabeling procedures published to date involve the conjugation of a chelating agent to the constituting polymer, which could actually affect their biodistribution. In this paper, we report a new facile method for radiolabeling polystyrene-b-poly(ethylene oxide) diblock copolymer micelles without the necessity of any chemical modification. Instead, we entrap the radiolabel (i.e., ^{111}In) in the micellar core during the formation of the micelles by using tropolone as lipophilic ligand.

Methods: Micelles were prepared by emulsifying a polymer solution in chloroform with a buffer containing ^{111}In and lipophilic ligand tropolone, by stirring for about 2 h. The produced micelles were physically characterized by means of dynamic light scattering and transmission electron microscopy. The biological properties of the radiolabeled micelles were determined by means of in vivo and ex vivo evaluation. SPECT analysis was done on Balb/c-nu mice, after administration of 1 mg micelles containing 22 MBq of ^{111}In. SPECT images were obtained over 24 h. Biodistribution of the micelles was assessed also ex vivo.

Results: The radiolabeling method is robust and reproducible with constant radiolabeling efficiency (~30 %) even at indium concentrations that are much higher than the necessary for in vivo studies, and the radiolabel retention is more than 80% in mouse serum at 48 h. Radiolabeled micelles having hydrodynamic radius of 97 ± 13 nm have been successfully evaluated in vivo and ex vivo in non-tumor-bearing mice, revealing significant blood circulation up to at least 24 h post injection, with low accumulation in most organs except for the liver and spleen, which are the natural organs for clearance of nanoparticles. **Conclusions**: An easy and robust radiolabeling method has been developed, and its applicability is demonstrated in animal studies, showing its value for future investigation of polymeric micelles as nanocarriers in tumor-bearing mice.

Keywords: radiolabeling, polymeric micelles, amphiphilic diblock copolymers, SPECT

BACKGROUND

Polymeric micelles are promising nanocarriers for pharmaceutical formulations due to their ability to encapsulate hydrophobic substances, overcoming in this way the poor solubility of some drugs and allowing transport through the blood stream to the site of interest (*1,2*). These micelles are constituted by amphiphilic block copolymers, which in aqueous solutions are able to self-assemble into supramolecular structures. In contrast to self-assemblies composed of low molecular weight surfactants, diblock copolymer micellar aggregates usually exhibit a low critical micelle concentration (CMC) which enhances their integrity even at low concentration (*3*). By varying the composition, the size, and the structure of the block copolymers, i.e., tuning the hydrophilic and hydrophobic block ratio, and/or by adjusting the micelle production method, it is possible to design polymeric micelles with well-defined dimensions and morphologies (*4,5*). These favorable characteristics of polymeric micelles have already led to clinical applications for systemic chemotherapy (*6,7*).

In these applications, bringing the micelles to the desired site is essential for therapeutic success, which can be accomplished by exploiting either active or passive targeting pathways. Nanocarriers in general can accumulate in diseased tissue due to the enhanced permeability and retention (EPR) effect, also referred to as passive targeting. Growing tissue, especially tumors, can establish new vascular systems to supply themselves with oxygen and nutrients. The newly formed vessels, however, have a discontinuous endothelium and lack of lymphatic drainage, enhancing in this way extravasation and retention of large particles over time (*8,9*). Long blood circulation time can increase the needed in vivo availability and is therefore an important factor to improve accumulation in tumor tissue. In active targeting, antibodies or peptides are used to ensure tumor uptake, but in the case of nanoparticles even when such targeting vectors are present, it is still imperative that these entities remain in blood circulation for sufficiently long time (*10*).

Even though the scientific community is gaining considerable knowledge about the various factors that can affect the biodistribution of nanoparticles, it is still difficult to predict the in vivo behavior of new formulations, making pre-clinical evaluation absolutely essential. Nuclear imaging approaches such as SPECT (single photon emission computed tomography) and PET (positron emission tomography) are very suitable for this purpose, since they offer high detection sensitivity at high temporal and spatial resolution. These techniques do, however, require radiolabeling of the micelles prior to imaging. Several methods for radiolabeling of polymeric micelles are described in the literature, all involving the conjugation of the micelles with a chelate or complexing agent (e.g., DOTA or DTPA) which requires additional synthetic steps (*11*). In addition, the attachment of such a chelate could alter the corona of the micelles and hence their biodistribution and pharmacokinetics (*12-14*).

In this paper, we present a new, facile radiolabeling method based on passive loading that is applied to micelles composed of the diblock copolymer polystyreneblock- poly(ethylene oxide) (PS-b-PEO). The non-ionic hydrophilic corona of the micelles is composed of PEO, often referred to as poly(ethylene glycol), which is commonly used in nano-particle formulations to enhance their stealthy surface chemistry(*2,13*). The hydrophobic counterpart is formed by the PS, which has a high glass transition temperature (T_g) and is extremely hydrophobic, ensuring stability of the micelles and a low release rate of any hydrophobic load (*14*). The radiolabeling method described here bypasses the covalent attachment of a chelating agent since a lipophilic ligand (tropolone) complexed with the radionuclide (in this case ^{111}In) is entrapped in the micellar core leaving the PEO corona unaffected. In this paper, we describe this radiolabeling strategy and demonstrate the ease and efficiency of this procedure as well as an initial in vivo evaluation of these micelles in healthy mice using SPECT.

EXPERIMENTAL SECTION

Chemicals

The block copolymer PS-b-PEO with a M_n (number average molar mass) of 9500-b-18,000 g/mol was purchased from Polymer Source (Quebec, Canada). The block copolymer was nearly monodisperse with a M_w/M_n ratio (Mw is the weight average molar mass) of 1.09. The $^{111}InCl_3$ was obtained as solution in 10 mM hydrochloric acid from Mallinckrodt Pharmaceuticals (Petten, The Netherlands) with a specific activity of 1.72 MBq/pmol. Indium chloride, Sephadex G-25 and Sepharose 4B size exclusion chromatography resins, 4-(2-hydroxyethyl)-1-piperazine ethanesulfonic acid (HEPES), and 1,4-piperazinediethanesulfonic acid sodium salt (PIPES) were purchased from Sigma Aldrich, and tropolone from Merck. Ultrapure water was prepared with the in-house Milli-Q system from Merck Millipore.

Production and radiolabeling of micelles

Formation of ^{111}In-tropolone complexes was executed by adding 50 kBq $^{111}InCl_3$ to 2.3 mL of 10 mM HEPES buffer solution (pH 7.4) containing 0.8 mM of tropolone. The sample was incubated for about 5 min at room temperature. Subsequently, 100 µL of a solution of PSb- PEO block copolymer in chloroform was added to reach a polymer concentration of 4.3 mg/mL. The mixture was stirred at room temperature in a fume hood using a glass stirring bar in an open glass vial for about 2 h until the chloroform had evaporated. Unencapsulated

^{111}In-tropolone was removed from the radiolabeled micelles by means of size exclusion chromatography (SEC) using a Sephadex G-25 column with a diameter of 1 cm and a length of 30 ± 1 cm, using 10 mM HCl as eluent. The ^{111}In activity in the eluted fractions was analyzed using a Wallac WIZARD^2 2480 Automatic Gamma Counter (PerkinElmer), by measuring the peak area of the 171- and 245-keV photon peaks. The labeling efficiency was determined as the amount of ^{111}In encapsulated in the micelles relative to the total amount of ^{111}In added to the sample.

Physical characterization of the micelles

Samples used for the physical characterization of the micelles were prepared exactly the same way as described above but using non-radioactive indium chloride. The sample used in the dynamic light scattering (DLS) studies was prepared in duplicate and contained 4.3 mg/mL PS-b-PEO. Prior to the measurements, the sample was diluted 10, 50, and 200 times using HEPES buffer and each diluted sample was measured three times following protocols described previously [15]. The DLS apparatus consisted of a JDS Uniphase 633 nm 35 mW laser, an ALV sp 125 s/w 93 goniometer, a fiber detector, and a PerkinElmer photon counter. An ALV-5000/epp correlator and software completed the set-up. The DLS sample cell was placed in a temperature-regulated bath containing toluene as the index-matching fluid. The intensity autocorrelation function, $g^{(2)}$ (τ), was determined at 90°. The measurements were performed at 22 ± 1°C. The R_H of the micelles was determined using the CONTIN method, and the radius was calculated from the diffusion coefficient of the particles using the Einstein-Stokes equation.

The samples used in the transmission electron microscopy (TEM) analysis contained 1.1 mg/mL and 4.3 mg/mL PS-b-PEO. Prior to analysis, a five-time dilution was made in HEPES buffer. A drop of the micellar solution was pipetted onto a carbon-coated copper grid of 200 mesh (Quantifoil, Jena, Germany). Excess liquid was removed with a tissue, and the grid was left to dry before placing the specimen into the microscope. A JEM 1400 TEM (JEOL) was used with a LaB6 electron source, operated at an acceleration voltage of 120 keV.

Partition studies

For the partition study, 4 mL of either PIPES or HEPES buffer, containing 0.8 μM tropolone and 5 kBq ^{111}In was mixed with an equal volume of chloroform during 30 s using a vortex. The aqueous and organic phases were left to separate gravimetrically, after which 1 mL of each phase was transferred into a counting vial and measured using the automatic gamma

counter described previously. The distribution ratio (D) of the ^{111}In was calculated according to the following equation:

$$D = \frac{[^{111}In]_{chloroform}}{[^{111}In]_{HEPES\ buffer}} \quad (1)$$

In which $[^{111}In]_{chloroform}$ is the concentration of 111In in the chloroform phase, and $[^{111}In]_{HEPES}$ buffer is the concentration of ^{111}In in the aqueous phase. The D was assessed at pH 4.5, 5.5, 6.5, 7.4, and 8.5.

Optimization of the radiolabeling parameters

In the optimization studies, the following parameters were sequentially tested: the polymer concentration, the ^{111}In activity (i.e., the amount of indium), the tropolone concentration, and the pH. The polymer concentration varied from 0.22 to 8.7 mg/mL. In the optimization of the indium activity studies, non-radioactive indium was used in addition to ^{111}In for safety reasons. The indium concentration ranged from 1.3 pM to 130 nM, corresponding to 5 kBq and 500 MBq ^{111}In per sample of 2.3 mL, respectively, which is referred to as ^{111}In equivalent. Stock solutions of non-radioactive InCl3 were prepared in 10 mM HCl, and for quantification, either 5 or 50 kBq of ^{111}In was added to the sample. The tropolone concentration was varied from 0.8 nM to 80 μM, using stock solutions of tropolone in HEPES. PIPES buffers at pH 4.5, 5.5, and 6.5 and HEPES buffers at pH 7.4 and 8.5 were used in the pH optimization studies.

Radiolabeling of preformed micelles

The micelles were prepared as follows: 100 μL of a PSb-PEO block copolymer solution in chloroform was added to 2.3 mL of HEPES buffer containing 0.8 mM tropolone. The mixture was stirred until the chloroform had evaporated. To this solution, ^{111}In-tropolone chloroform solution was added in portions of 2 μL, which was itself prepared by extracting the ^{111}In into chloroform from a solution containing 1 mM tropolone in HEPES. The addition was done at 30-s intervals, until an activity of 50 kBq was reached. The unencapsulated ^{111}In-tropolone was removed from the radiolabeled micelles by means of SEC. The ^{111}In activity was measured as previously described using an automated gamma counter. Labeling efficiency was calculated relative to the total amount of ^{111}In added to the sample.

Retention studies

The retention of the ^{111}In radiolabel in the micelles was assessed in PBS and in mouse serum. For both samples, 3 mL of the radiolabeled micelles solution was mixed with an equal volume of either PBS or serum. As control, 1 mL of the same sample was analyzed on the day of preparation. The samples were stored in an incubator at 37 °C, and after 24 and 48 h, the retention of the radiolabel was analyzed. The micelles in the serum samples were separated from the released ^{111}In using a Sepharose 4B gel SEC column with a diameter of 1 cm and a length of 30 ± 1 cm. The micelles in the PBS were separated from the released ^{111}In by using a Sephadex G-25 SEC column having the same dimensions as in the serum studies, using 10 mM HCl as eluent.

In vivo and ex vivo evaluation

Micelles for in vivo tests were prepared as described in the "Production and radiolabeling of micelles" section, using a starting concentration of polymer adjusted to the number of animals and the required final polymer amount of 1 mg per animal. The sample was centrifuged for 90 min at 2300 g using Amicon® Ultra-4 centrifugal filter devices (Merck Millipore). The concentrated micellar solution was recovered from the filter and filled up to the required injection volume with PBS.

The biodistribution of PS-b-PEO micelles was tested in Balb/c-nu mice (Janvier Labs, Le Genest-Saint-Isle, France). Three mice received an injection of 200 µL of solution containing 22 MBq of ^{111}In in 1 mg of micelles. Immediately after the injection, the mice were anesthetized with a gas mixture of isoflurane (Pharmachemie, Haarlem, The Netherlands) (4 % induction, 2 % maintenance) and oxygen (0.8 %) and subjected to SPECT/CT scan (NanoSPECT/CT, Bioscan Inc., California, USA). One mouse, randomly chosen, was subjected to a dynamic scan during the first 60 min post injection (pi) using a matrix of 256 × 256 pixels, 16 projections, 20 s per projection. Static images were further acquired 30 min pi, 4 h pi, and 24 h pi, using a matrix of 256 × 256 pixels, 20 projections with 60 s per projection. A CT scan (240 projections, 500 ms exposure time 55 kVp tube voltage) was performed for anatomical reference. For biodistribution analyses after the last SPECT/CT acquisition, the mice were euthanized by cervical dislocation. Blood was immediately drawn via heart puncture and stored in a collection vial, then both the cadaver and the vial containing the collected blood were measured in a dose calibrator (Comecer VDC-404, COMECER Netherlands, Joure, The Netherlands) to have a measure of retention of radioactivity in the body. After the total body count, a selection of different organs was harvested. The uptake of the micelles in different tissues was calculated using the Wallac Wizard 1480 automated gamma counter (PerkinElmer) by measuring the emitted radiation. Part of the spleen, part of the

liver, and the complete right kidney of one mouse were collected and stored at −80 °C for ex vivo autoradiography evaluation. From the frozen tissues, 15-µm tissue sections were cut, mounted on glasses, and processed for ex vivo autoradiography. The slides were placed in a sensitive phosphor-imaging screen (PerkinElmer), and read out was performed 3 days later using the Cyclone Storage Phosphor System (Packard). Quantification of the autoradiograms was carried out with Optiquant (Software version 5.0. PerkinElmer). All animal experiments were performed in accordance with the Dutch animal welfare regulations and approved by the Central Animal Testing Committee (Dutch: Centrale Commissie Dierproeven).

DATA ANALYSIS

The obtained in vitro data were processed with Microsoft Excel (Microsoft Office Professional Plus 2010 package). ANOVA was used for statistical evaluation. All the in vivo data collected were analyzed with GraphPad Prism (GraphPad Software, version 5).

RESULTS

Physical characterization of the micelles

The morphology of the micelles has been assessed by DLS and TEM. Figure 1 shows the RH of the micelles for different dilutions. According to the DLS analysis, the micelles appear to have good stability upon dilution, having variations in the hydrodynamic radius within the measurement uncertainty. The overall average hydrodynamic radius has been found to be 97 ± 13 nm (N = 18).

Three representative TEM images of the micelles are given in Figure 2, in which the PS core is clearly visible as dark stains on a grey background. The PEO corona has lower electron density compared to the PS, and hence, it is (nearly) invisible. Most of the micelles appear to have spherical shape with diameter of the PS core ranging from 25 to 40 nm, irrespective of the polymer concentration. A small number of rod-like micelles with different lengths have also been observed (Figure 2c). Their presence can explain the larger dimensions of the micelles measured by DLS since the presence of a small number of large objects can contribute significantly to the scattered light signal leading to a shift of the apparent hydrodynamic size to larger values.

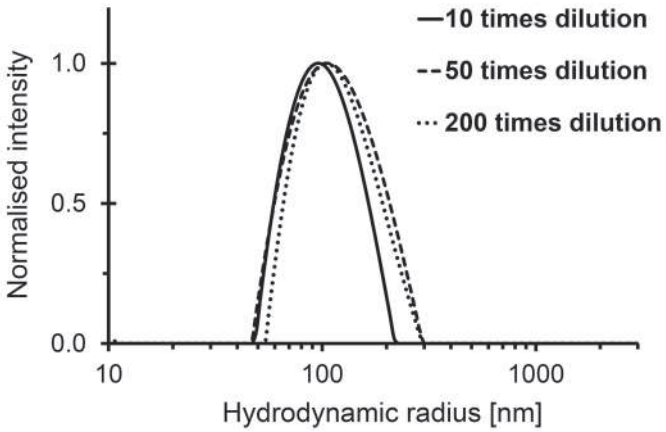

Figure 1. Size distribution of the PS-b-PEO micelles at a concentration of 4.3 mg/mL as determined by DLS, at three different dilutions.

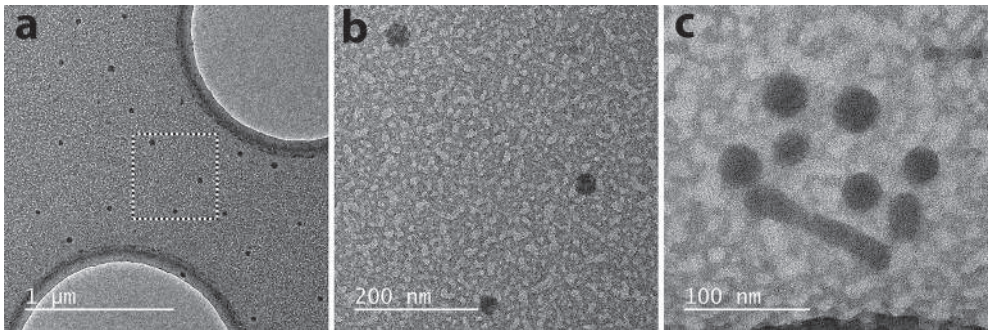

Figure 2. TEM images of PS-b-PEO micelles. a) spherical micelles, b) magnified image of A and c) a rod-like micelle between a few spherical ones. The concentration of A and B is 4.3 mg/ml and in C 1.1 mg/ml.

Radiolabeling

Prior to the optimization of the radiolabeling parameters, the distribution ratio, D, of ^{111}In in a mixture of chloroform and HEPES buffer containing tropolone had been determined. The obtained distribution ratio is 4.8 ± 0.5 indicating that in the presence of tropolone, indium has a clear preference for the organic phase, due, most likely, to the formation of an In-tropolone complex having lipophilic character. The results for D at pHs other than 7.4, given in Additional file 1: Table S1, show a comparable D values for pH 4.5 to 7.4 and a lower D for pH 8.5, i.e., 2.9 ± 0.2.

The radiolabeling efficiency increases with the polymer up to a value of 1.1 mg/mL, after which the encapsulated percentage remains constant, reaching a plateau at about 30% (Fig. 3a). At a block copolymer concentration of 4.3 mg/mL, there is an excess of micelles compared to the number of ^{111}In atoms (see Additional file 2 for the calculations), which implies that the labeling efficiency should be independent of the amount of indium. Indeed, the labeling efficiency appears to be the same up to the equivalent activities of 500 MBq (see Additional file 3: Figure S1).

The optimal tropolone concentration has been determined to be between 0.1 and 10 mM (Figure. 3b). At the lowest tested tropolone concentrations (0.8 μM), more than 50 % of ^{111}In has been found to stick to the glass vial or the stirrer, while above 10-mM free tropolone is expected to compete with ^{111}In-tropolone leading to a decrease in loading. Figure 3c shows the effect of the pH on the radiolabeling efficiency, revealing that even at pH 4.5, the labeling efficiency is still 34 ± 1 %, and it remains constant up to pH of 7.4. Only at higher pH values, >8, the efficiency slightly decreases to 29 ± 4 %.

As an alternative to the passive loading method, the radiolabeling of preformed micelles, referred to as 'active loading' has also been tested since it has previously been successfully applied in the radiolabeling of liposomes and polymersomes (*15*). In active loading, the ^{111}In-tropolone complex in chloroform is added to the preformed micelles to transport the 111In into the core of the micelles. The labeling efficiency of this method has been shown to be somewhat lower than the passive loading, 22 ± 3 % versus up to 32 ± 2 %.

Retention of ^{111}In

The loss of radiolabel has been assessed in both phosphate-buffered saline solution and in mouse serum (Figure 4). In saline, the micelles are stable having 95 ± 4 % of the ^{111}In still encapsulated in the micelles after 2 days of incubation. The retention of ^{111}In in serum is 83 ± 3 % and 81 ± 1 % after 1 and 2 days, respectively. In all samples, the same trend is observed: a fast release rate in 24 h followed by a negligible loss in the next 24 h.

In vivo evaluation

Dynamic SPECT/CT images in the first 68 min pi show that most of the activity is still in circulation (Fig. 5). Up to 4 h pi circulation is clearly detectable in the scans, making the major blood vessels and the heart chambers visible (Figures 5, 6a, b), while at 24 h, the SPECT data suggests that the micelles have primarily accumulated in the spleen and liver and are not found in the blood (Figures 6b, c).

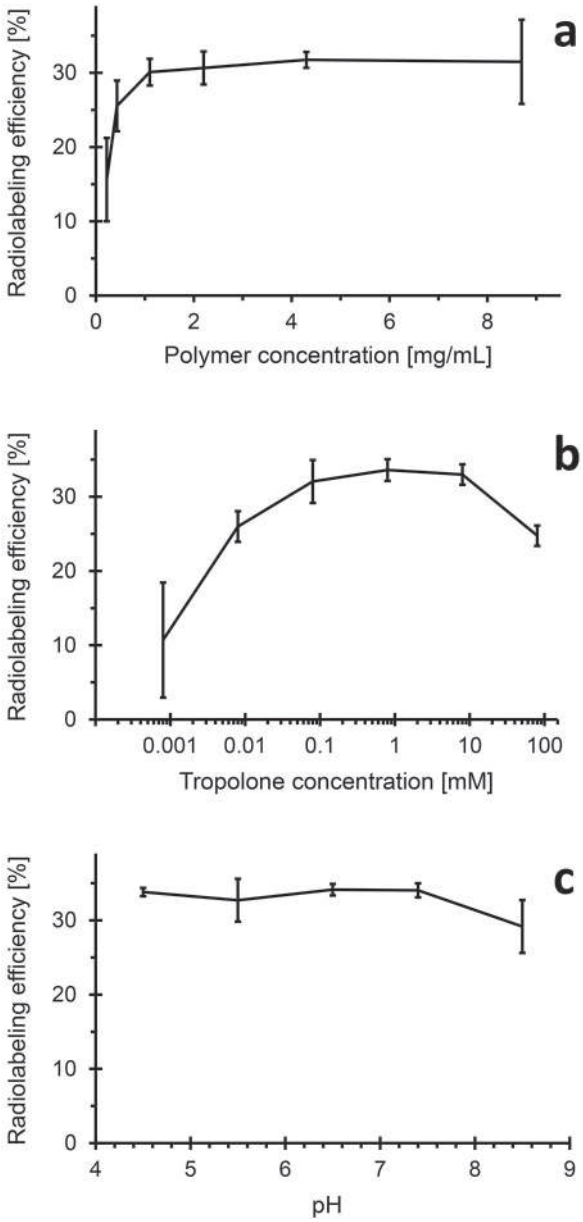

Figure 3. The radiolabeling efficiency as function of the PS-b-PEO micelles concentration (a), as function of the tropolone concentration and (b) as function of the pH (c). Default parameters are 4.3 mg/mL PS-b-PEO micelles, 0.8 mM tropolone in HEPES buffer at pH 7.4, containing 50 kBq ^{111}PIn. The uncertainty bars are the standard deviations (N=3).

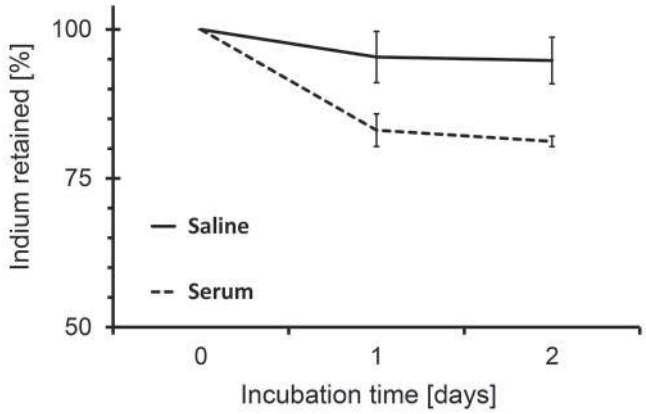

Figure 4. Retention of ^{111}In on micelles as function of time. The ^{111}PIn activity was 50 kBq per sample. The uncertainty bars are the standard deviations (N=3).

Whole-body retention of activity at 24 h pi has been estimated by measuring radioactivity levels in the extracted blood and the cadavers of euthanized animals, which show that more than 85 % of the injected activity has been retained in the body after 24 h. Ex vivo biodistribution analysis 24 h pi, expressed as a percentage of injected dose per gram of tissue (% ID/g), confirmed the observation made using SPECT/CT imaging, i.e., elevated spleen (176 ± 97 % ID/g) and liver uptake (30 ± 6 % ID/g) (Figures 7). Surprisingly, although circulation is not detectable via nuclear imaging at 24 h pi, the blood samples reveal relatively high percentage of activity (21 ± 8 % ID/g), indicating clearly that the micelles are still in circulation at this time point. The stomach also showed relatively high uptake being on average around 22.96 % ID/g.

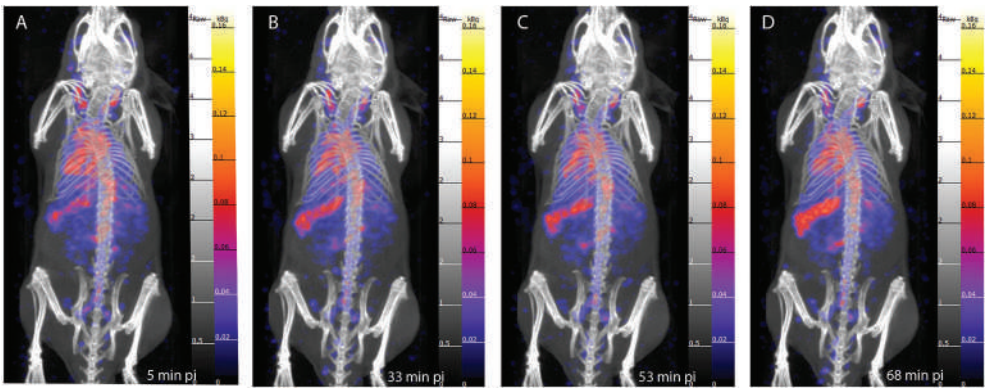

Figure 5. Four frames of a dynamic SPECT/CT scan of a non-tumor-bearing mouse, up to one hour pi.

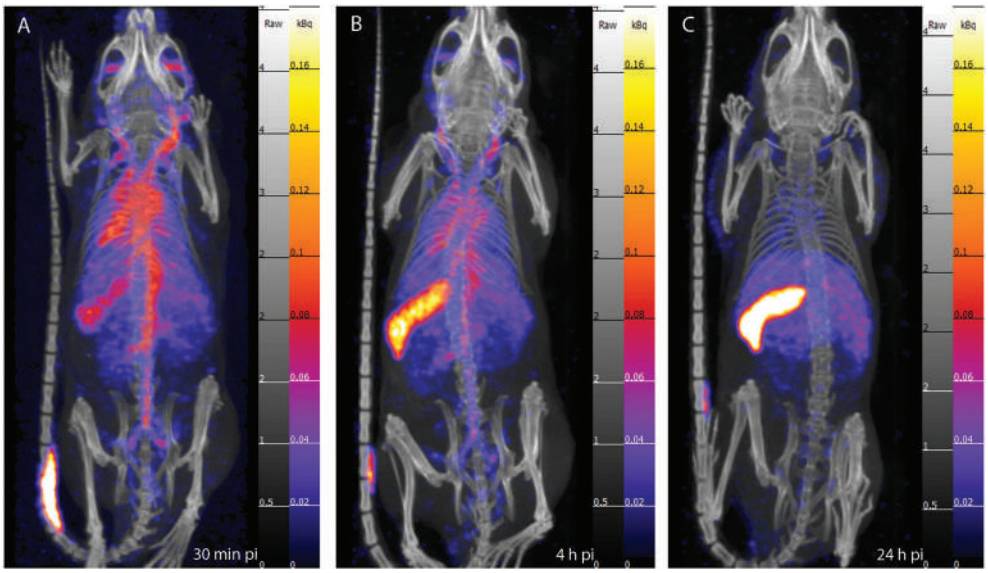

Figure 6. SPECT/CT scans of a non-tumor-bearing animal at time points 0 (a); 4 h (b) and 24 h (c) pi of a dose of 1 mg micelles containing 22 MBq of ^{111}PIn.

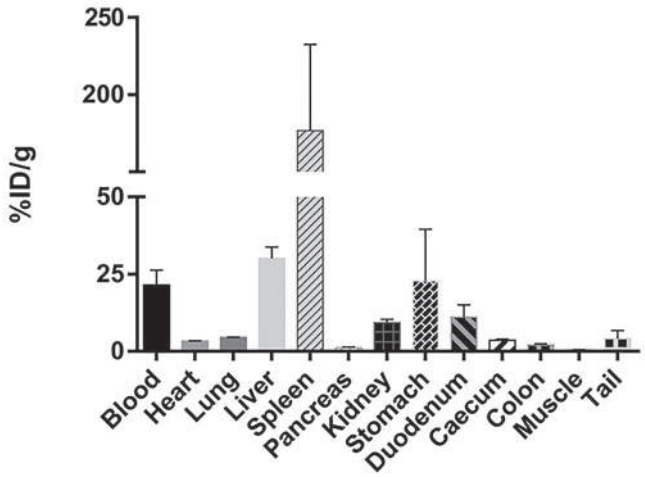

Figure 7. Biodistribution results of ^{111}PIn-PS-b-PEO micelles 24 h pi in non-tumor-bearing mice. Bar represent the average values of the calculated % ID/g ± standard deviations (N=3).

Ex vivo autoradiography

Ex vivo autoradiography has been carried out in the sections of the spleen, liver, and kidney. Accumulation in the liver and the kidney tissue appears to be homogeneous. In contrast, the spleen has non-homogenous staining pattern having areas with elevated uptake and smaller zones with lower retention. The observed staining pattern coincides with the anatomical architecture of the spleen with red pulp and white pulp zones, indicating high accumulation in the red pulp and low accumulation in the white pulp (Figure 8).

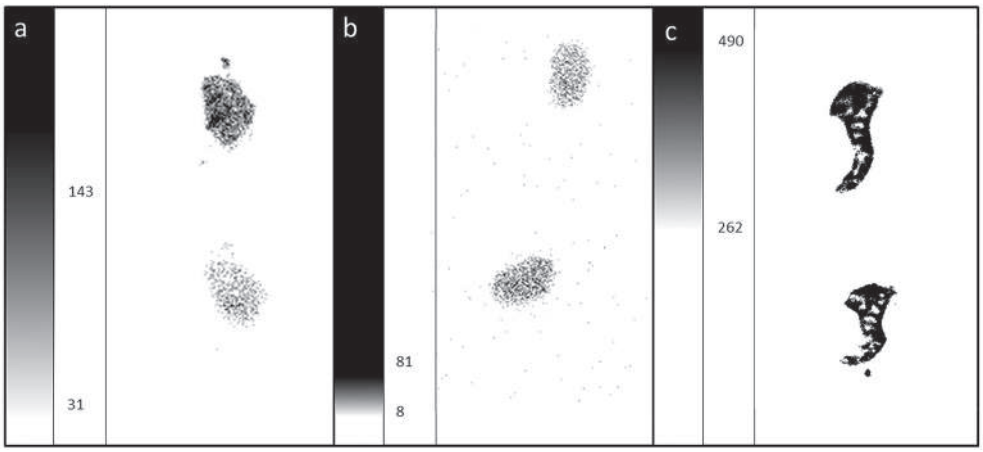

Figure 8. Autoradiography images; distribution of ^{111}In-PS-b-PEO micelles in liver, kidney and spleen 24 h pi. Two sections per organ are shown. The intensity scale is expressed in Digital Light Unit per surface (DLU/mm2): (a) liver (min: 31; max 143); (b) kidney (min 8; max 81); (c) spleen (min 262; max 490).

DISCUSSION

The aim of this study was to develop a simple and fast radiolabeling method for PS-b-PEO micelles which does not interfere with the intrinsic properties of micelles, allowing their evaluation in vivo using SPECT. Radiolabeling of polymeric carriers is typically carried out by the conjugation of a chelating molecule on their outer surface which has two main disadvantages: the properties of the nano-entities are altered and therefore possibly their behavior, and radiolabel integrity in vivo is often compromised (*16*). For instance, recently, it has been shown that polymersomes composed of the same block copolymer and having the same size exhibit different biodistribution and loss of radiolabel when radiolabeling is on the outer

surface versus enclosure in the aqueous cavity of the vesicles. The introduction of a chelating agent (i.e., DTPA) in this case resulted in somewhat negatively charged micelles which led to significantly higher liver uptake than when the PEG chains were not modified, preserving their neutrality (*16*). The potential of polymeric micelles as carriers for therapeutic agents, especially when envisioning drug delivery applications, should, hence, be assessed without changing their inherent qualities. In this study, we make use of the physical characteristics of the block copolymer, PSb-PEO (i.e., high T_g and extreme hydrophobicity) toencapsulate radionuclides in the micellar core, providing a novel and facile radiolabeling method that does not require chemical modifications, keeps the PEO corona intact, and protects the radiolabel from the biological environment.

The synthesis of the polymeric micelles is based on the spontaneous self-assembly of amphiphilic block copolymers into micellar structures due to formation of interfacial instabilities in chloroform-in-water emulsion droplets (*17*). When the PS-b-PEO block copolymers dispersed in chloroform are emulsified in water, they distribute at the (water-chloroform) interface in order to reduce the entropy of the system, which eventually leads to the formation of micelles as the chloroform evaporates. The mobility of the PS-b-PEO unimers in the micellar core is virtually non-existent due to the glassy behavior of polystyrene, leading to kinetically trapped structures having exceptionally high stability (*18*). This micellization process can be used to entrap lipophilic entities, such as in this case tropolone, which are present in the chloroform solution. Tropolone, being a ligand often used in radiolabeling, can be applied to passively bring a radio-metal to the micellar core, which is initially chloroform-rich, provided that the tropolone-metal complex has affinity for chloroform. The final evaporation of chloroform from the micellar structures results then in radiolabeled micelles. In this work, tropolone is complexed with indium (^{111}In) and their distribution ratio has been determined to be above 1, showing a tendency to accumulate in the chloroform phase. Since radiolabeling is in this case a passive process, the radiolabeling efficiency will be limited by the distribution ratio and the amount of chloroform present in the micellar core during micellization, which naturally will depend on the number and size of the micelles. This inherent limitation, however, makes the radiolabeling procedure highly reproducible, since there is only a slight dependence on the different radiolabeling parameters such as polymer, tropolone, and indium concentration, and surprisingly, also pH, as long as sufficient micelles are formed. For instance, the efficiency remains nearly the same for tropolone concentrations ranging from 0.1 to 10 mM. Only at higher amounts a decrease is seen which is explained by the fact that if there is an excess of free tropolone, i.e., percentage-wise less ^{111}In-labeled tropolone will be encapsulated, assuming that both species behave in a similar way (i.e., have a similar D value). The lack of dependence on indium concentration is logical since there is always a large excess of tropolone and polymer in the studied range, which allows encapsulating sufficient amount of activity at radiolabeling efficiency of 30%. One of the parameters expected to affect the radiolabeling efficiency is the pH, simply based on the pKa value of tropolone and the speciation of indium. In the tested pH range of 4.5 to 8.5, the radiolabeling efficiency remains the same between

pH 4.5 and 7.4 and only at pH 8.5 a small decline is observed. The same trend is observed for the distribution ratio, which is constant between pH 4.5 and 7.4 and is lower at pH 8.5. This decrease in the distribution ratio and in the labeling efficiency can be explained by the fact that at alkaline pH $In(OH)_4^-$ is formed which is unable to complex with the negatively charged ropolone (see Additional file 4: Figure S2 for the speciation chart). The anticipated reduction of labeling

efficiency at lower pH (<6.8) based on previous studies and the pKa value of tropolone (i.e., pKa 6.9) have not been observed. The structure of tropolone suggests that it will be partially situated at the water-chloroform interface and as such might have a different pKa value, enabling it to still extract indium even at somewhat acidic pH. This assumption also seems to be supported by the indium retention studies in serum, which reveal initial fast loss of radiolabel in the first 24 h followed by nearly no loss of any indium in the following 24 h. Such a loss profile can be ascribed to the distribution of In-tropolone in the micelles, i.e., it is very likely that some ^{111}In-tropolone complexes will be situated at the interface between the PEO corona and the PS core and will be much more prone to be taken from the micelles by scavenging proteins. Nevertheless, the loss of radiolabel is still limited (<19 %) and acceptable.

The radiolabeling procedure described in this manuscript is based on some general chemical principles and may be applicable to other block polymers exhibiting similar behavior as PEO-b-PS, i.e., having very slow exchange kinetics. In addition, this procedure would also be suitable for (simultaneous) encapsulation of a variety of radionuclides, provided that they are capable of complexing with tropolone or similarly behaving lipophilic ligands.

The success of any micellar formulation in systemic application is mainly dependent on the capacity of carriers to accumulate in diseased tissue with limited retention in healthy organs. The blood residence time has been identified as one of the most crucial aspect in achieving high tumor uptake (*19*), which in turn depends on the capability of the micelles to escape the body clearance mechanisms. Carriers of the size of PS-b-PEO micelles are usually cleared by macrophages in the liver and spleen, often also referred to as the mononuclear phagocyte system (MPS). PS-b-PEO micelles show a substantial retention in MPS organs, in line with previous observations evaluating the in vivo behavior of other nanoparticles similar in size and composition (*20,21*). In this respect, the morphology of the micelles influences the circulation time and the presence of rod-like micelles in our case might affect the circulation time; however, as the number of elongated species is low, the effect on the average circulation time is considered to be negligible. A particular pattern of accumulation has been observed in the spleen confirming the possible uptake by the splenic resident macrophages as a result of unspecific filtration process (*22*). This spleen uptake is in general higher when compared to other block copolymer micelles that have been investigated, which tend to exhibit more pronounced liver uptake (*23*). This discrepancy in biodistribution can be due to differences in charge of the investigated systems, and as mentioned earlier, all other systems include chelates

present on the surface of the micelles, which typically result in negatively charged micelles. In addition, the rigidity of the PS-b-PEO particles makes them more prone to spleen filtration. Apart from the blood, liver, and spleen, however, all the investigated organs show a low uptake profile (in average below 5 % ID/g) and little standard deviations indicative of a differential but homogeneous uptake in the various tissues. The surprisingly elevated stomach uptake is the result of one single animal, which explains as well the high standard deviation reported in the graph. This unexpected finding is probably not the result of tissue uptake/retention but could be ascribed to mice feeding behavior, i.e., daily coprophagy and social grooming (*24*). Although we have not determined the half-live of the micelles, the measured retention in blood is at 24 h still above 20 % ID/g which indicates that a large percentage of the micelles are still in circulation, which is comparable to a number of studies on polymeric micelles (*23*). Based on these results, we expect that these micelles will have long enough circulation time to ensure high tumor uptake, which should be further tested in tumor-bearing mice.

CONCLUSION

We have developed a new, easy, fast, and robust method to produce and radiolabel spherical PS-b-PEO block copolymer micelles. The radiolabeling efficiency is sufficient to achieve micelle activities of up to several hundred megabecquerel. Ex vivo results show blood circulation even 24 h pi, with high accumulation in the spleen and liver. Overall, these results are promising for further investigation of radiolabeling polymeric micelles and for the assessment of their fate in vivo.

SUPPORTING INFORMATION

A graphical representation of the effect of the indium activity on the radiolabeling efficiency, a calculation of the number ratio of ^{111}In nuclides and micelles, and speciation chart of indium over the full pH range. This material is available free of charge via the Internet at http://pubs.acs.org.

Author Contributions

‡These authors contributed equally. The manuscript was written through contributions of all authors. All authors have given approval to the final version of the manuscript.

Corresponding Author

* Adrie Laan, Delft University of Technology, Department of Radiation Science and Technology, Section of Radiation and Isotopes for Health. Mekelweg 15, 2629 JB Delft, The Netherlands, tel: (+31)15-2783968, e-mail: *2TUa.c.laan@tudelft.nlU2T*

* Costanza Santini, Erasmus MC, Department of Nuclear Medicine/Radiology, 's-Gravendijkwal 230, 3015 CE Rotterdam, The Netherlands, tel: (+31)107044971. e-mail: *2TUc.santini@erasmusmc.nlU2T*

Notes

The authors declare no competing financial interest.

Funding Sources

The research leading to these results was partially supported by People Programme (Marie Curie Actions) of the European Union's Seventh Framework Programme (FP7/2007-2013) under REA grant agreement no. PITN-GA-2012-317019 'TRACE 'n TREAT.

Acknowledgment

This work was supported through the use of imaging equipment provided by the Applied Molecular Imaging Erasmus MC facility.

Abbreviations

PS, polystyrene; PEO, poly(ethylene oxide); SPECT, Single-photon emission computed tomography; PET, positron emission tomography; DLS, dynamic light scattering; TEM, Transmission electron microscopy.

REFERENCES

1. Gohy J-F. Block Copolymer Micelles. 2005;190:65-136.
2. Adams ML, Lavasanifar A, Kwon GS. Amphiphilic block copolymers for drug delivery. *J Pharm Sci.* 2003;92:1343-1355.
3. Riess G. Micellization of block copolymers. *Progress in Polymer Science.* 2003;28:1107-1170.
4. Mai Y, Eisenberg A. Self-assembly of block copolymers. *Chem Soc Rev.* 2012;41:5969-5985.
5. Yoo JW, Chambers E, Mitragotri S. Factors that Control the Circulation Time of Nanoparticles in Blood: Challenges, Solutions and Future Prospects. *Current Pharmaceutical Design.* 2010;16:2298-2307.
6. Ahn HK, Jung M, Sym SJ, et al. A phase II trial of Cremorphor EL-free paclitaxel (Genexol-PM) and gemcitabine in patients with advanced non-small cell lung cancer. *Cancer Chemotherapy and Pharmacology.* 2014;74:277-282.
7. Kato K, Chin K, Yoshikawa T, et al. Phase II study of NK105, a paclitaxel-incorporating micellar nanoparticle, for previously treated advanced or recurrent gastric cancer. *Investigational New Drugs.* 2012;30:1621-1627.
8. Maeda H. The enhanced permeability and retention (EPR) effect in tumor vasculature: the key role of tumor-selective macromolecular drug targeting. *Advances in Enzyme Regulation.* 2001;41:189-207.
9. Peer D, Karp JM, Hong S, Farokhzad OC, Margalit R, Langer R. Nanocarriers as an emerging platform for cancer therapy. *Nat Nano.* 2007;2:751-760.
10. Moghimi SM, Hunter AC, Murray JC. Long-circulating and target-specific nanoparticles: theory to practice. *Pharmacol Rev.* 2001;53:283-318.
11. Oerlemans C, Bult W, Bos M, Storm G, Nijsen JF, Hennink WE. Polymeric micelles in anticancer therapy: targeting, imaging and triggered release. *Pharm Res.* 2010;27:2569-2589.
12. Patil RR, Yu J, Banerjee SR, et al. Probing In Vivo Trafficking of Polymer/DNA Micellar Nanoparticles Using SPECT/CT Imaging. *Molecular Therapy.* 2011;19:1626-1635.
13. Owen SC, Chan DPY, Shoichet MS. Polymeric micelle stability. *Nano Today.* 2012;7:53-65.
14. Rieger J. The glass transition temperature of polystyrene. *Journal of thermal analysis.* 1996;46:965-972.
15. Wang G, de Kruijff R, Stuart MCA, Mendes E, Wolterbeek HT, Denkova AG. Polymersomes as radionuclide carriers loaded via active ion transport through the hydrophobic bilayer. *Soft Matter.* 2013;9:727-734.
16. Brinkhuis RP, Stojanov K, Laverman P, et al. Size Dependent Biodistribution and SPECT Imaging of 111In-Labeled Polymersomes. *Bioconjugate Chemistry.* 2012;23:958-965.
17. Zhu J, Hayward RC. Spontaneous Generation of Amphiphilic Block Copolymer Micelles with Multiple Morphologies through Interfacial Instabilities. *Journal of the American Chemical Society.* 2008;130:7496-7502.
18. Gao Z, Lukyanov AN, Chakilam AR, Torchilin VP. PEG-PE/Phosphatidylcholine Mixed Immunomicelles Specifically Deliver Encapsulated Taxol to Tumor Cells of Different Origin and Promote their Efficient Killing. *Journal of Drug Targeting.* 2003;11:87-92.
19. Alexis F, Pridgen E, Molnar LK, Farokhzad OC. Factors Affecting the Clearance and Biodistribution of Polymeric Nanoparticles. *Molecular Pharmaceutics.* 2008;5:505-515.

20. Psimadas D, Georgoulias P, Valotassiou V, Loudos G. Molecular nanomedicine towards cancer: 111In-labeled nanoparticles. *J Pharm Sci.* 2012;101:2271-2280.

21. Lee H, Hoang B, Fonge H, Reilly RM, Allen C. In vivo distribution of polymeric nanoparticles at the whole-body, tumor, and cellular levels. *Pharm Res.* 2010;27:2343-2355.

22. den Haan JMM, Kraal G. Innate Immune Functions of Macrophage Subpopulations in the Spleen. *Journal of Innate Immunity.* 2012;4:437-445.

23. Jensen AI, Binderup T, Kumar Ek P, Kjær A, Rasmussen PH, Andresen TL. Positron Emission Tomography Based Analysis of Long-Circulating Cross-Linked Triblock Polymeric Micelles in a U87MG Mouse Xenograft Model and Comparison of DOTA and CB-TE2A as Chelators of Copper-64. *Biomacromolecules.* 2014;15:1625-1633.

24. Kenagy GJ, Hoyt D. Reingestion of feces in rodents and its daily rhythmicity. *Oecologia.* 1979;44:403-409.

25. Wilhelm M, Zhao CL, Wang Y, et al. Poly(styrene-ethylene oxide) block copolymer micelle formation in water: a fluorescence probe study. *Macromolecules.* 1991;24:1033-1040.

SUPPORTING INFORMATION

Calculation of the number ratio of ^{111}In nuclides and micelles

For calculation of the number of micelles we have used the aggregation number from the publication by Wilhelm et al.(*25*) For a PS-b-PEO block copolymer with a comparable size, i.e. for PS-b-PEO 11200-17500 an average aggregation number of 290 was reported. At a PS-b-PEO 9500-18000 concentration of 1.1 mg/mL in a default volume 2.3 mL the number of micelles will be:

$$\frac{1.1\times10^{-3}\ g/mL\times 2.3\ mL}{(9500+18000)\ g/mole}\ \mathrm{X}\ \frac{6.022\times10^{23}\ n/mole}{290\ n/micelle} = 1.91\times10^{14}\ micelles$$

The number of ^{111}In nuclides is directly proportional to the activity and can be calculated with the decay constant, λ, which for ^{111}In is 2.86 x 10^{-6} s^{-1} , for 50 MBq the number of nuclides is:

$$N = \frac{A}{\lambda} = \frac{50\times10^{6}s^{-1}}{2.86\times10^{-6}s^{-1}} = 1.74\times10^{13}\ nuclides$$

In this example there is about ten times excess of micelles compared to the number of ^{111}In nuclides, this means that part of the micelles will be present without radiolabel. In most practical situations the ratio will even be higher, so relatively more micelles will by without radiolabel.

The influence of the indium activity on the radiolabeling efficiency

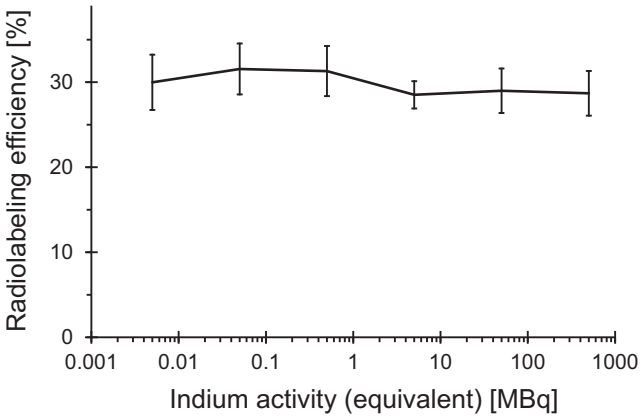

Figure s1. The labeling efficiency as function of the indium activity. The uncertainty bars correspond to standard deviations determined for three separate experiments. The samples were prepared in HEPES buffer pH 7.4 with 0.8 mM tropolone and 50 kBq ^{111}In activity (5 kBq for the lowest data point), containing 4.3 mg/mL PS-b-PEO micelles. Increasing amounts of non-radioactive indium was added equivalent to an ^{111}In activity up to 500 MBq.

Speciation chart of indium over the full pH range

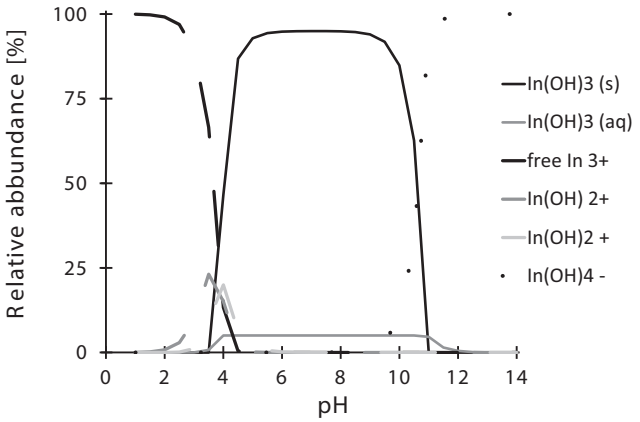

Figure s2. Speciation chart of indium at a concentration of 1 μM. The speciation chart is created with Cheaqs Next software version 2014.0.9.4. Input values for the concentration of both indium and chloride were $1x10^{-6}$ M, and for each pH the regarding H^+ input value was set as free activity, the concentration of all other elements was set to 0 M for this evaluation.

CHAPTER 3.3

Size and dose: factors influencing biodistribution and tumor uptake of polymeric micelles

In preparation for submission to EJNMMI Research

Santini C, Laan AC, Jennings L, de Jong M, Bernsen MR, Denkova AG

ABSTRACT

Background. Polystyrene block-poly(ethylene) oxide (PS-b-PEO) amphiphilic block copolymers can aggregate into stable supramolecular aggregates. Such aggregates can be labeled with tracking agents, including radionuclides, allowing for in vivo follow-up using nuclear imaging techniques, and can be easily varied in size without changing the block length of the forming block copolymer. The possibility to tune the particle size further confirmed the versatility and the potential of PS-b-PEO micelles as a drug carrier. The carrier size is often indicated as one of the most important properties, having a significant effect on biodistribution and tumor accumulation. In contrast, little is known on the effect of particle dose. More knowledge on this specific topic would help in determining the optimal delivery efficacy and may enable improvement of tumor uptake and avoiding toxicity in healthy tissues. In this study, we assessed the differences in tumor uptake after varying the size and applied dose of PS-b-PEO micelles. For the first time, ^{111}In radiolabeled PS-b-PEO micelles of two different sizes (106 nm and 170 nm in diameter) were evaluated at two different doses (1.7 mg/mL and 7 mg/mL) in mice bearing tumor xenografts. Using SPECT imaging and ex vivo studies, biodistribution of micelles were followed quantitatively over a period of 48 h.

Results. Images and biodistribution studies showed tumor uptake up to 4.15 % IA/g, as well as low off target accumulation, but relatively high uptake in the clearance organs (liver and spleen) for the four micellar samples. The levels of uptake in different tissues were significantly different for the four micellar formulations, they appeared highly dependent on size and dose.

Conclusions. PS-b-PEO micelles were found to accumulate in tumor tissue, they were found to have a biodistribution dependent on particle size and dose. These effects might be relevant for other nanoparticles as well.

Keywords: polymeric micelles, SPECT, size, dose, tumor uptake, uptake limit

BACKGROUND

The delivery of curative doses of therapeutics with tolerable toxicity in normal organs is still one of the biggest challenges in the treatment of solid tumors (1). In this respect, drug-encapsulating nanoparticles (nanocarriers) such as liposomes, dendrimers, or polymeric micelles, have shown better outcomes than free drugs, especially because of improved tumor uptake and reduced off target toxicity (2, 3).

Polystyrene block-poly(ethylene) oxide (PS-b-PEO polymers) are amphiphilic di-block copolymers that can form kinetically stable, nanosized micellar structures (*1-3*). Next to the easy and fast (radio)labeling method shown in previous studies (*1, 4*), the synthesis of PS-b-PEO polymer-based aggregates can be easily modulated to enable different morphologies (different size or shape) that might be of relevance for in vivo application, especially for the delivery of radionuclides to tumors (*3*).

Nanoparticle size is, among others, a main factor that can influence the level of accumulation in the tumor and the in vivo behavior, e.g. circulation time, clearance pathway, and bioavailability. Tumor accumulation of nanoparticles occurs as a result of a phenomenon known as the Enhanced Permeability and Retention (EPR) effect (*5*). In many tumors newly formed vessels are characterized by large fenestrae, lack of lymphatic drainage and irregular blood flow (*6, 7*), which favor the enhanced extravasation of particles from the circulation to the tumor tissue and subsequent retention of nanosized structure in the size range of ~50 to 500 nm (*8*). While nanoparticles below 50 nm show deep penetration in tissues and in tumors, compared to larger particles they also show faster washout and poor persistence in tissues (*9*).

The size of particles is one of the parameters determining not only the clearance pathway, but also the circulation time and the efficacy of accumulation in the tumor. Nanoparticles, because of their nanometric-size, often undergo limited excretion via the kidney as they exceed the renal filtration threshold; they are preferentially cleared via other pathways, i.e. via liver and spleen (*10*). These organs also show size-depended clearance patterns; particles above 50 nm up to ~100-150 nm are preferentially cleared from the circulation by the liver, while particles above ~180-200 nm are generally retained at a high level in the spleen (*10, 11*).

In a previous study, we generated PS-b-PEO micelles of 180 nm in diameter to develop and evaluate a facile method for radiolabeling of PS-b-PEO micelles. Following in vivo injection of these radiolabeled micelles in healthy mice, we observed preferential accumulation of radioactivity in the spleen and (at a lower level) in the liver (*1, 3*). This pattern of accumulation was the result of normal clearance pathways of nanosized particles, and influenced in vivo application of nanoparticles in two ways. On the one hand liver and spleen toxicity as a result of accumulation of carrier or carrier's payload might occur; the availability of nanoparticles

for target (tumor) accumulation is dependent on clearance; fast clearance might reduce the availability for target accumulation. Since these effects are strongly size-dependent, changing the size outside the liver and spleen accumulation range, can be a solution to reduce the accumulation in clearance organs, reduce the potential toxicity and improve the bioavailability for tumor accumulation (*10, 12*). While several studies have shown the importance of the size of the nanoparticle for in vivo applications, the role of the injection dose has been poorly investigated and has never been related to the size (*13*).

The dose of encapsulating nanoparticles directly determines the amount of the payload (specifically drugs) and plays a significant role in the delivery of drugs to the tumor. However, in contrast to expectations, previous studies indicated that injection of higher doses of nanocarrier (and drug) did not always result in higher accumulation in tumor tissue and better curative outcomes (*14*). These results indicated that other parameters also play a role in the biodistribution and tumor delivery efficacy of nanoparticles. In this study, we investigated the potential of PS-b-PEO micelles to target tumor tissue in a human tumor xenograft model in mice. We synthesized PS-b-PEO micelles of two different sizes, large micelles (LM, around 170 nm), and small micelles (SM, around 100 nm) to study how in vivo biodistribution was influenced by the size of the nanoparticles. We also studied the effect of PS-b-PEO particle dose on biodistribution and tumor uptake. We used a dose, matching that used in a previous study (*1*) and compared it to a four times lower injection dose.

MATERIALS AND METHODS

Chemicals

The block copolymer PS-b-PEO with a Mn (number-average molar mass) of 9500-b-18000 g/mol was purchased from Polymer Source (Quebec, Canada). The block copolymer was near monodisperse with an Mw/Mn ratio (Mw is the weight-average molar mass) of 1.09. Indium chloride, Sephadex G-25 and Sepharose 4B size exclusion chromatography resins, 4-(2-hydroxyethyl)-1-piperazine ethanesulfonic acid (HEPES) were purchased from Sigma Aldrich; tropolone was purchased from Merck. Ultrapure water was prepared with the in-house Milli-Q system (Merck Millipore). $^{111}InCl_3$ was obtained as solution in 10 mM hydrochloric acid from Mallinckrodt Pharmaceuticals (Petten, The Netherlands).

Synthesis, labeling and quality control of micelles

Synthesis, radiolabeling and purification of the two different micellar sizes was performed as previously described (*1, 3*). Briefly, 100 µl of a polymer solution in chloroform was added to 2.3 ml of HEPES buffer pH 7.4, containing the lipophilic ligand tropolone (0.8 mM) and $^{111}InCl_3$. The concentration of polymer solution was adjusted to obtain the required final micelle concentration: 1.25 mg/mL for in vitro stability test; 7 and 1.7 mg/mL for the in vivo study at high and low micellar concentration, respectively. For in vitro evaluation 50 kBq of $^{111}InCl_3$ solution was added to the sample. For in vivo studies 154 MBq of $^{111}InCl_3$ solution was added to each of the four samples, namely: large micelles at high dose (LMH), large micelles at low dose (LML), small micelles at high dose (SMH) and small micelles at low dose (SML). The solutions were then emulsified using a glass stirrer until all chloroform had evaporated. The two different micellar sizes were obtained by manipulating the speed of chloroform evaporation: the duration for complete evaporation was approximately 2 h (fast evaporation) for LM, and approximately 20 h (slow evaporation) for SM. The characterization of LM and SM was assessed by dynamic light scattering (DLS) and transmission electron microscopy (TEM) following the procedure previously described (*1*) (Figure 1).

In vitro stability tests

The retention of ^{111}In in labeled micelles was assessed in PBS and in mouse serum, following the previously described procedure (*1*). Briefly, 3 mL of the radiolabeled micelles (LM and SM) were mixed with an equal volume of PBS or serum. Both samples were placed in an incubator at 37 °C, and then analyzed after 24 and 48 h. The micelles in the serum samples were separated from the released ^{111}In using a Sepharose 4B gel SEC column (1 cm diameter and a length of 30 ± 1 cm), using 10 mM HEPES buffer pH 7.4 as eluent. For the same procedure, the micelles in PBS were purified with a Sephadex G-25 SEC column having the same dimensions as in the serum studies and using 10 mM HCl as eluent. The retention of radiolabel for the two different micellar sizes was calculated by measuring emitted radiation with a gamma counter (Wallac, 1480 Wizard 3"; PerkinElmer, Groningen, The Netherlands).

Tumor and animal model

The human small cell lung cancer cell line H69 xenografted in nude mice (ECACC, Salisbury, UK) was chosen as tumor model, because of the high tumor yield and fast growth in mice. This model is also known to develop tumors with aberrant vascularization with enhanced EPR effect (*15*). The cells were cultured under standard conditions in Gibco's RPMI

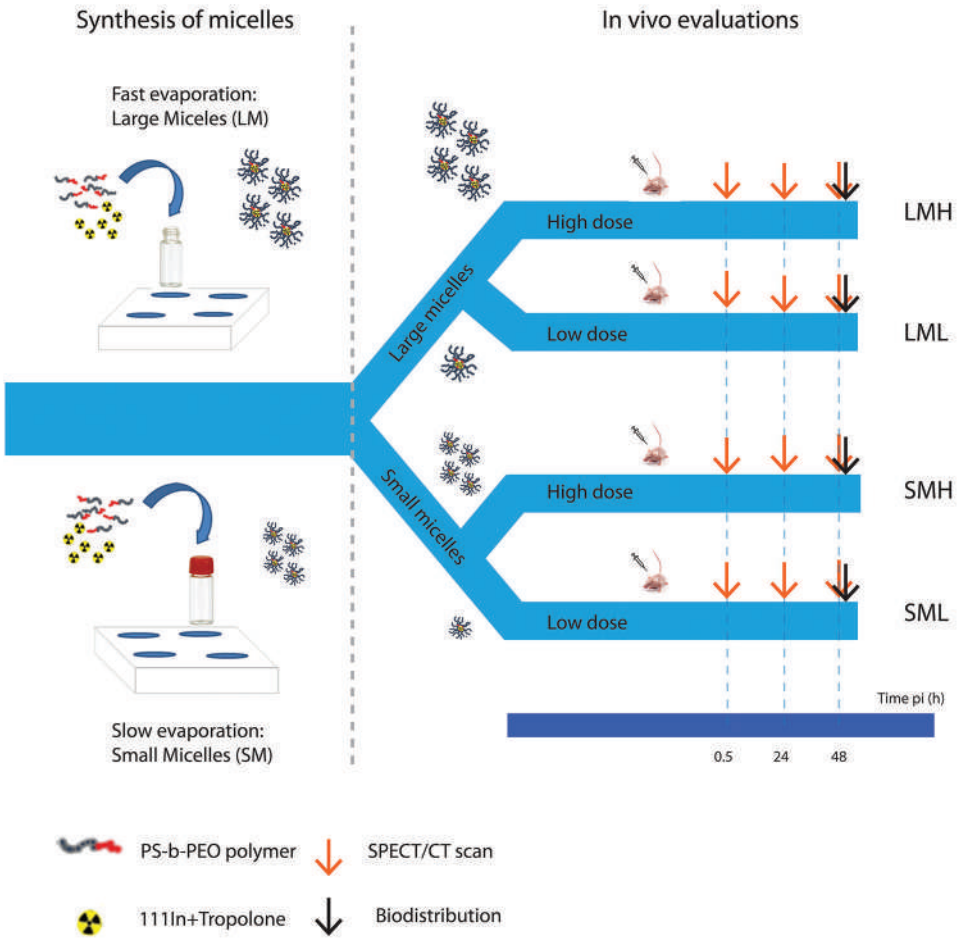

Figure. 1. Experimental overview. On the left: synthesis of PS-b-PEO micelles of different sizes. On the right: overview of in vivo evaluation, experimental groups and image acquisition schedule. LMH: large micelles, high dose; LML: large micelles, low dose; SMH: small micelles high dose; SML: small micelles, low dose.

medium (Invitrogen Corp., Breda, The Netherlands) supplemented with 10% v/v fetal bovine serum and 1% v/v penicillin/streptomycin. Cells were suspended in a 2:1 v/v Seligmann's buffered salt solution (SBSS) medium and Matrigel (BD Biosciences, Mississauga, Canada) at a concentration of $25.7*10^6$ cell/mL and inoculated subcutaneously in 20 young adult male Balb/c-nu mice (Janvier, France) (100 µL/mouse, ~$2.6*10^6$ cell/mouse). Tumor growth was monitored and measured with a caliper ruler three times/week. All animal experiments were performed in accordance with Dutch animal welfare regulations and approved by the local, ethics committee.

Table 1. Summary of dose injected for each formulation

Group	Injected dose [mg/ml]	Injected activity/mouse (mean ± sd) [MBq]
LMH	7 mg/mL (1.4 mg/mouse)	8.7 ± 0.37
SMH	7 mg/mL (1.4 mg/mouse)	6.38 ± 0.21
LML	1.7 mg/mL (0.34 mg/mouse)	2.34 ± 0.41
SML	1.7 mg/mL (0.34 mg/mouse)	4.24 ± 0.12

LMH: large micelles at high dose; LML: large micelles at low dose; SMH: small micelles at high dose; SML: small micelles at low dose. sd: standard deviation

SPECT/CT imaging and signal quantification

When the average tumor volume reached 300 mm^3, mice were randomly subdivided in four groups of five animals each, one for each of the four different micellar combinations. Mice received an injection of 200 µL of selected sample in the tail vein. Averages of radioactivity injected in each group are summarized in Table 1. After injection of radiolabeled nanoparticle, three out of five mice per group were randomly selected and subjected to nuclear imaging by single photon emission computed tomography combined with computed tomography (SPECT/CT). The nuclear images were acquired using the U-SPECT-II system (MiLabs B.V., Utrecht, The Netherlands) equipped with the new ultra-high-sensitivity collimator Mouse 2.0, having 54 conical pinholes of 2.0 mm diameter (*16*). The U-SPECT system has a heating system to prevent hypothermia of the animals during the scan. During scanning, mice were anesthetized with a gas mixture of isoflurane (Pharmachemie, Haarlem, The Netherlands) (4% induction, 2% maintenance) and oxygen. Mice were subjected to static SPECT/CT at different time points: 0.5 h post injection (pi), 24 h pi and 48 h pi (Figure 1).

Acquisition time was approximately 35 minutes (40-42 positions, 52 sec/position); CT scan was approximately 3 minutes (240 projections, 500 ms exposure time, 55 kVp tube voltage).

CT images were reconstructed using a filtered back projection (FBP) algorithm; SPECT images were reconstructed using the pixel-based ordered subsets expectation maximization (POSEM) algorithm with 30 iterations and 4 subsets (*17*). Both photo peaks of ^{111}In were used (171 and 245 keV). SPECT was registered to CT, corrected for scatter using the triple energy window method and for attenuation using the CT (*18*). All images shown were corrected for decay of ^{111}In, and scaled based on the image showing the highest radioactivity concentration.

Biodistribution studies

After 48 h pi all mice were euthanized by cervical dislocation; as a measure for biodistribution of the labelled micelles, the level of radioactivity present in blood and selected organs was measured. Samples of the collected blood and organs were weighed and the gamma radiation emitted from these samples was measured with a gamma counter. For the selected tissue samples the uptake of micelles was calculated as the percentage of injected activity measured per gram of tissue (% IA/g). Hereby assuming that measured radioactivity is a measure for the presence of radiolabeled micelles.

Ex vivo autoradiography

Autoradiography studies were conducted as previously described (*19*). In short, tumors were stored at -80°C for two weeks; then tissues were sliced into 15 μm thick sections and mounted on glass slides for autoradiography analyses. The slides were placed in a sensitive phosphor-imaging screen (PerkinElmer). The read out was performed using the Cyclone Storage Phosphor System (Packard) and images were processed with Optiquant (Software version 5.0, Perkin Elmer).

Software and statistical analyses of in vivo/ex vivo data

All data collected were processed with Prism version 6 (GraphPad Software, La Jolla, California, USA). Differences in the level of uptake of radioactivity of the different formulations were determined for each collected organ/tissue (biodistribution assay) using a One-Way Anova test ($p<0.05$ considered as statistically significant) and further post-hoc analyses using Bonferroni correction where appropriate ($p<0.01$ considered as statistically significant).

RESULTS

Synthesis and in vitro characterization of the micellar formulations

Using a one-step synthesis and labeling procedure, we successfully generated radiolabeled micelles of two sizes. The hydrodynamic diameter of the micelles measured via DLS was 170 ± 8 nm for LM and 106 ± 7 nm for SM; TEM analysis showed diameters of the polystyrene (PS) core to be between 31 and 37 nm for SM and between 40 nm and to 65 nm for LM (Figure 2A-B).

The radiolabeling yield for LM was 32.7 ± 0.7% and for SM it was 11.3 ± 0.3%. The retention of ^{111}In-tropolone in both PBS and serum remained stable over time, being always above 85% up to at least after 48 h exposure (Figure 2C-D).

Imaging studies: SPECT/CT and tumor autoradiography

Following injection of LM or SM, the SPECT/CT images showed already at the early time points an elevated signal in the area of the mice corresponding to the heart, major arteries, liver and spleen (Figure 3-4, SPECT/CT images). At later time points (24 h and 48 h pi) the radioactivity in the heart and major arteries, representative for radioactivity in the circulation, was not detectable anymore in the scan. The area corresponding to liver and spleen showed high signal up to at least 48 h pi. Radioactivity in the area of the tumor could not be detected by SPECT/CT. Radioactivity in the tumor was detectable through autoradiography analyses in all four samples. In the tumor rim more radioactivity was observed than in the tumor center (Figure 3-4, Autoradiography).

Biodistribution studies

An overview of biodistribution results obtained at 48 h pi is shown Table 2. The levels of radioactivity reached in selected organs and tumor are represented in different graphs in Figure 5. For all healthy organs and tumor, with exception of liver and spleen, we recognized a specific pattern in uptake values after low dose and high dose: with LM values decreased or remained stable with high dose, whereas for SM values increased at higher dose. The increase in uptake observed for SM when comparing low and high dose was statistically significant

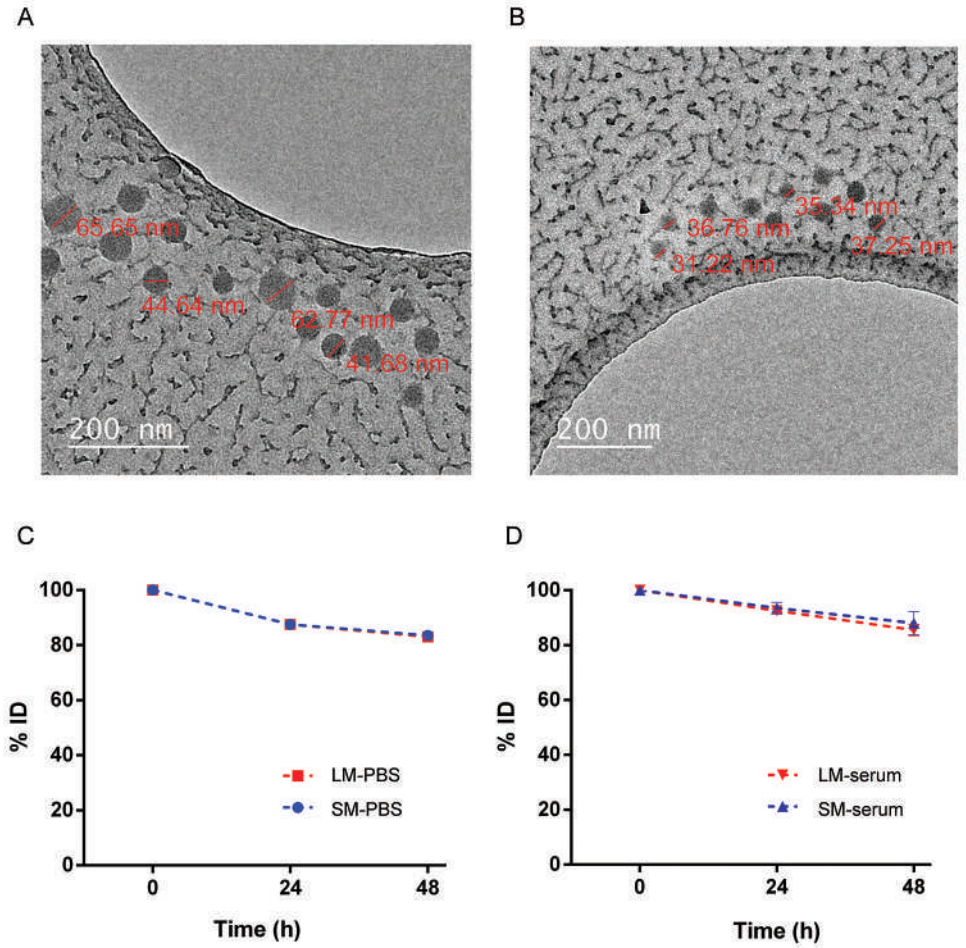

Figure 2. In vitro characterization of PS-b-PEO micelles. TEM images of LM (A) and SM (B); stability over time in PBS (C) and serum (D). LM: large micelle; SM: small micelles.

($p<0.01$) for most organs, including kidney, lungs, muscle and tumor. For LM, the increase of the injected dose from low to high resulted in significantly different values ($p<0.01$) only for muscle and colon, while for all other organs the values showed no significant difference ($p>0.01$).

In contrast to the pattern observed in the majority of off target tissues, in the spleen we observed a different trend: the values of radioactivity reached in the spleen by LM (blue lines) increased significantly ($p<0.01$) going from low to high dose. In contrast, for the SM (red line) the values remained similar; there was no significant difference ($p>0.01$) between the values measured at low dose and high dose (Figure 5, Spleen).

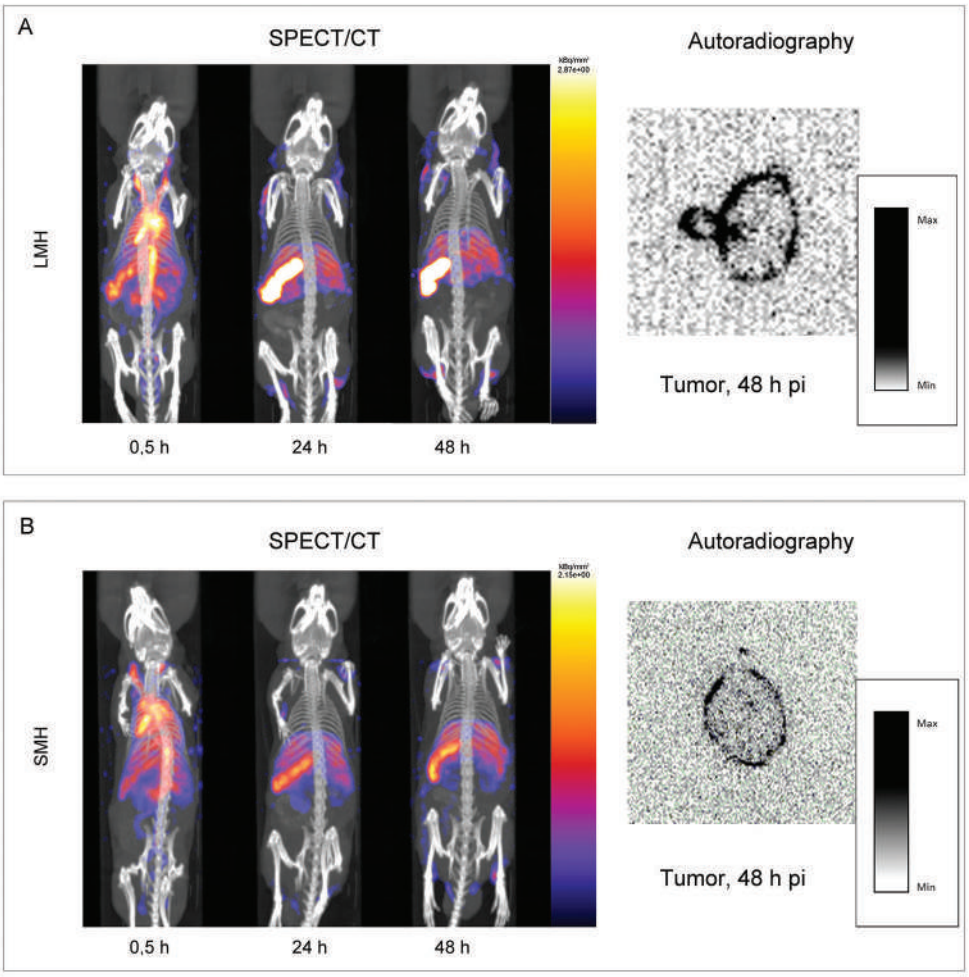

Figure 3. Biodistribution of ^{111}In-labeled micelles in tumor-bearing mice as assessed by SPECT/CT imaging and tumor autoradiography. A) Whole body SPECT/CT maximum intensity projection images (left panel) of tumor-bearing mice taken at various time points after injection with ^{111}In-labeled large micelles at a dose of 7 mg/mL (~8.7 MBq/mouse). On the right: autoradiogram of a tumor section, resected at 48 h pi. B) Whole body SPECT/CT maximum intensity projection (left panel) of tumor bearing mice take at various time point after the injection with ^{111}In-labeled large micelle at the dose of 7 mg/mL (~6.3 MBq/mouse). On the right: autoradiogram of a tumor section, resected at 48 h pi. LMH: large micelles, high dose; SMH: small micelles high dose; pi: post injection: min: minimum; max: maximum.

Liver presented another pattern: the uptake values of radioactivity measured in the liver remained similar ($p>0.01$) when the LM and SM were applied at low or high dose (Figure 5, Liver). However, we observed that the level or radioactivity measured in the liver after injection of SM was higher compared to that of LM (Figure 5, Liver).

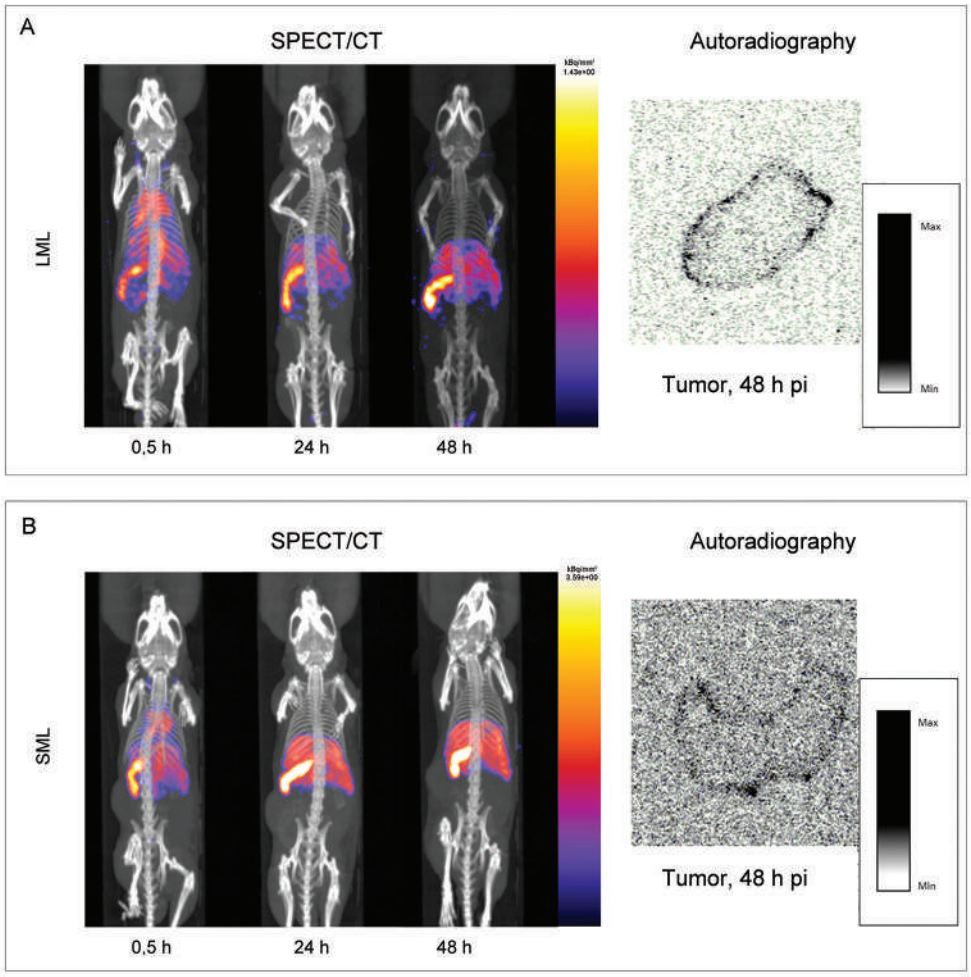

Figure 4. Biodistribution of ^{111}In-labeled micelles in tumor-bearing mice as assessed by SPECT/CT imaging and tumor autoradiography. A) Whole body SPECT/CT maximum intensity projection images (left panel) of tumor-bearing mice taken at various time points after injection with ^{111}In-labeled small micelles at a dose of 1.7 mg/mL (~2.3 MBq/mouse). On the right: autoradiogram of a tumor section, resected at 48 h pi. B) Whole body SPECT/CT maximum intensity projection (left panel) of tumor bearing mice take at various time point after the injection with ^{111}In-labeled large micelle at the dose of 1.7 mg/mL (~4.2 MBq/mouse). On the right: autoradiogram of a tumor section, resected at 48 h pi. LMH: large micelles, high dose; SMH: small micelles high dose; pi: post injection: min: minimum; max: maximum.

By comparing the differences in the uptake due to the variation in micellar size, we obsered that the effect of size is most prominent at the higher injection dose. Statistically higher uptake values ($p<0.01$) were found for SM compared to LM in caecum, kidney, muscle, colon, and tumor. Significant difference ($p<0.01$) in uptake at high dose was also found in the spleen, but here LM showed higher uptake values than SM (Figure 5).

At low dose, tatistical differences ($p>0.01$) in the uptake were found between LM and SM, for liver, heart and tumor, with LM showing higher uptake (Figure 5).

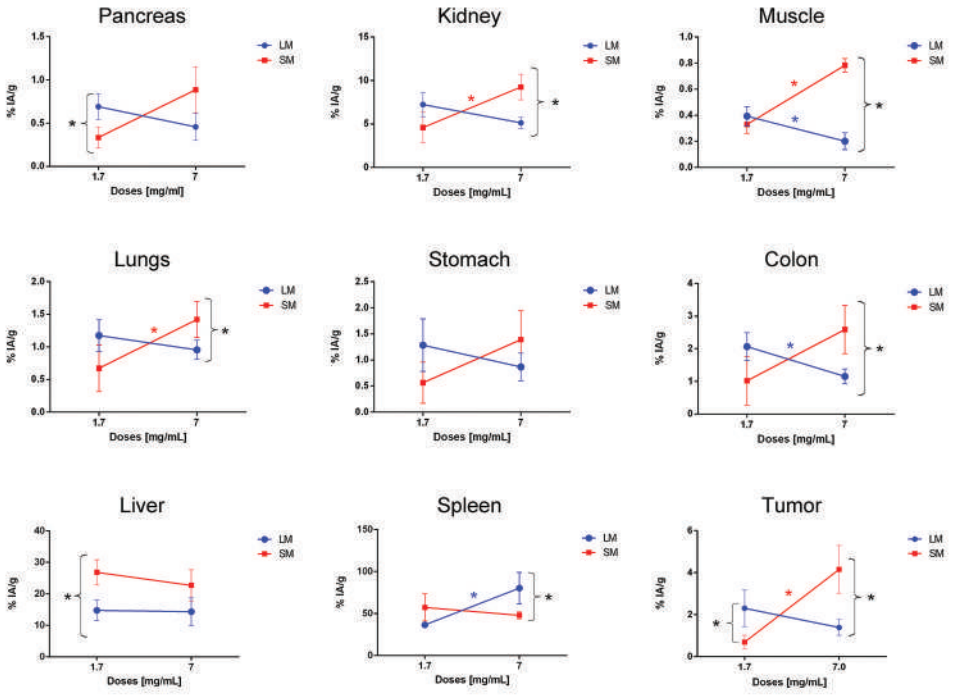

Figure 5. Biodistribution of radioactivity 48 h pi in selected organs and tumor after the injection of LMH (n=5), LML (n=5), SMH (n=5) and SML (n=5) in tumor bearing mice. Dots represent % IA/g expressed as mean ± standard deviation. Statistical significance in uptake between LM and SM, when applied at the same dose: * (black) significant difference $p<0.01$ for LM vs SM applied at the same dose; * (red): significant difference ($p<0.01$) in the uptake of SM between low and high dose; * (blue): significant difference ($p<0.01$) in the uptake of LM between low and high dose; LMH: large micelles, high dose; LML: large micelles, low dose; SMH: small micelles high dose; SML: small micelles, low dose; pi: post injection; IA: injected activity.

Table 2. Biodistribution of the four combinations expressed in % IA/g, 48 h pi.

	LMH		LML		SMH		SML	
% IA/g	**Mean**	**sd**	**Mean**	**sd**	**Mean**	**sd**	**Mean**	**sd**
Caecum	1.37	0.24	2.33	0.57	2.68	0.21	1.38	0.76
Liver	14.33	3.96	14.78	2.91	22.72	4.46	26.83	3.45
Kidney	5.13	0.54	7.23	1.20	9.24	1.31	4.59	1.57
Lungs	0.95	0.13	1.17	0.21	1.38	0.18	0.67	0.32
Muscle	0.20	0.06	0.39	0.06	0.78	0.05	0.33	0.06
Stomach	0.87	0.23	1.48	0.23	1.39	0.48	0.56	0.35
Colon	1.39	0.50	2.07	0.37	2.59	0.66	1.02	0.66
Rectum	0.83	0.30	1.36	0.18	1.73	0.37	0.77	0.46
Pancreas	0.46	0.13	0.69	0.13	0.84	0.25	0.33	0.11
Heart	0.86	0.12	1.11	0.08	1.17	0.20	0.66	0.15
Skin	8.33	4.22	6.83	2.10	8.63	0.40	2.96	1.69
Bone	1.00	0.17	1.77	0.88	2.22	0.42	1.42	0.69
Spleen	80.28	16.20	36.57	1.26	47.90	3.62	57.36	14.06
Tumor	1.22	0.45	1.95	0.36	4.15	0.99	0.69	0.29

LMH: large micelles at high dose; LML: large micelles at low dose; SMH: small micelles at high dose; SML: small micelles at low dose; sd: standard deviation.

Discussion

This study represents the first preclinical evaluation of radiolabelled PS-b-PEO micelles in tumor bearing mice, we investigated their biodistribution related to both particle size and applied dose.

The micelles we used in our evaluation had a diameter of ˜100 nm (SM) and 180 nm (LM). These sizes are within the upper size-limit range for retention of particles in the liver and in the preferential size range of uptake in the spleen (*10, 20*).

In the liver, we found higher levels of SM compared to those of LM, an effect that reflects the capacity of the liver to trap particles of ˜100 nm with higher efficiency compared to those of ˜200 nm (*10*). For both LM and SM, the increase of the dose resulted in limited effect on

liver uptake as we did not see an increase in the levels of radioactivity when SM and LM were administered at low or high dose.

In the spleen and in the liver we detected differences in uptake for different micellar sizes, whereas in the spleen values also differed with variations in the dose. LM showed higher uptake in the spleen (*1*), also increasing with higher dose. In contrast with the results of LM, however, the uptake of SM in the spleen did not increase at the higher dose.

In contrast with the uptake of LM and SM in liver and spleen, other organs and tumor did not show significant values for LM and SM at low or high dose. This might be due to different penetration capacities of the two micellar sizes. Different penetration capacities due to the size were visible only at high dose. Probably at the low dose other aspects play a more important role. Further studies, focusing in such aspects are needed to clarify the effect of the clearance organs at low dose.

Another interesting aspect that we observed in our study was the limited effect on accumulation of LM at the higher dose. High uptake in the spleen might strongly influence the remaining amount of circulating LM, thus reducing the uptake in other tissues. Moreover, because of their bigger size, LM show a lower penetration in tissues compared to SM, which further hampers accumulation. Our results indicate that a critical design and evaluation of nanoparticles as carriers is therefore warranted. The uptake value in the tumor is of course an important parameter to evaluate, but other factors may also be of importance and should be considered when selecting nanocarriers as well. The chemical and physical properties of nanoparticles, such as the synthesis time or the loading yield, as well as the uptake in healthy tissues, can strongly steer the selection process of nanoparticles.

In our study, among all formulations tested, SMH showed the highest tumor uptake. However, the uptake in normal tissue was also very high, resulting in a low tumor/tissue ratio. A dose reduction on the other hand, resulted in lower uptake in normal organs (except for liver and spleen), but had a dramatic effect on tumor uptake as well. These aspects, together with the low labeling yield and the long synthesis time, do not support the use of SM for in vivo use.

In contrast, LM had lower levels of tumor uptake than SM, but they presented higher tumor/tissue ratios. Moreover, LM showed higher labeling yields compared to SM and shorter synthesis time, suggesting LM to be more efficient as carrier for tumor delivery.

Low levels of tumor uptake of nanoparticles are often seen, but it has been shown that this limitation can be overcome by temporarily improvement of tumor vasculature. The method is known as "intratumoral vascular normalization" and have been shown to be effective in improving the accumulation of nanoparticles similar to PS-b-PEO micelles in the tumor (*20, 22*).

CONCLUSIONS

In conclusion, we have shown that PS-b-PEO micelles provide a versatile platform to generate micelles of different size. For the sizes tested, PS-b-PEO micelles could accumulate in tumors and showed to have suitable properties as a drug carrier. Both tumor and regular tissue uptake, however, was dependent on particle size and applied dose. The effects of both parameters should therefore be taken into account when evaluating carriers for drug delivery in general.

List of abbreviations

CT: computed tomography; DLS: dynamic light scattering; EPR: enhanced permeability and retention effect; LM: large micelles; LMH: large micelles high dose; LML: large micelles low dose; PEO: poly(ethylene oxyde); PS: polystyrene; SM: small micelles; SMH: small micelles high dose; SML: small micelles low dose; TEM: transmission electron microscopy.

Competing interests

The authors have no competing interests.

Author's contribution

CS performed the in vivo and ex vivo data acquisitions and data analysis and wrote the manuscript. AL performed the in vitro evaluations, carried out the physical characterization and the production of radiolabeled micelles; LJ participated in the experimental design; AD, MdJ and MB contributed to the design of the study and writing and critical editing of the manuscript. All authors approved the final manuscript.

Acknowledgment

This work was performed using imaging equipment in the Applied Molecular Imaging at Erasmus MC (AMIE) facility. The research leading to these results has received funding from

the People Programme (Marie Curie Actions) of the European Union's Seventh Framework Programme (FP7/2007-2013) under REA grant agreement no. PITN-GA-2012-317019 'TRACE'n TREAT. The authors thank all members of the consortium under the Marie Curie Action, "Trace'n Treat", for their collaboration. Particular thanks go to Jan de Swart, Mark Konijnenberg and Ho Sze Chan for their technical support and fruitful discussions.

REFERENCES

1. Laan AC, Santini C, Jennings L, de Jong M, Bernsen MR, Denkova AG. Radiolabeling polymeric micelles for in vivo evaluation: a novel, fast, and facile method. *EJNMMI Res.* 2016;6:016-0167.
2. Yu K, Eisenberg A. Multiple Morphologies in Aqueous Solutions of Aggregates of Polystyrene-block-poly(ethylene oxide) Diblock Copolymers. *Macromolecules.* 1996;29:6359-6361.
3. Jennings L, Ivashchenko O, Marsman IJ, et al. In vivo biodistribution of stable spherical and filamentous micelles probed by high-sensitivity SPECT. *Biomater Sci.* 2016;10:10.
4. Miyata K, Christie RJ, Kataoka K. Polymeric micelles for nano-scale drug delivery. *Reactive and Functional Polymers.* 2011;71:227-234.
5. Maeda H. Macromolecular therapeutics in cancer treatment: the EPR effect and beyond. *J Control Release.* 2012;164:138-144.
6. Matsumura Y, Maeda H. A new concept for macromolecular therapeutics in cancer chemotherapy: mechanism of tumoritropic accumulation of proteins and the antitumor agent smancs. *Cancer Res.* 1986;46:6387-6392.
7. Folkman J, Hanahan D. Switch to the angiogenic phenotype during tumorigenesis. *Princess Takamatsu Symp.* 1991;22:339-347.
8. Blanco E, Shen H, Ferrari M. Principles of nanoparticle design for overcoming biological barriers to drug delivery. *Nat Biotech.* 2015;33:941-951.
9. Dreher MR, Liu W, Michelich CR, Dewhirst MW, Yuan F, Chilkoti A. Tumor vascular permeability, accumulation, and penetration of macromolecular drug carriers. *J Natl Cancer Inst.* 2006;98:335-344.
10. Bertrand N, Leroux JC. The journey of a drug-carrier in the body: an anatomo-physiological perspective. *J Control Release.* 2012;161:152-163.
11. Bae YH, Park K. Targeted drug delivery to tumors: myths, reality and possibility. *J Control Release.* 2011;153:198-205.
12. Moghimi SM, Hunter AC, Murray JC. Long-circulating and target-specific nanoparticles: theory to practice. *Pharmacol Rev.* 2001;53:283-318.
13. Panagi Z, Beletsi A, Evangelatos G, Livaniou E, Ithakissios DS, Avgoustakis K. Effect of dose on the biodistribution and pharmacokinetics of PLGA and PLGA-mPEG nanoparticles. *Int J Pharm.* 2001;221:143-152.
14. Alibolandi M, Sadeghi F, Abnous K, Atyabi F, Ramezani M, Hadizadeh F. The chemotherapeutic potential of doxorubicin-loaded PEG-b-PLGA nanopolymersomes in mouse breast cancer model. *Eur J Pharm Biopharm.* 2015;94:521-531.
15. Haeck J, Bol K, Bison S, et al. Optimized time-resolved imaging of contrast kinetics (TRICKS) in dynamic contrast-enhanced MRI after peptide receptor radionuclide therapy in small animal tumor models. *Contrast Media Mol Imaging.* 2015;10:413-420.
16. Ivashchenko O, van der Have F, Goorden MC, Ramakers RM, Beekman FJ. Ultra-high-sensitivity submillimeter mouse SPECT. *J Nucl Med.* 2015;56:470-475.
17. Branderhorst W, Vastenhouw B, Beekman FJ. Pixel-based subsets for rapid multi-pinhole SPECT reconstruction. *Phys Med Biol.* 2010;55:2023-2034.

18. Ogawa K, Harata Y, Ichihara T, Kubo A, Hashimoto S. A practical method for position-dependent Compton-scatter correction in single photon emission CT. *IEEE Trans Med Imaging.* 1991;10:408-412.
19. Melis M, Forrer F, Capello A, et al. Up-regulation of somatostatin receptor density on rat CA20948 tumors escaped from low dose [177Lu-DOTA0,Tyr3]octreotate therapy. *Q J Nucl Med Mol Imaging.* 2007;51:324-333.
20. Ernsting MJ, Murakami M, Roy A, Li SD. Factors controlling the pharmacokinetics, biodistribution and intratumoral penetration of nanoparticles. *J Control Release.* 2013;172:782-794.
21. Huang Y, Goel S, Duda DG, Fukumura D, Jain RK. Vascular Normalization as an Emerging Strategy to Enhance Cancer Immunotherapy. *Cancer Research.* 2013;73:2943-2948.
22. Al-Abd AM, Aljehani ZK, Gazzaz RW, et al. Pharmacokinetic strategies to improve drug penetration and entrapment within solid tumors. *J Control Release.* 2015;219:269-277.
23. Li SD, Huang L. Pharmacokinetics and biodistribution of nanoparticles. *Mol Pharm.* 2008;5:496-504.

EPILOGUE

Summary, Concluding remarks

Samenvatting

Curriculum Vitae

List of Pubblications

PhD Portfolio

Acknowledgements

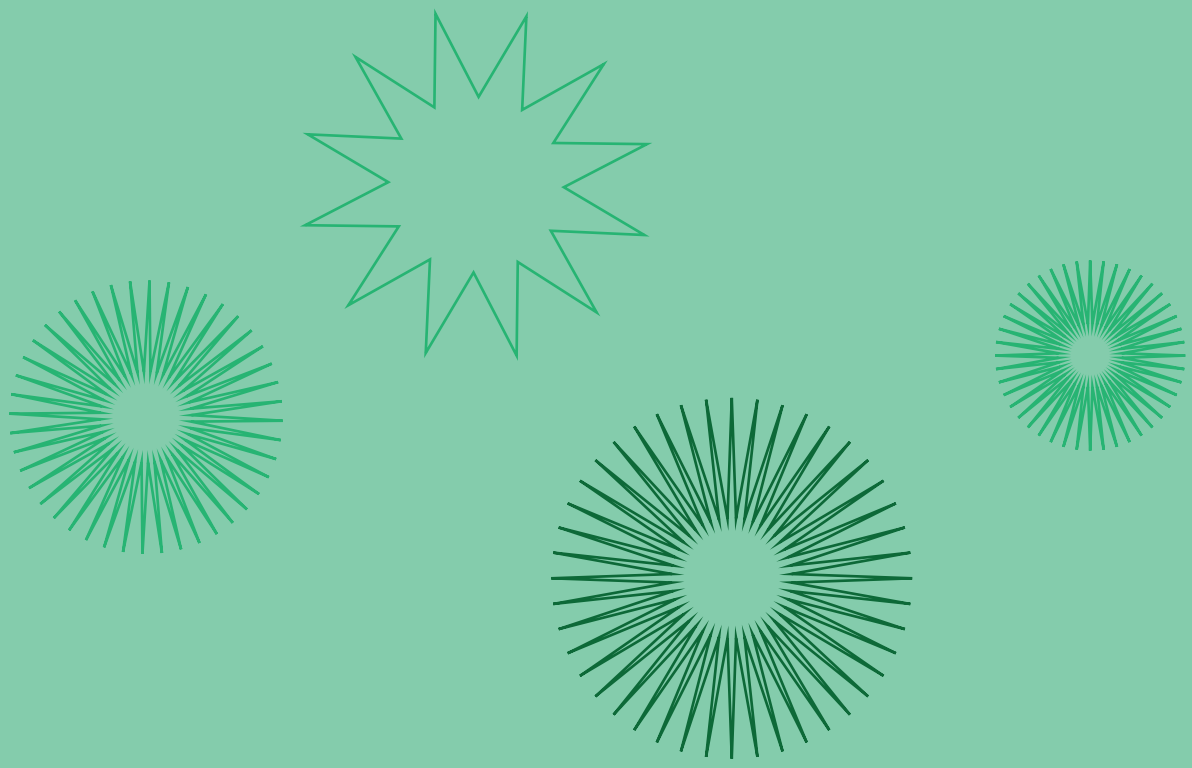

SUMMARY, CONCLUDING REMARKS

Cancer is an important cause of death worldwide, with an increasing number of new cases every year. Different approaches have been developed for detection and treatment of the disease.

Nuclear medicine techniques can be applied for both imaging and therapy, they can also be employed to improve other cancer therapy methods (i.e. nuclear imaging-guided surgery). For delivery of radioactivity to tumor cells often radiolabeling of specific molecules, acting as carriers for targeting to the tumor, is employed.

The carriers presented in this thesis can be subdivided into two main categories: 1) small peptide-based carriers that specifically accumulate in tumor tissue via interaction with tumor receptors. Their main clearance pathway is via the kidneys; 2) nanosized carriers (molecular or supramolecular nanoparticles) that can aid in accumulation of radioactivity in the tumor via passive mechanisms. They can suffer from high uptake in liver and spleen .

The aim of our preclinical studies was to develop, further improve and evaluate carriers for delivery of radionuclides for tumor imaging and/or therapy at the tumor site.

Chapter 1 of this thesis provides an introduction to radioactivity and the two categories of carriers. We describe relevant aspects of biodistribution mechanisms involved in tumor accumulation and clearance pathways.

In **Chapter 2** we present two studies performed with two radiolabeled peptide-based carriers (i.e. somatostatin analogues) for imaging and therapy of neuroendocrine tumors (NETs).

Chapter 2.1 describes a preclinical evaluation study using the hybrid label (nuclear and optical), somatostatin analogue Cy5-^{111}In-DTPA-Tyr^3-octreotate in comparison to ^{111}In-DTPA-Tyr^3-octreotate. Nuclear imaging with radiolabeled somatostatin analogs is successfully applied in the clinic for tumor visualization, surgical planning and staging in patients with NETs. The integration of nuclear techniques with optical techniques may help to further improve imaging for intraoperative guidance. Hybrid molecules that consist of e.g. a DTPA chelator and Cy5 optical dye can be used to generate dual-labeled peptides (i.e. Cy5-^{111}In-DTPA-Tyr^3-octreotate) for multimodal molecular imaging applications. These bulky hybrid-imaging molecules however substantially reduced receptor affinity in in vitro studies. On the

other hand in vivo studies in a mouse model with Cy5-^{111}In-DTPA-Tyr^3-octreotate showed good nuclear and optical imaging potential with good tumor uptake. The results therefore indicated that Cy5-^{111}In-DTPA-Tyr^3-octreotate is a promising compound for image-guided resection of neuroendocrine tumors, allowing for combined visualization of lesions by Single Photon Emission Computed Tomography/Computed Tomography (SPECT/CT) (surgical planning, intraoperative guidance and treatment evaluation) and fluorescence imaging (intra-operative surgical guidance).

In **Chapter 2.2** we describe the effects of specific activity and treatment schedules on the therapeutic efficacy of ^{177}Lu-DOTA-Tyr^3-octreotate in tumor-bearing mice. For effective tumor treatment a high level of radiation should be delivered to the tumor, while normal organs should receive a non-toxic dose. Increasing the tumor/normal-organ ratio will therefore enhance the therapeutic window of this therapy. Increasing the specific activity of administered peptide was shown to improve the dose to the tumor and in general resulted in higher tumor/normal organ ratios compared to treatment with radiolabeled peptides with low specific activity. Fractionation of the dose can play a role as well in potential improvement of the therapeutic effects as dose fractionation did not affect anti-tumor responses, but can reduce the radiation effects of the dose delivered to different normal organs in mice.

Chapter 3 describes the in vivo behavior of two different nanostructures for tumor targeting: the Pluronic P94 block-copolymer and Polystyrene-poly(ethylene oxide (PS-b-PEO)-based supramolecular aggregates.

In **Chapter 3.1** we present the effects of different administration routes (either intravenous (IV) or intratumoral (IT)) of radiolabeled Pluronic P94 copolymer on tumor uptake/retention and biodistribution in vivo in a mouse tumor model. Pluronic P94 is a triblock copolymer that, as unimer, has shown tumor cell internalization in vitro and prolonged blood circulation in vivo, being promising for tumor drug delivery applications. IV injection of radiolabeled unimers, however, resulted in limited tumor uptake whereas IT administration of the radiolabeled unimers resulted in substantial radioactivity levels in tumor tissue. The minimal off-target tissue involvement and excellent radioactivity retention in the tumor after IT administration indicated the potential of Pluronic P94 copolymer as a carrier of radioactivity for tumor imaging and/or therapy.

In **Chapter 3.2** we report a new facile method for radiolabeling PS-b-PEO-based supramolecular aggregates with ^{111}In for SPECT. PS-b-PEO diblock copolymers are amphiphilic block copolymers that can aggregate into stable nanoparticles. During the aggregation process they can incorporate different agents, including radionuclides, with the advantage that chemical modification of the carrier (e.g. covalent attachment of a chelator) is not needed.

The in vivo evaluation of the nanoparticles via SPECT imaging showed long circulation in vivo in a mouse model, no acute toxicity and relatively low accumulation in the liver. These observations confirmed the potential of PS-b-PEO structures for delivery of imaging and/or therapeutic radionuclides to solid tumors.

Next to the ease of radiolabeling, PS-b-PEO supramolecular structures can be simply varied regarding size. Size is considered one of the main factors influencing biodistribution of nanoparticles and tumor delivery efficiency. Little is known however regarding the effects of different applied doses in in vivo applications; high doses may saturate uptake in different tissues. The study presented in **Chapter 3.3** is the first assessing the in vivo biodistribution and tumor uptake of PS-b-PEO supramulecular aggregates of two different sizes, applied at two different doses in a mouse model in vivo. Our result indicated PS-b-PEO aggregates to show a specific size-and-dose-dependent biodistribution profile, with a tendency of more desirable tumor-to-normal-tissue distribution patterns at lower doses and for smaller particles.

CONCLUDING REMARKS

In this thesis work, we designed and evaluated carriers from two categories, i.e. small, specific, receptor-targeting peptides and larger non-specific-targeting agents, including nano-sized particles (nanoparticles). Some main characteristics of these carrier types are listed in Table 1. The two categories show profound differences regarding their in vivo behavior in mice, including the mechanisms and level of accumulation in tumor cells, longevity in the circulation and clearance pathways. As a result, depending on the conditions (i.e. tumor type with or without a certain receptor), one of the two types of carries will be preferred over the other for delivery of imaging and/or therapeutic radionuclides. In tumors overexpressing specific receptors, targeting peptides will be the first choice; in tumors with low or no (known) receptor expression, a nanoparticle showing longer circulation time and passive targeting properties might be preferable.

Of the first category, we evaluated the potential of radiolabelled somatostatin analogues for two different approaches: intraoperative imaging and improved radionuclide therapy in a mouse model of neuroendocrine tumors (NETs).

Multimodal intraoperative or guided surgery is an emerging and promising field of interventional surgery. In our research, the affinity between receptor and peptide was employed to deliver a multimodal probe that can be used before and during surgery to guide and improve the resection of lesion(s) [1, 2]. In our study the “multimodal” part was a nuclear-and-optical

Table 1. Summary of properties of small targeting peptides versus non-targeting nanoparticles

	Targeting agents (peptides)	Non-targeting nanoparticles
Size	< 1 nm	> 50 nm
Main accumulation method in tumor tissues	Ligand-receptor interaction	EPR effect
Main clearance pathways	Kidney	Liver and Spleen
Potential of application	Tumors with elevated receptor expression	Tumor presenting good EPR effects
Level of accumulation in target tissues	Up to 30% ID/g	Up to 10% ID/g (in average 3-5% ID/g)
Main strengths	Target specific Low off target accumulation Rarely side effects are seen	No target needed, potentially effective in more tumor types Possibility to load with multiple agents at the same time with minimal effect on biological behavior
Main limitations	Native molecules vulnerable to degradation Effective in a restricted number of tumor types Potential radiation-induced toxicity to the kidneys and bone marrow Potential reduction of affinity for the receptor after modification (stabilization and labeling)	Low accumulation in the tumor Elevated and long lasting accumulation in liver and spleen

EPR: enhanced permeability and retention; ID; injected dose.

platform that was covalently bound to a somatostatin analogue [3]. The attachment of this bulky structure to the ligand resulted however in a significant reduction of receptor affinity. The results of the in vivo study in mice were nevertheless promising: despite the reduction of receptor affinity, the nuclear images obtained with the multimodality somatostatin analogue were comparable to those obtained with a radiolabelled somatostatin analogue. These results strongly support further research on the use of multimodality somatostatin analogues for imaging and for guided surgery, in comparison to radiolabeled counterparts. For the nuclear part different chelators (such as the DOTA) might be used for incorporation of different radionuclides, to open also the possibility of positron emission tomography (PET) -based nuclear imaging.

A major drawback of the novel multimodality somatostatin analogue was represented by the high uptake/retention in the kidney compared to the radiolabelled counterpart. Kidneys

are known to have relatively high uptake of radiolabelled somatostatin analogues [4-6], the elevated renal radioactivity can hide lesions that are close to kidneys and can damage kidneys due to a high radiation dose delivered (by therapeutic radionuclides) [3]. A significant reduction of renal uptake of these radiopeptides can be obtained using positively charged amino acids that counteract their reabsorption in the proximal tubules [7]. We assume our multimodal somatostatin analogues might benefit from a similar approach as well [3].

Radiolabeled somatostatin analogues have shown to be highly effective for radionuclide therapy of NETs; they can reduce tumor growth and improve quality of life of patients [8, 9]. On the other hand, complete regression of metastasized disease is still rare. The understanding of radiation effects in tumor lesions and healthy tissues can be an important factor to reduce normal tissue toxicity and also improve the therapeutic success. Changes in the administration schedules of therapeutic somatostatin analogues can increase the ratio between tumor versus normal organ radiation effects, with significant improvement of the therapeutic window. Increasing the specific activity and modification (e.g. fractionation of the dose) of the treatment plan can improve therapeutic responses. In our study we applied a tumor-response model that linked the absorbed dose to the observed tumor volume response over time. Our findings strongly underline the importance of a more personalized treatment planning based on physical and biological tumor characteristics.

Of the second category of carriers, polymeric molecular and supramolecular structures, we investigated accumulation in the tumor and biodistribution in preclinical models. Both Pluronics and PS-b-PEO supramolecular aggregates are structures that can be labeled with radionuclides [10, 11], showing long lasting stability in vivo. They can selectively and stably accumulate in tumors via a passive mechanism, the enhanced permeability and retention (EPR) effect [12, 13]. However, both Pluronic P94 and PS-b-PEO supramolecular aggregates presented relatively low tumor/normal tissue ratios, as tumor accumulation was generally below 5% of the injected dose and retention in liver and spleen was high [14]. With the aim to improve the tumor to tissue radioactivity ratio, we evaluated the effects of local (IT) versus IV injections. We showed the effect of systemic and local administrations on tumor and normal tissue accumulation/retention of the radiolabeled polymeric carrier Pluronic P94 (P94-^{111}In-DTPA) in its unimeric form. As previously shown, systemic administration resulted in limited uptake of radioactivity in the tumor and a substantial dose to liver and spleen. In contrast, local IT administration of the radiolabeled polymer substantially improved the dose to the tumor with minimal off-target tissue involvement. A control group injected intratumorally with ^{111}In-DTPA confirmed the need of the polymeric carrier for a long retention of radioactivity in the tumor. Pluronic P94 therefore presents promising potential for delivery of radioactivity in tumors when injected IT. This approach obviously presents limitations as it is not appropriate for targeting metastatic cancer, nevertheless it can be a valid method in specific cases where systemic application is not suitable. So, intratumoral injection of drugs (or drug-loaded carriers) is applied in the clinic in the treatment of brain cancers [15].

The low level of accumulation in the tumor can be caused by poor permeability, high internal pressure or impaired blood flow [16, 17]. Improvements in the delivery have been made by specific intervention at the level of the tumor, applying hyperthermia, or by normalization of tumor vasculature/blood flow [17, 18]. Poor accumulation of nanoparticles in tumors might also be caused by high uptake and retention in clearance organs. Reducing this high uptake that depletes nanoparticles from the circulation and therefore the delivery to the target, is crucial to improve the level of accumulation in the tumor. Sizes, shape, stiffness, structure of the outer part (i.e. the components that are in direct contact with the host environment) are morphological and structural aspects that have shown to significantly influence clearance of the nanoparticle from liver and spleen [13, 14].

We furthermore presented a method for the synthesis and facile radiolabeling of PS-b-PEO-based supramolecular aggregates and demonstrated their potential for in vivo application as carriers for delivery of radionuclides to target tissues. The aggregates showed long lasting circulation in mice and could be detected via nuclear imaging up to at least 24 h pi. Results encouraged further evaluation of the potential of PS-b-PEO-based supramolecular aggregates to deliver (radioactive) agents to tumors. Recent studies demonstrated that PS-b-PEO-based supramolecular aggregates could be tuned in size during their synthesis [13]. Size is considered one of the most important properties when dealing with delivery of nanoparticles. It affects the biodistribution including tumor targeting capabilities, but also determines clearance from the circulation and uptake in clearance organs. In contrast, little is known on the effects of the applied dose, high doses may lead to saturation of tissues and, as a consequence, influence the potential therapeutic efficacy and toxicity. We studied the effects of different sizes and applied doses on biodistribution and tumor uptake of PS-b-PEO base nanoparticles in mice bearing a tumor xenograft. Our results indicate that PS-b-PEO aggregates have a specific size-and-dose-dependent behavior. In terms of tumor uptake the smaller nanoparticles presented the best outcome at a higher dose, suggesting that reducing the size and increasing the dose might be beneficial to improve tumor uptake. On the other hand, elevated off-target accumulation of small particles was seen, especially at the higher dose, raising concerns regarding off target toxicity. The best performance was therefore obtained using the bigger particles at the lower dose, showing the second-best tumor uptake, but a considerably lower off target accumulation. Our results indicate that dose is as crucial as size for delivery of radioactivity to the tumor and the success of PS-b-PEO nanoparticles. Further studies should provide insight on the curative potential of these nanoparticles and the level of toxicity.

In general, the peptides performed better than the nanoparticles applied in our studies regarding tumor uptake and retention, as well as regarding tumor to normal organ ratios. Peptides, however, are only suitable for imaging and therapy of specific tumor types that overexpress a characterized targeting receptor. In other conditions, nanoparticles can be interesting devices for imaging and therapy of solid tumors. Our results demonstrated that Pluronic

polymers as well as supramolecular aggregates of PS-b-PEO can successfully be taken up in tumor tissue and encourage further studies to evaluate their potential as carriers of curative drugs.

REFERENCES

1. Lutje, S., et al., Targeted radionuclide and fluorescence dual-modality imaging of cancer: preclinical advances and clinical translation. Mol Imaging Biol, 2014. 16(6): p. 747-55.
2. Bunschoten, A., et al., Multimodal interventional molecular imaging of tumor margins and distant metastases by targeting alphavbeta3 integrin. Chembiochem, 2012. 13(7): p. 1039-45.
3. Santini, C., et al., Evaluation of a Fluorescent and Radiolabeled Hybrid Somatostatin Analog In Vitro and in Mice Bearing H69 Neuroendocrine Xenografts. J Nucl Med, 2016. 57(8): p. 1289-95.
4. Krenning, E.P., et al., Somatostatin receptor scintigraphy with indium-111-DTPA-D-Phe-1-octreotide in man: metabolism, dosimetry and comparison with iodine-123-Tyr-3-octreotide. J Nucl Med, 1992. 33(5): p. 652-8.
5. Melis, M., et al., Localisation and mechanism of renal retention of radiolabelled somatostatin analogues. Eur J Nucl Med Mol Imaging, 2005. 32(10): p. 1136-43.
6. Berne, R.M., B.M. Koeppen, and B.A. Stanton, Berne & Levy physiology2010, Philadelphia, PA: Mosby/Elsevier.
7. Valkema, R., et al., Phase I study of peptide receptor radionuclide therapy with [In-DTPA]octreotide: the Rotterdam experience. Semin Nucl Med, 2002. 32(2): p. 110-22.
8. Bodei, L., et al., Long-term tolerability of PRRT in 807 patients with neuroendocrine tumours: the value and limitations of clinical factors. Eur J Nucl Med Mol Imaging, 2015. 42(1): p. 5-19.
9. Kwekkeboom, D.J., et al., Treatment with the radiolabeled somatostatin analog [177 Lu-DOTA 0,Tyr3] octreotate: toxicity, efficacy, and survival. J Clin Oncol, 2008. 26(13): p. 2124-30.
10. Laan, A.C., et al., Radiolabeling polymeric micelles for in vivo evaluation: a novel, fast, and facile method. EJNMMI Res, 2016. 6(1): p. 016-0167.
11. Arranja, A., et al., Interactions of Pluronic nanocarriers with 2D and 3D cell cultures: Effects of PEO block length and aggregation state. J Control Release, 2016. 224: p. 126-35.
12. Arranja, A., et al., SPECT/CT Imaging of Pluronic Nanocarriers with Varying Poly(ethylene oxide) Block Length and Aggregation State. Mol Pharm, 2016. 13(3): p. 1158-65.
13. Jennings, L., et al., In vivo biodistribution of stable spherical and filamentous micelles probed by high-sensitivity SPECT. Biomater Sci, 2016. 10: p. 10.
14. Bertrand, N. and J.C. Leroux, The journey of a drug-carrier in the body: an anatomo-physiological perspective. J Control Release, 2012. 161(2): p. 152-63.
15. Cordier, D., et al., Targeted Radiolabeled Compounds in Glioma Therapy. Seminars in Nuclear Medicine, 2016. 46(3): p. 243-249.
16. Lammers, T., et al., Drug targeting to tumors: principles, pitfalls and (pre-) clinical progress. J Control Release, 2012. 161(2): p. 175-87.
17. Al-Abd, A.M., et al., Pharmacokinetic strategies to improve drug penetration and entrapment within solid tumors. J Control Release, 2015. 219: p. 269-77.
18. Khawar, I.A., J.H. Kim, and H.J. Kuh, Improving drug delivery to solid tumors: priming the tumor microenvironment. J Control Release, 2015. 201: p. 78-89.

SAMENVATTING

Kanker is wereldwijd een belangrijke doodsoorzaak; bovendien stijgt het aantal patiënten met kanker nog ieder jaar. Er wordt hard gewerkt aan betere methoden voor het opsporen en behandelen van deze ziekte.

Nucleair geneeskundige technieken kunnen toegepast worden voor beide toepassingen, zowel voor beeldvorming (imaging) als voor behandeling. Ze kunnen ook worden gebruikt om andere kankertherapiemethoden te verbeteren (bijv. chirurgische geleiding met behulp van nucleaire beeldvorming). Specifieke moleculen kunnen radioactief gelabeld worden, deze tracers kunnen fungeren als dragers van radioactiviteit naar bijvoorbeeld een receptor op de tumorcel. De tracers die in dit proefschrift worden gepresenteerd, kunnen onderverdeeld worden in twee hoofdcategorieën: 1) kleine peptide-gebaseerde dragers die specifiek in tumorweefsel accumuleren na binding aan hun bindingsplaatsen op de cellen, de tumorreceptoren. Hun belangrijkste klaringsroute uit het lichaam is via de nieren. 2) nanosized dragers (moleculaire of supramoleculaire nanodeeltjes) die kunnen zorgen voor accumulatie van radioactiviteit in de tumor via passieve mechanismen (dus niet via receptoren). Bekend van deze deeltjes is dat ze snelle en hoge lever- / miltopname kunnen vertonen, wat ongunstig is tijdens zowel imaging als therapie.

Het doel van onze preklinische studies was om verschillende radioactief gelabelde tracers voor tumorbeeldvorming en therapie te ontwikkelen, te verbeteren en te evalueren.

Hoofdstuk 1 van dit proefschrift geeft een introductie met betrekking tot radioactiviteit, het gebruik daarvan in de geneeskunde en de twee categorieën tracers die hierboven genoemd zijn. Verschillende aspecten van opname- en accumulatiemechanismen van radioactiviteit in tumoren en de organen die zorgen voor de klaring uit het lichaam zijn beschreven.

In **Hoofdstuk 2** presenteren we twee studies uitgevoerd met twee radioactief gelabelde peptide-tracers (d.w.z. somatostatine-analogen) voor beeldvorming en therapie van neuroendocriene tumoren (NETs). **Hoofdstuk 2.1** beschrijft een preklinische evaluatie studie waarin het nieuwe hybride, d.w.z. radioactief en optisch gelabeld, somatostatine analoog Cy5-^{111}In-DTPA-Tyr^3-octreotaat is vergeleken met ^{111}In-DTPA-Tyr^3-octreotaat. Nucleaire beeldvorming met radioactief gelabelde somatostatine analoga wordt reeds met veel succes toegepast in de kliniek voor tumorvisualisatie, chirurgische planning en behandeling van patiënten met NETs. De integratie van nucleaire technieken met optische technieken kan bijdragen tot verdere verbetering van beeldvorming tijdens chirurgie. Hybride moleculen die bijvoorbeeld de DTPA chelator en Cy5 voor optische beeldvorming bevatten, kunnen gebruikt worden voor het genereren van dergelijke dubbel gelabelde peptiden (d.w.z. Cy5-^{111}In-DTPA-Tyr^3-octreotaat) voor multimodale beeldvorming. Het relatief grote hy-

bride molecuul bleek echter de affiniteit voor de receptoren op tumorcellen in in vitro studies (bijvoorbeeld in cellen in kweekbakjes) aanzienlijk te verminderen. Echter, in muizenstudies vertoonde Cy5-^{111}In-DTPA-Tyr^3-octreotaat een goede opname in de tumoren in deze muizen. De resultaten hebben aangetoond dat Cy5-^{111}In-DTPA-Tyr^3-octreotaat een veelbelovende verbinding is voor klinische beeldgeleide resectie van neuroendocriene tumoren met gecombineerde nucleaire en optische visualisatie van tumorweefsel. In **Hoofdstuk 2.2** beschrijven we de effecten van specifieke activiteit en behandelingsschema's op de therapeutische effecten van ^{177}Lu-DOTA-Tyr^3-octreotaat in muizen. Voor een effectieve tumorbehandeling moet een hoge stralingsdosis aan de tumor worden gegeven, terwijl gezonde organen juist een niet-toxische dosis krijgen om bijwerkingen te voorkomen. Verhoging van de opname in tumor versus die in gezonde organen zal daarom de therapeutische opties van deze therapie verbeteren. Verhoging van de specifieke activiteit van het toegediende peptide verbeterde de stralingsdosis op de tumor en in het algemeen resulteerde dit ook in hogere tumor- / normale orgaanopname in vergelijking met toepassingen met lage specifieke activiteit. Fractionering van de dosis kan ook een rol spelen in de verbetering van de therapeutische effecten, aangezien dosisfractionering geen vermindering veroorzaakte in de antitumorrespons, maar wel kan zorgen voor minder bijwerkingen in normale organen.

Hoofdstuk 3 beschrijft het in vivo gedrag in muizen van twee verschillende nanostructuren ontwikkeld voor opname van radioactiviteit in tumoren: Pluronic P94 blokcopolymeer en een supramoleculaire structuur gebaseerd op Polystyreen-poly (ethyleenoxide) (PS-b-PEO). In **Hoofdstuk 3.1** beschrijven we de effecten van verschillende toedieningsroutes (intravenous (IV) of intratumoraal (IT)) van radioactief gelabelde Pluronic P94 op tumoropname, retentie en biodistributie in vivo in een muis tumormodel. Pluronic P94 zijn triblokcopolymeren die in tumorcellen in kweekbakjes opname vertoonden en in muizen gunstige bloedcirculatietijden lieten zien, wat deze tracer potentieel geschikt maakt voor tumor imaging. IV-injectie van radioactief gelabelde tracer resulteerde echter in heel beperkte tumoropname, terwijl IT-toediening daarentegen de radioactiviteit-opname in tumorweefsel aanzienlijk verbeterde en daarmee de opties voor tumortherapie. Er was ook minimale opname in normale organen (na IT-toediening), in combinatie met de uitstekende retentietijd in de tumor bleek Pluronic P94 copolymeer daarom veelbelovend voor verder onderzoek. In **Hoofdstuk 3.2** rapporteren we over een nieuwe en eenvoudige methode voor radioactieve labeling van PS-b-PEO supramoleculaire aggregaten voor nucleaire beeldvorming. Deze diblokcopolymeren kunnen aggregeren tot stabiele supramoleculaire structuren. Tijdens het aggregatieproces kunnen ze verschillende stoffen opnemen, waaronder radionucliden, met het voordeel dat chemische modificatie van het tracermolecuul (door bijvoorbeeld covalente binding van een chelator) niet nodig is. De in vivo-evaluatie van de aggregaten via nucleaire beeldvorming vertoonde een gunstige verblijftijd in het bloed in muizen. Ook werd er geen acute toxiciteit gevonden en was er relatief lage accumulatie in de lever. Deze observaties laten de potentie van PS-b-PEO-structuren voor de afgifte van beeldvormings- en / of therapeutische radionucliden aan tumoren zien. Naast het gemak van radiolabeling kunnen PS-b-PEO supramoleculaire struc-

turen eenvoudig worden aangepast qua grootte. De grootte van nanopartikels wordt namelijk beschouwd als een van de belangrijkste factoren die de biodistributie beïnvloeden, inclusief de efficiëntie van tumorafgifte. Weinig is echter bekend van de effecten van verschillende toegediende doses bij in vivo toepassing in bijvoorbeeld muizen; hoge doses zouden de opname in verschillende weefsels kunnen verzadigen. De studie in **Hoofdstuk 3.3** is de eerste in vivo biodistributie en tumoropname studie met PS-b-PEO supramoleculaire aggregaten van twee verschillende groottes, deze zijn toegepast in twee verschillende doses in een muismodel in vivo. Onze resultaten duiden erop dat PS-b-PEO aggregaten een specifieke grootte-en-dosis afhankelijke biodistributie vertonen met een tendens richting een betere verhouding in tumor/normale weefsel verdeling bij lagere doseringen en/of kleinere partikels.

CURRICULUM VITAE

Costanza Santini was born of the 9th of November 1984 in Florence, Italy. After finishing her secondary education at the Liceo Scientifico Statale Niccoló Rodolico in Florence, she continued her study at the Univesitá degli Studi di Firenze (University of Florence), Italy. She obtained the Bachelor's degree in Biology in 2007. In 2011 she completed the Master degree in Molecular Biology with the highest grade. She did her internship at the department of Preclinical and Clinical Pharmacology in Florence. After graduation, she spent some time traveling and she worked as a teacher of mathematics and science in a secondary school and as a researcher at the CERM, Sesto Fiorentino, Italy. In 2013 she enrolled in the European Program under the 7th frame Marie Curie Action "Trace'n'Treat' as a PhD candidate under the supervision of Marion de Jong and Monique Bernsen Between 2013 and 2017 she carried out her doctoral research at the department of Nuclear Medicine at the Erasmus Medical Center, Rotterdam, The Netherlands. The work was performed in close collaboration with members of other European universities and institutes. Her research was mostly focused on the in vivo (preclinical) evaluation of newly developed radiolabeled peptides and supramolecular carriers for tumor targeting and therapy. As a part of her PhD studies she spent a few months at the JRC-ITU (Joint Research Centrum- Institute of Trans-Uranium Element) in Karlsruhe, Germany, in the department of Nuclear Chemistry in the group of Alfred Morgenstern, where she received a training in the handling of alpha emitters.

LIST OF PUBLICATIONS

Evaluation of a Fluorescent and Radiolabeled Hybrid somatostatin analogue In Vitro and in Mice Bearing H69 Neuroendocrine Xenografts, ***Santini C****, Kuil J, Bunschoten A, Pool S, de Blois E, Ridwan Y, Essers J, Bernsen MR, van Leeuwen FW, de Jong M.. J Nucl Med. 2016 Aug;57(8):1289-95. doi:10.2967/jnumed.115.164970. Epub 2016 Apr 28. PubMed PMID: 27127222.*

The influence of increasing specific activity of ^{177}Lu-DOTA, Tyr^3-octreotate and multiple dosing on tumor dose and therapeutic response in a H69 nude mice model, *Bison SM,* ***Santini C*** *, Koelewijn SJ, de Blois E, Melis M, de Jong M, Konijnenberg MW, An uptdated version has been submitted to Journal of Nuclear Medicine*

Intravenous and intratumoral injection of Pluronic P94: the effect of administration route on biodistribution and tumor retention, ***Santini C****, Arranja A, Denkova AG, Schosseler F, Morawska K, Dubruel P, Mendes E, de Jong M, Bernsen M, Nanomedicine: Nanotechnology, Biology and Medicine, doi:https://doi.org/10.1016/j.nano.2017.04.015.*

Radiolabeling polymeric micelles for in vivo evaluation: a novel, fast, and facile method, ***Santini C*****, Laan AC*, Jennings L, de Jong M, Bernsen MR, Denkova AG, EJNMMI Res. 2016 Dec;6(1):12. doi: 0.1186/s13550-016-0167-x. Epub. 2016 Feb 9. PubMed PMID: 26860294; PubMed Central PMCID: PMC4747947*
*The authors contributed equally to the manuscript

Size and dose: factors influencing biodistribution and tumor uptake of polymeric micelles, ***Santini C*****, Laan AC, Jennings L, de Jong M, Bernsen MR, Denkova AG; in preparation for submission to EJNMMI Research*

PHD PORTFOLIO

Department	Radiology and Nuclear Medicine
Research School	Molecular Medicine (MolMed)
PhD Period	April 2013- April 2017
Promotor	Prof. dr. M. de Jong
Co-promotor	Dr. M. Bernsen

PhD Training

	Institute	Year	ECTS
Academic and department skills			
Proefdiercursus (art9) Erasmus MC	Erasmus MC, Rotterdam, NL	2013	3
Cursus Stralingshygiene (level 5B)	Congress bureau, Rotterdam, NL	2013	1.8
HLO Student supervision and training	Erasmus MC, Rotterdam, NL	2014	1.5
Research Meetings, Department of Radiology & Nuclear Medicine	Erasmus MC, Rotterdam, NL	2013-2017	1
Journal Club Meeting Department of Radiology & Nuclear Medicine	Erasmus MC, Rotterdam, NL	2013-2017	1
In-house training in in vivo imaging	Erasmus MC, Rotterdam, NL	2013-2017	1
In-house training in lab skills	Erasmus MC, Rotterdam, NL	2013-2017	1

General Courses			
Workshop: Photoshop and Illustrator	MolMed, Rotterdam, NL	2013	0.3
Research Integrity Course	Erasmus MC, Rotterdam, NL	2014	0.3
Basic course on R programming	MolMed, Rotterdam, NL	2014	1.4
Functional Imaging and Super Resolution – advanced light microscopy course	MolMed, Rotterdam, NL	2014	1
English writing course	MolMed, Rotterdam, NL	2016	2

Project's meeting and workshops			
3rd Trace'n'Treat Consortium Meeting	Erasmus MC, Rotterdam, NL	2013	1.3
Marie Curie Actions: On the last lap to Horizon 2020	EU, Florence, IT	2013	0.3
Workshop: Development and Application of Radiopharmaceuticals	TUDelft. Delft, NL	2013	1.4
4th Trace'n'Treat Consortium Meeting *(oral presentation)*	CNRS, Strasbourg, FR	2014	1.45
5th Trace'n'Treat Consortium Meeting and Project Midterm Review *(oral presentations)*	Jogu Mainz, Mainz DE	2014	1.75
Trace'n'Treat Winter School: Advanced materials for biomedical applications	UGent, Gent, BE	2014	0.6
6th Trace'n'Treat Consortium Meeting *(oral presentation)*	UU, Utrecht, NL	2015	1.45
Trace'n'Treat Spring School	TUDelft, Delft, NL		
7th Trace'n'Treat Consortium Meeting *(oral presentation)*	MMH, Hannover, DE	2015	0.45
8th Trace'n'Treat Consortium Meeting *(oral presentation)*	TUDelft, Delft, NL	2016	0.45

Presentation/posters at international congresses			
ECR congress 2014 *(E-poster)*	ECR, Vienna, AT	2014	1
EANM congress 2014 *(oral presentation)*	EANM, Gothenburg, SE	2014	2
Trace'n'Treat conference *(oral presentation)*	Trace'n' Treat, Lisbon, PT	2015	2
EANM congress 2015 *(poster presentation)*	EANM, Hamburg, DE	2015	2
ECR congress 2016 *(oral presentation)*	ECR, Vienna, AT	2016	2
EANM congress 2016 *(oral presentation)*	EANM, Barcelona, ES	2016	2

Attendance and presentations to specialized seminars and workshops			
The translational imaging course by AMIE	MolMed, Rotterdam, NL	2013	1.4
Training in F-18 labeling	VU, Amsterdam, NL	2013	0.7
NKRV meeting 2014 *(poster presentation)*	NKRV, Groningen, NL	2014	0.3
MolMed Day 2014 *(poster presentation)*	MolMed, Rotterdam, NL	2014	0.3
NKRV meeting 2014	NKRV, Rotterdam, NL	2014	0.3
COST Meeting 2014 *(oral presentation)*	COST, Instanbul, TR	2014	1.6
The European Workshop on Novel Aspects of Nanomedicine	Council of Europe, Strasbourg, FR	2014	0.3

MiLabs User Meeting *(oral presentation)*	MiLabs, Utrecht, NL	2015	0.45
NKRV meeting 2016 *(invited oral presentation)*	NKRV, Delft, NL	2016	0.3
NKRV meeting 2016 *(poster presentation)*	NKRV, Nijmegen, NL	2016	0.3
Scientific mission			
Short visit to MiLabs	Trace'n'Treat, MiLabs, Utrecht, NL	2014	0.3
Secondment (2 Months) at the Institute of Trans-Uranium elements (ITU)	Trance'n'Treat, JRC-ITU, Karlsruhe, DE	2015	5
Other activities			
Four deliverables for Trace'n'Treat project		2013-2016	4
Invited chairperson at EANM 2015	EANM, Hamburg. DE	2015	0.1
Invited chairperson at EANM 2016	EANM, Barcelona, ES	2016	0.1
Peer review in EJNMMI		2016	0.3

Total ECTS: >30

ACKNOWLEDGEMENTS

It was a boring afternoon in October, when I applied to position in The Netherlands about something I really did not understand… And there is where one of the most intense and formative experience in life had started.

Moving to another country, living in a new world, become "international", it has always been something I wanted to do in my life. However, leaving friends, family and dealing with a new language, a new job, sometimes a new way of thinking is always hard. There have been days in which all I wanted to do was to cry and run home.

The beautiful people I meet during the last four years have dramatically reduced those black days, and helped me growing professionally and personally.

The first big thank goes to my supervisor and promotor Marion De Jong, that guided me with patience and wisdom towards the hard route of getting a doctorate degree. Didn't matter how deep my frustration was, after a brief chat with her, all the problems seemed to be "not that bad". And for that help (sometimes more as a psychologist than as a boss) I will never be able to thank her enough.

Then I want to thank my co-promotor Monique Bernsen, for all the time she spent with me, to improve my latin-based-english and for the afternoons of "blood, sweat and tears" on our endless papers. What is left after all, is not only a bunch of well-written papers, is the awareness of what it means carrying out good science.

I would like to thank all the colleagues in our small group, the Preclinical Department of Nuclear Medicine: our priceless multifunctional technicians Gaby and Stuart, the Labeling Man Erik, our nice radiation protection office Jan, our Imaging Men Joost and Yanto, our Man of Numbers Mark. I want to thank Merleen -never too busy to listen to me, and Ho Zse for her harsh point of views on my research -actually she turns out to be a sweet friend, always ready to help.

Special thank goes to my room-mates Simone, Sandra and Ingrid, for our long and suffered discussions and complains (but also the happy time!). It was nice to share the room with you, and I am sure I will miss all the vitality and the loyalty among us.

A big thanks goes also to the project leaders and the partners of the Trace'n Treat project: Antonia Denkova, Karin van der Graaf, Peter Dubruel, Eduardo Mendes, Francois Schosseler, Frank Roesch, Bert Wolterbeek, Tobias Ross, Freek Beekman, Arjan Bos, Frank Bruchertseifer and Philippe Overeem. And of course I want to thanks to all the fellows that participated to the project, hoping to continue our collaborations: Vallín García Cruz, Karolina

Morawska (craziness is never enough!), Alexandra Gil Arranja, Laurence Jennings, Oleksandra Ivashchenko, Ana De La Fuente Joaniquet and Johan Postema.

Although not officially part of Trace'n Treat, I would like to thank Adrie Laan for the time he spent in our project, and for the effort to release our papers. And, of course, for the after-work-beers.

My life in The Netherlands, however was not only work, and I have to thank all those people that helped me being happy in the last four years.

A big big thank goes to Pietro, my high-school mate, that hosted me for one month in his living room in Delft before I could find a real house in Rotterdam.

Licia, Alessandro, Manuela and Monica: thank you for the craziness of our nights out in the first months in Rotterdam. I will never forget pizza and BBQs together!

I want to thank all our Italian Family that has grown bigger and bigger in time: our adopted PhD-boy Saša, our architecture professor Ilir, and our master in bureaucracy Ivan; and Alessandro Onnis, Chiara and Sylvie. I will never forget our dinners together, the discussion and the dramas!

I want to thank also all the people of the Neuroscience Department (for the amazing coffee and the Friday-afternoon borrels), and expecially Carmen, Negah, Andy, Mimmo and Freek.

And of course, next to the new ones, were (and are still) the old friends, that didn't let me go away. Lilli, Bea and Claudia, Fabio, Claudia, Giulia, Ricche, Giorgio and Tina, thank you for being there, every time I came back.

Babbo e Mamma, ricordo il giorno che vi dissi "Mi hanno preso in Olanda", e sebbene so che vi piangeva il cuore a vedermi andare via, lontano, ricordo anche che mi avete risposto "Bene. Questa è una bella cosa". Vi ringrazio per avermi insegnato l'amore per il sapere e per avermi dato sempre la libertà di scegliere.

Last but not least, I need to thank my two flat mates, the core of my family in the last years.

The first one comes easy, Tommaso, my love. You move to Rotterdam for me, and I know how much you miss your hills and mountains… I know that I wouldn't be here without you.

The second is Simona, my new sister, my confident, the person with whom I shared my frustration and misery, but also our deeper secrets and our little victories. We build a house together, from the floor to the picture on the wall. I couldn't how would it be, if I hadn't told you "Puoi anche spingere la porta".